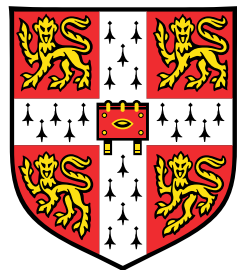


Multi-microscopy Characterisation of III-nitride Devices and Materials



Christopher Xiang Ren

Department of Materials Science and Metallurgy
University of Cambridge

This dissertation is submitted for the degree of
Doctor of Philosophy

Wolfson College

July 2016

I would like to dedicate this thesis to my loving parents ...

Declaration

I hereby declare that except where specific reference is made to the work of others, the contents of this dissertation are original and have not been submitted in whole or in part for consideration for any other degree or qualification in this, or any other university. This dissertation is my own work and contains nothing which is the outcome of work done in collaboration with others, except as specified in the text and Acknowledgements. This dissertation contains fewer than 65,000 words including appendices, bibliography, footnotes, tables and equations and has fewer than 150 figures.

Christopher Xiang Ren
July 2016

Acknowledgements

And I would like to acknowledge ...

Abstract

This is where you write your abstract ...

Table of contents

List of figures	xiii
List of tables	xvii
Nomenclature	xix
1 Introduction	1
1.1 III-Nitride Material Properties	2
1.1.1 Crystal Structure	2
1.1.2 Band Structure	4
1.1.3 Built-in Fields	7
1.1.4 Defects in III-nitrides	10
1.2 III-nitride Devices	16
1.2.1 Light Emitting Diodes	16
1.2.2 Microcavities	17
1.2.3 Nanowires for Nanophotonic Devices	23
2 Experimental Methods	27
2.1 Transmission Electron Microscopy	27
2.1.1 Conventional Transmission Electron Microscopy	28
2.1.2 Scanning Transmission Electron Microscopy	33
2.1.3 Energy-Dispersive X-ray spectroscopy	35
2.2 Electron Tomography	36
2.3 Atomic Force Microscopy	37
2.4 Scanning Electron Microscopy Techniques	40
2.5 Hyperspectral Electroluminescence Mapping	43
2.6 Dual Beam FIB-SEM	44
2.6.1 Sample Preparation	45
2.6.2 Tomography	46

3 Inhomogeneous Electroluminescence in InGaN QW LEDs	49
3.1 Short title	49
3.2 Sample Structure	50
3.3 Experimental	51
3.3.1 Hyperspectral EL Imaging	52
3.3.2 Cathodoluminescence and Electron Beam Induced Current	58
3.3.3 Hexagonal Defect Structure	63
3.3.4 LED Simulations	69
3.4 Conclusion	71
3.5 Future Work	71
References	73
Appendix A How to install L^AT_EX	81
Appendix B Installing the CUED class file	85

List of figures

1.1	Wurtzite unit cell and lattice parameters \mathbf{a} and \mathbf{c} , the (0001),(11-20) and (1-100) planes are shown. Courtesy of J. Griffiths.	3
1.2	Unit cell (dashed line) for GaN crystal structure and lattice parameters $\mathbf{a}_0, \mathbf{c}_0$. Adapted from [7]	3
1.3	Bandgap at room temperature for III-nitride materials with the visible spectrum shown on the left. Courtesy of K. Montgomery.	5
1.4	Band diagram of a quantum well. The bandgap of the well material is denoted E_g , the energy of the ground state transition is denoted E_1 and the conduction and valence bands are denoted E_c, E_v respectively [15].	6
1.5	Illustration of Ga-face (+ c) and N-face (-c) GaN wurtzite crystal exhibiting polarity along the c -axis [17].	7
1.6	GaN unit cell with lattice parameters c and a [19]	8
1.7	Unbiased and biased quantum well energy levels with associated carrier wavefunctions. Under an applied field the overlap between the electron and hole carrier wavefunctions is reduced [22].	9
1.8	Point Defects: vacancy, self-interstitial, substitutional impurity and foreign interstitial.	11
1.9	Misfit dislocation formation through strain relaxation for heteroepitaxial growth: a) the film is grown on a substrate of smaller lattice size b) the film maintains a pseudomorphic relationship with the substrate c) the film relaxes through the formation of a dislocation.	12
1.10	a) a -plane GaN showing basal plane stacking faults (BSFs), prismatic stacking faults (PSFs) and stacking faults bounded partial dislocations (PDs) shown schematically b) and in TEM. Adapted from [28].	13
1.11	Stacking sequences for stacking fault types. The change in stacking sequence is highlighted in the figures [29].	14

1.12 a) TEM image of a hexagonal inverted pyramid defect b) Schematic of a V-pit with its associated TD [34].	15
1.13 Potential landscape due to V-pits decorating the apex of TDs: carriers (blue) need to overcome the energy barriers to recombine non-radiatively at the TDs [34].	15
1.14 a) <i>p-n</i> junction at equilibrium, with the conduction band, Fermi level and valence band denoted E_c, E_F and E_v respectively, the built in potential across the junction is denoted as V_{bi} b) under forward bias of V.	16
1.15 Typical visible light LED structure grown on a sapphire substrate [15].	17
1.16 Illustration of the some key parameters such as FSR and resonant cavity mode FWHM.	19
1.17 Optical resonators.	19
1.18 Illustration of the minimum radius R_{min} for WGM propagation. Rays traversing the region $r < R_{min}$ (denoted in red) exceed the critical angle θ_c and thus escape the cavity. Rays travelling outside this region $r > R_{min}$ (denoted in violet) are confined.	20
1.19 Scanning electron microscope image of a GaN microdisk produced by selective etching of sacrificial AlInN layers [47].	21
1.20 Nanobeam schematic and 3-D FDTD simulation of the electric field intensity profile of the cavity mode adapted from [56].	22
1.21 a) Lasing from the end-facets of a GaN nanowire b) schematic of the triangular InGaN/GaN MQW nanowire grown by Qian <i>et al.</i> c) GaN nanowire coupling to a dielectric cavity d) GaN/InGaN nanowire bundle coupling to a gold plate through a nanogap layer. Adapted from [61–64] respectively.	24
1.22 a) Schematic of the InGaN QD in GaN nanowire structure b) SEM micrograph of the nanowire sample grown by MBE c)TEM micrograph of a single nanowire. Adapted from [65].	24
1.23 a) SEM micrograph showing the a single nanowire on a patterned SiO_2 substrate grown by MOCVD. The inset shows the array of nanowires grown on the substrate b)showing the site-controlled GaN QD at the tip of the nanowire c)schematic of the nanowire structure [66].	25
2.1 h	27
2.2 a) Elastic and b) inelastic interactions for a high energy electron beam incident on a thin sample.	28
2.3 h	29
2.4 h	30

2.5 a) Bright-field and b) dark-field imaging [67].	31
2.6 Specimen is tilted from a) to b) for the g-3g condition [68].	32
2.7 h	33
2.8 h	34
2.9 h	35
2.10 h	36
2.11 Schematic of an atomic force microscope.	37
2.12 The effect of separation on the tip-sample interaction force [78].	38
2.13 Interaction of a hemisphere with a flat-topped island for the cases a) $h > R(1 - \cos(\alpha))$ and b) $h < R(1 - \cos(\alpha))$ adapted from [79].	39
2.14 Measurement error in the depth of a pit caused by the finite width of the AFM tip.	39
2.15 SEM design [80].	40
2.16 Interaction volumes for different interactions of an electron beam [81].	41
2.17 h	42
2.18 h	43
2.19 h	44
2.20 FIB/SEM lamella lift-out and polishing process: a) Protective Pt layer deposition, b) trench milling and Lamella lift out c) final thinning.	45
2.21 h	46
3.1 h	50
3.2 h	51
3.3 a) C5610A b) C5608A EL under a forward bias of 3V. The bright inhomogeneities are visible in the emission of the LEDs.	51
3.4 h	53
3.5 Peak intensity for varying injection current for C5610.	54
3.6 Peak energy for varying injection current for C5610.	55
3.7 h	56
3.8 h	57
3.9 h	57
3.10 h	58
3.11 EL images of the regions examined using CL and EBIC mapping for a) C5610A and b) C5608A.	59
3.12 a) CL and b) EBIC maps acquired simultaneously of the area shown in Fig.3.11 a.	59

3.13 a) CL and b) EBIC maps acquired simultaneously of the area shown in Fig.3.11b.	60
3.14 a) SEM micrograph and b) pan-CL image of an inhomogeneity in C5610A. The pan-CL image utilises a temperature scale (blue = low, red = high).	61
3.15 a)CL peak intensity and b) CL peak energy for the feature shown in Fig.3.14	61
3.16 a) SEM micrograph and b) pan-CL image of an inhomogeneity in C5608A. The pan-CL image utilises a temperature scale (blue = low, red = high).	62
3.17 a)CL peak intensity and b) CL peak energy for the feature shown in Fig.3.16	62
3.18 h	63
3.19 h	64
3.20 h	64
3.21 h	65
3.22 h	66
3.23 h	66
3.24 h	67
3.25 Quantification of the ternary alloy compositions: a) HAADF-STEM image showing the region examined by EDX (blue box) b) aluminium atomic percentage, c) gallium atomic percentage and d) indium atomic percentage.	68
3.26 h	70
3.27 h	71

List of tables

1.1	Room temperature lattice parameters for GaN, InN and AlN [8].	4
1.2	Direct bandgaps of GaN, InN and AlN [8].	4
1.3	Bulk $\frac{c}{a}$ ratios for GaN, InN and AlN [15].	8
1.4	Burgers vectors for pure edge (a), pure screw (c) and mixed (a + c) TDs . .	12
1.5	BSF types in wurtzite materials.	13

Nomenclature

Acronyms / Abbreviations

1-D	One-Dimensional
AFM	Atomic Force Microscopy
AlN	Aluminium Nitride
BSE	Back Scattered Electron
BSF	Basal-plane Stacking Fault
C-AFM	Conductive Atomic Force Microscopy
EBL	Electron Blocking Layer
EL	Electroluminescence
ET	Electron Tomography
FIBT	Focussed Ion Beam Tomography
FSR	Free Spectral Range
GaAs	Gallium Arsenide
GaN	Gallium Nitride
InN	Indium Nitride
LED	Light-Emitting Diode
PD	Partial Dislocation
PSF	Prismatic Stacking Fault

SEM	Scanning Electron Microscope
SE	Secondary Electron
SPS	Single Photon Source
WGM	Whispering Gallery Mode

Chapter 1

Introduction

Gallium nitride (GaN) has been described as 'the most important semiconductor material since silicon' [1], and indeed the influence of this incredible material and its associated alloys (termed III-nitrides) is pervasive in modern society. The impact of III-nitride materials is perhaps best evidenced by the recent global transition from traditional lighting sources to semiconductor lighting solutions based on III-nitride materials. Since the first demonstration of a high-brightness blue light emitting diode (LED) in 1991 by Shuji Nakamura [2], the widespread use of III-nitride LEDs for general lighting purposes has blossomed into a multi-billion pound industry.

The extraordinary optical properties of III-nitride materials have also enabled their application beyond general lighting: the development of III-nitride based lasers has found applications in telecommunications [3], medicine [4] and data storage, whilst III-nitride optical emitters have been used as single photon sources (SPSs) which have applications in cryptography for secure communications [5].

The optoelectronic properties of III-nitride materials are somewhat astonishing: GaN suffers from a defect density several orders of magnitude higher than other optically active semiconductor materials such as gallium arsenide (GaAs) [6] yet is still optically active. Nonetheless, the effects of defects originating from the heteropitaxial growth of GaN are clearly deleterious when considering III-nitride device operation, highlighting the fickle relationship between the compositional and structural properties of III-nitride and their optical properties. This work aims to explore the manner in which the microstructural properties of photonic III-nitride devices affect their performance by combining multiple microscopy techniques to examine the same feature at the micro- and nano-scale, thus allowing us to link specific structural features with emissive properties at the device level. The experimental research in this thesis is separated into four main sections.

The first section details the investigation of inhomogeneous electroluminescence (EL) of in-

dium gallium nitride (InGaN) quantum well (QW) LEDs. By employing the use of scanning probe techniques, electron microscopy and spatially resolved luminescence spectroscopy the underpinning cause of inhomogeneous LED emission behaviour was elucidated.

The second section involves microscopy-based investigation into the mechanisms behind incomplete etching in the fabrication of III-nitride based microdisk cavities and the effect of this issue on the overall optical performance of these cavities. Using focussed ion beam techniques developed over the course of this work, the first direct observation of a dislocation induced whisker on the underside of a microdisk cavity was reported.

The third section describes the microscopy of one dimensional (1-D) photonic crystal cavity (PCC) 'nanobeam' cavities. This section concerns the use of tomographic techniques such as electron tomography (ET) and focussed ion beam tomography (FIB-T) to investigate the manner in which fabrication issues can affect the 3-D morphology and thus the quality of III-nitride nanobeam cavities.

The final section describes a correlative study of III-nitride nano and micro-rods grown at the Cambridge Centre for Gallium Nitride. By examining both the optical properties of these rods using luminescence spectroscopy methods and examining the microstructure using electron microscopy, the growth conditions of these rods were optimised and tailored to specific applications such as single photon sources or low-threshold lasers.

1.1 III-Nitride Material Properties

1.1.1 Crystal Structure

GaN can crystallise into two distinct crystal structures: hexagonal (wurtzite) and cubic (zinc blende and rock salt). Under ambient conditions, wurtzite GaN is the most commonly studied form as it is the most structurally stable. Thus, the work discussed in this thesis concerns wurtzite III-nitrides. A schematic of a wurtzite III-nitride crystal structure is shown in Fig.1.1 and consists of stacked hexagonal close-packed planes following an ABABAB stacking sequence. Atoms of the respective elements (gallium and nitrogen) are tetrahedrally bonded to one another. However, in the case of III-nitrides this structure deviates from ideal tetrahedral bonding and results in a non-zero dipole moment for each unit cell which will be discussed in the following sections.

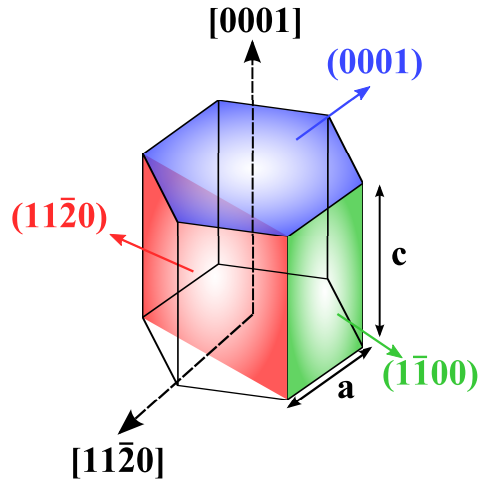


Fig. 1.1 Wurtzite unit cell and lattice parameters \mathbf{a} and \mathbf{c} , the (0001) , $(11\bar{2}0)$ and $(\bar{1}100)$ planes are shown. Courtesy of J. Griffiths.

A 4-index Miller-Bravais notation ($hkil$) is used to denote the crystal planes where the index i is defined by the relation:

$$i = -(h+k) \quad (1.1)$$

The crystallographic planes (0001) , $(\bar{1}100)$ and $(11\bar{2}0)$ shown in Fig.1.1 are often termed the c , m and a -planes in the literature. The fundamental unit cell of the wurtzite GaN crystal structure and its associated lattice parameters \mathbf{a} and \mathbf{c} is shown in Fig.1.2

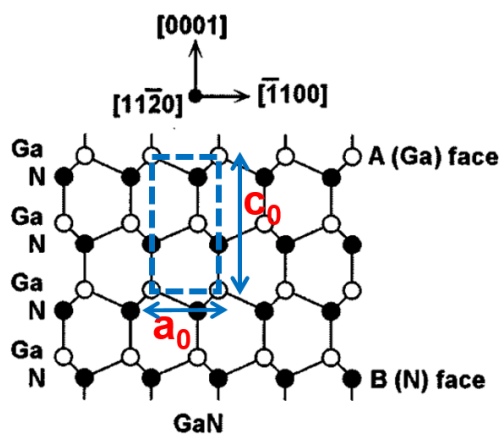


Fig. 1.2 Unit cell (dashed line) for GaN crystal structure and lattice parameters \mathbf{a}_0 , \mathbf{c}_0 . Adapted from [7]

Other members of the III-nitride materials such as indium nitride (InN) or aluminium nitride (AlN) have different lattice parameters due to the differing atomic radii of aluminium and indium relative to gallium.

Alloy	\mathbf{a} (\AA) at T = 300K	\mathbf{c} (\AA) at T = 300K
GaN	3.189	5.185
InN	3.545	5.703
AlN	3.112	4.982

Table 1.1 Room temperature lattice parameters for GaN, InN and AlN [8].

III-nitride photonic devices are often heterostructures consisting of ternary alloys of the materials shown in Table 1.1. Lattice parameters of a relaxed ternary alloy $A_xB_{1-x}N$ can be estimated using Vegard's law [9]:

$$\mathbf{a} = x\mathbf{a}_{AN} + (1 - x)\mathbf{a}_{BN} \quad (1.2)$$

$$\mathbf{c} = x\mathbf{c}_{AN} + (1 - x)\mathbf{c}_{BN} \quad (1.3)$$

Typical indium compositions for blue LEDs range between 15-20 %, which leads to a lattice mismatch of approximately 2 %, resulting in considerable amounts of strain in these GaN/InGaN heterostructures.

1.1.2 Band Structure

One of the principal driving factors behind the interest in III-nitrides for photonic devices is their direct bandgap which collectively spans the visible spectrum and beyond. The bandgap of III-nitride binary alloys is given below in Table 1.2.

Alloy	Bandgap (eV)
GaN	3.51
InN	0.78
AlN	6.25

Table 1.2 Direct bandgaps of GaN, InN and AlN [8].

Ternary alloying modifies the bandgap as shown in Fig. 1.3. In theory the entire range of 0.78-6.25 eV is accessible through alloying, though material limitations reduce the full effective range for III-nitride devices [10].

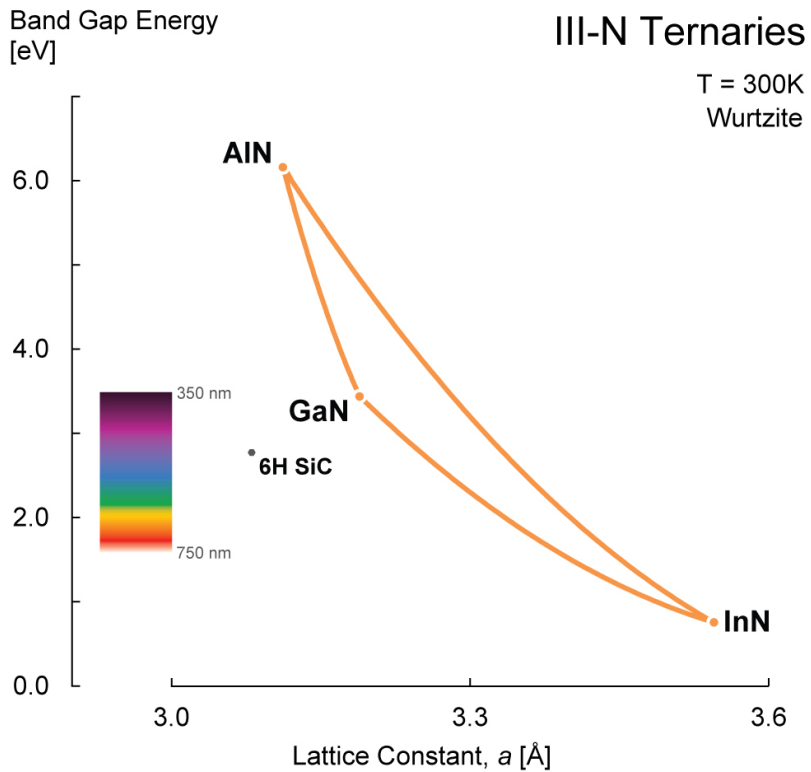


Fig. 1.3 Bandgap at room temperature for III-nitride materials with the visible spectrum shown on the left. Courtesy of K. Montgomery.

The bandgap of a ternary alloy $A_xB_{1-x}N$ is given by a modified Vegard's Law:

$$E_g = xE_g^{AN} + (1-x)E_g^{BN} - x(1-x)C \quad (1.4)$$

Where C is a bowing parameter which accounts for deviation from a linear relation between ternary alloy composition and bandgap energy. The value of the InGaN bowing parameter has been widely debated in the literature due to the lack of a reliable value for the bandgap energy for InN [8]. Although the current value of 1.4 eV is reported, there are also suggestions the bowing parameter may be composition dependent [11–13].

In considering the optical properties of III-nitride materials it is also important to consider the effects of impurities and defects. Crystal disorder introduces further energy states which would be 'forbidden' in an ideal crystal lattice leading to an effective smearing of the bandgap. Sub-bandgap absorption can occur due to the introduction of these defective states. The smearing out of the absorption edge of the material is known as the 'Urbach tail', and can be a highly deleterious source of loss in III-nitride cavity structures [14].

Quantum Confinement Effects

The first prototype high-brightness blue III-nitride LED consisted of a GaN *p-n* junction, or a 'homojunction' [2], however modern LED structures consist of heterostructures known as quantum wells. QWs consist of a thin layer of low bandgap material between two quantum barriers with a higher bandgap. Carriers in the low bandgap material are effectively confined in one direction, hence the term 'quantum well'. This confinement leads to the discretisation of the carrier wavefunctions within the well, as shown schematically in Fig.1.4.

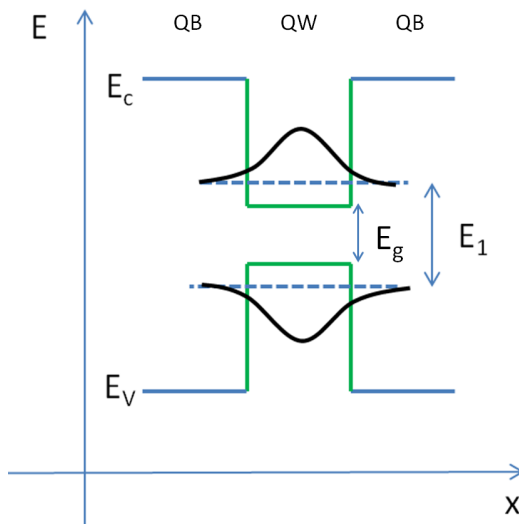


Fig. 1.4 Band diagram of a quantum well. The bandgap of the well material is denoted E_g , the energy of the ground state transition is denoted E_1 and the conduction and valence bands are denoted E_c, E_v respectively [15].

Thus the energy of the transition in the QW is given by the following relation:

$$h\nu = E_1 - E_{ex} \quad (1.5)$$

where E_1 is the energy of the ground state transition and E_{ex} is the exciton binding energy. For an infinite potential well of thickness L, the ground state E_1 is given by:

$$E_1 = \frac{\hbar^2 \pi^2}{2m^* L^2} \quad (1.6)$$

where \hbar is the reduced Plank constant, m^* is the carrier effective mass. As such, the energy of the optical transition is related to the thickness of the well.

1.1.3 Built-in Fields

III-nitride materials in wurtzite structure are termed 'polar' materials, due to the fact they exhibit a spontaneous polarisation field [16]. This occurs due to the III-nitride bonding structure's deviation from an ideal tetrahedral structure along the (0001) axis of the crystal, combined with the ionicity of the bond [15]. This deviation causes each unit cell to possess a non-zero dipole moment along the principal axis of the tetrahedral bonding structure, resulting in an overall spontaneous polarization in the crystal. As the III-nitride wurtzite structure is non-centrosymmetric, the direction of the polarization depends on whether the crystal exhibits (+c) or (-c) polarity, as shown in Fig.1.5

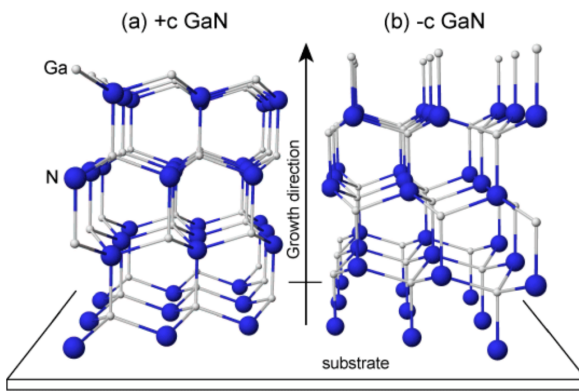


Fig. 1.5 Illustration of Ga-face (+c) and N-face (-c) GaN wurtzite crystal exhibiting polarity along the c-axis [17].

This non-zero dipole moment is particularly strong for III-nitrides relative to other III-V semiconductors due to the strong electronegativity and small size of nitrogen compared to other group V elements, resulting in a metal-nitrogen bond with greater ionicity than other III-V bonds [18]. Fig.1.6 shows a GaN unit cell with lattice parameters c and a denoted.

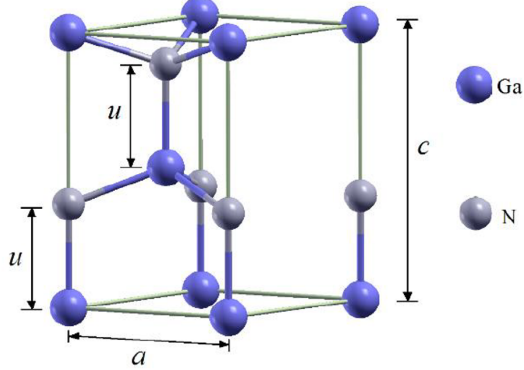


Figure 1. Unit cell 1x1-MN/GaN (M = V, Cr and Mn) multilayers.

Fig. 1.6 GaN unit cell with lattice parameters c and a [19]

If all nearest neighbour bond lengths are equal, an ideal hexagonal closed packed crystal exhibiting zero spontaneous polarisation would have a ratio of lattice parameters denoted by:

$$\frac{c}{a} = \left(\frac{8}{3}\right)^{0.5} = 1.63299 \quad (1.7)$$

The degree of spontaneous polarisation observed in III-nitride materials is thus determined by the amount their lattice parameter ratio deviates from this ideal value. The values for bulk III-nitride materials are given in Table 1.3.

Alloy	$\frac{c}{a}$
GaN	1.6259
InN	1.6116
AlN	1.6010

Table 1.3 Bulk $\frac{c}{a}$ ratios for GaN, InN and AlN [15].

A lower $\frac{c}{a}$ ratio indicates a higher angle between the three bonds at the base of the tetrahedral bonding structure, resulting in a lower compensation polarisation along the (0001) axis and a higher spontaneous polarisation. Thus, according to Table 1.3 the strongest spontaneous polarisation is observed in AlN and the weakest in GaN.

It is important to note that materials which exhibit spontaneous polarisation also exhibit piezoelectric polarisation [16]. Strain experienced by the material results in the distortion of the crystal lattice, which can either alleviate or exacerbate the deviation from the ideal tetrahedral structure resulting in additional polarisation fields. This piezoelectric polarization is a crucial consideration in III-nitride devices which often consist of QW heterostructures as

lattice mismatches with underlying layers result in the expansion or contraction of III-nitride films. Interestingly two different polarisation configurations are obtained for AlGaN and InGaN coherently strained to GaN. In the case of InGaN the piezoelectric field acts against the spontaneous field, whilst the opposite is true for AlGaN strained to GaN. Within the context of visible light LEDs, InGaN containing QWs are dominated by the piezoelectric contribution to the polarization fields [20] due to the sizeable lattice mismatch between GaN and InN (11%) [21].

The Quantum Confined Stark Effect

III-nitride photonic devices often make use of heterostructures known as quantum wells, which enhance radiative efficiency by confining carrier wavefunctions over a range of several nanometres. Given the presence of built-in fields in III-nitride materials, it is important to consider the effect polarisation fields will have on the band structure and thus optical properties of quantum wells as shown in Fig.1.7

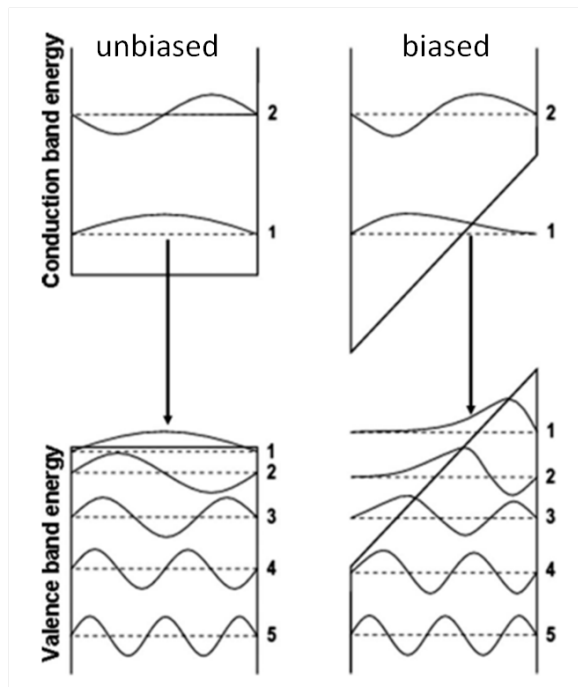


Fig. 1.7 Unbiased and biased quantum well energy levels with associated carrier wavefunctions. Under an applied field the overlap between the electron and hole carrier wavefunctions is reduced [22].

The field-induced transition from a rectangular to a 'sawtooth'-shaped potential well results in the reduction in energy of the optical transition, meaning the photons emitted from the QW are red-shifted. However, as the carrier density within the QW is increased, by either

optical or electrical injection, the polarization fields are effectively screened resulting in a carrier density-dependent optical transition energy.

A further effect of the polarization fields is to spatially separate the carrier wave functions, thus reducing their overlap as shown in Fig.1.7. This results in a reduced probability for the radiative recombination carriers thus reducing the efficiency of III-nitride QW emitters.

1.1.4 Defects in III-nitrides

Many issues with III-nitride based optoelectronic devices arise from the high defect densities inherent to the heteroepitaxially grown material. Dislocation densities tend to be several orders of magnitude higher in nitride devices relative to other III-V materials due to the lack of a low cost, widely-available lattice matched substrate [6]. Lattice mismatch and alloy specific growth temperatures results in the presence of imperfections in the crystal structure of the epitaxial film known as defects. These defects can result in perturbations to the electrical and optical properties of an 'ideal' crystal, and are often classified based on their spatial dimensions. 0-D defects are often referred to as point defects, 1-D defects are commonly termed linear defects or dislocations, 2-D defects are known as planar defects or stacking faults, and there are a variety of 3-D defects known as volume defects.

0-D Defects

Point defects exist in four main forms, shown in Fig.1.8. Vacancies, where an atom is missing from the lattice, and self-interstitial point defects are termed 'native defects': there is no inclusion of foreign atoms. These two types of intrinsic point defects are shown in Fig.1.8 a) and b) respectively.

In the case of GaN, three types of vacancies can exist: gallium vacancies, nitrogen vacancies and divacancies. The gallium vacancy (V_{Ga}) has a low formation energy in *n*-type GaN, is acceptor-like and has a low migration barrier. Due to this low migration energy, it is expected that gallium vacancies form complexes with more stable defects. Gallium vacancies and associated complexes are thought to be the cause of yellow luminescence observed in *n*-type GaN [6].

Nitrogen vacancies initially attracted a large amount of interest due to the common belief that their energy levels were close to or within the conduction band. Due to this, the *n*-type conductivity of undoped GaN was attributed to nitrogen vacancies [23]. However, calculations have shown the thermal equilibrium of nitrogen vacancies to be too low to account for the observed conductivity. Nitrogen vacancies are also expected to have relatively low migration barriers, indicating complexes involving more stable defects may occur during

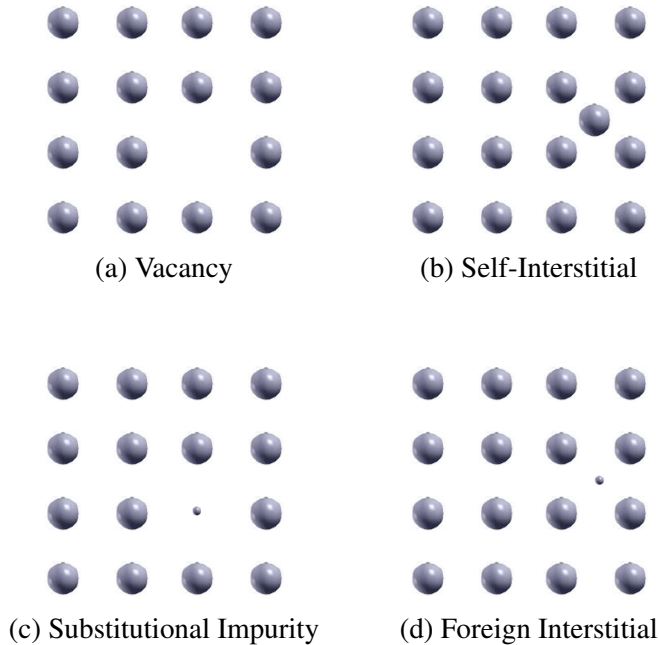


Fig. 1.8 Point Defects: vacancy, self-interstitial, substitutional impurity and foreign interstitial.

high-temperature growth or annealing, especially in *p*-type GaN [24]. Divacancies have high formation energy in GaN and are not expected to form in large concentrations [24].

The inclusion of foreign atoms can result in a foreign interstitial point defect, or a substitutional impurity, both are shown in Fig.1.8 c) and d) respectively. The formation of self-interstitial or antisite (swapping of Ga and N lattice positions in the lattice) have a low occurrence due to the small lattice constant of GaN and large size mismatch between Ga and N atoms [24].

Point defects are responsible for a plethora of deleterious effects at the device level in III-nitrides: they can reduce radiative efficiency, produce undesired luminescence and act as parasitic current paths [24].

1-D Defects

Dislocations in GaN epilayers are categorised in two main forms: misfit dislocations (MDs) and threading dislocations (TDs). The origins of misfit dislocations are quite well understood: they occur through the release of misfit strain at interfaces between two crystals of differing lattice constants. The process is shown in Fig.1.10: a film with a lattice parameter greater than the substrate is grown as is typical for III-nitride epilayers (GaN on sapphire or InGaN on GaN) and as a result the grown layer experiences compressive stress and forms a pseudo-morphic layer. The top layer is strained and matched to the lower layer due to its smaller

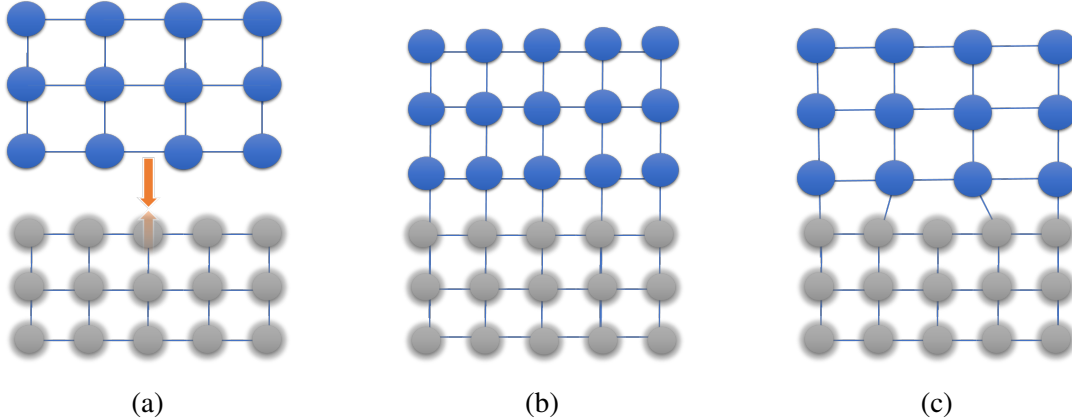


Fig. 1.9 Misfit dislocation formation through strain relaxation for heteroepitaxial growth: a) the film is grown on a substrate of smaller lattice size b) the film maintains a pseudomorphic relationship with the substrate c) the film relaxes through the formation of a dislocation.

lattice parameter. Strain relaxation occurs as the pseudomorphic relationship is broken when the top film reaches a critical thickness and results in the formation of misfit dislocations.

The origins of TDs are however still widely debated. TDs are not believed to relieve mismatch stress, and typically propagate perpendicular to the planar surface. TDs are classified into three categories based on their Burgers vector, as shown in Table 1.4.

Dislocation type	Burgers vector
a type	$\frac{1}{3} < 1\bar{1}20 >$
c type	$< 0001 >$
a + c type	$\frac{1}{3} < 11\bar{2}3 >$

Table 1.4 Burgers vectors for pure edge (**a**), pure screw (**c**) and mixed (**a + c**) TDs

It was initially reported that GaN islands on sapphire during the initial stages of growth may be misorientated with respect to one another and that TDs were generated during the coalescence of these misorientated islands [25]. This was seemingly disproven by a transmission electron microscopy data from a study on partially coalesced GaN on sapphire layers at various growth stages, which indicated the large majority of TDs seemed to initiate from within the nucleation layers at the GaN/sapphire interface rather than at coalescence boundaries [26]. Oliver *et al.* used silane treatment to enlarge dislocation pits and observe them using atomic force microscopy, finding no significant relationship between boundary regions and the locations of dislocations [27]. It was however suggested that dislocations may arise from the overgrowth of smaller islands by larger ones. Thus, while there is convincing evidence that TDs do not originate due to island coalescence, the actual mechanism behind their generation remains an area of active research.

2-D Defects

Stacking faults are defects which disrupt the regular stacking sequence of the crystal structure. In non-polar heterostructures they can intersect the QW layers. As a result of this, stacking faults are a more pressing concern than dislocations in epitaxial films grown along alternative directions to the c -plane, as in polar materials stacking faults tend to remain in the nucleation layers [10]. Fig. 1.10 shows different forms of stacking faults in (11̄20) GaN (a -plane) on r -plane sapphire. Basal-plane stacking faults (BSFs) are atomic layers with a modified stacking sequence in the wurtzite crystal matrix. These BSFs can transfer to another stacking plane through prismatic stacking faults (PSFs). BSFs can also be bound by partial dislocations (PDs).

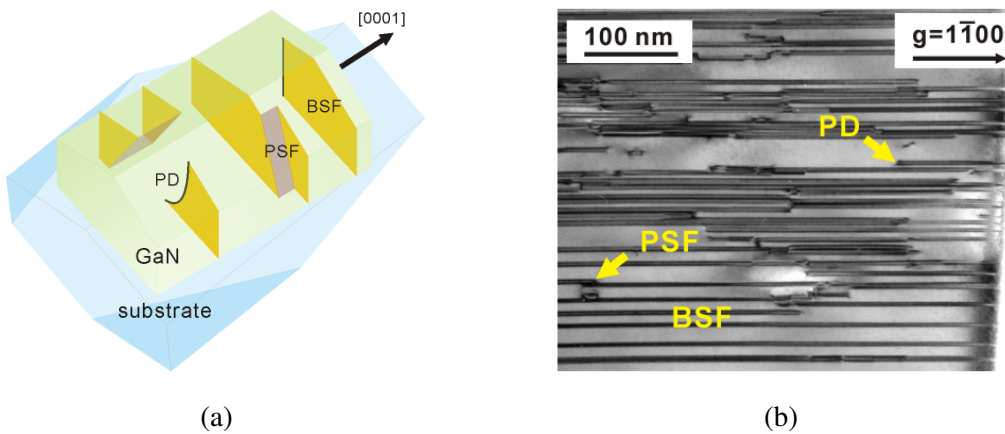


Fig. 1.10 a) a -plane GaN showing basal plane stacking faults (BSFs), prismatic stacking faults (PSFs) and stacking faults bounded partial dislocations (PDs) shown schematically b) and in TEM. Adapted from [28].

Three types of BSFs exist in wurtzite crystals, they are classified based on their displacement vector \vec{R} as shown in Table 1.5 and in Fig. 1.11.

BSF type	Displacement vector \vec{R}
I_1	$\frac{1}{6} < 20\bar{2}3 >$
I_2	$\frac{1}{3} < 10\bar{1}0 >$
E	$\frac{1}{2} < 0001 >$

Table 1.5 BSF types in wurtzite materials.

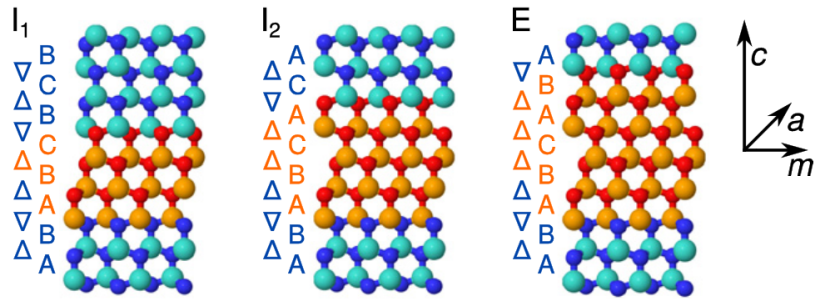


Fig. 1.11 Stacking sequences for stacking fault types. The change in stacking sequence is highlighted in the figures [29].

Whilst TDs are considered completely undesirable due to the adverse effects they may have on radiative processes and carrier transport, it has been suggested the presence of BSFs on the optical properties may be beneficial in some cases. As first indicated by Rieger *et al.* [30] and Rebane *et al.* [31], BSFs may be considered as zinc-blende QWs in a wurtzite matrix, thus enabling radiative recombination through confinement. The characteristic BSF luminescence has been used to determine the spontaneous polarization of wurtzite GaN [32] as well as the diffusion length in GaN nanowires[33].

3-D Defects

There are many forms of 3-D defects in III-nitrides such as voids, nanopipes and cracks. In this particular section we will focus on those relevant to the work featured in later chapters of this work.

Inverted hexagonal pyramid defects, also known as V-pits, are defects commonly found at the surface of InGaN/GaN QW structures. They form as a result of a TD intersecting the QW layers in heterostructures. It is believed that the low temperatures required for the growth of the InGaN layers allow even minute perturbations of the surface to persist into inclined facets with low growth rates, such as the $(1\bar{1}01)$ facets. The apex of TDs thus provide optimal conditions for the formation of V-pits during the growth of InGaN layers [34]. Interestingly, TEM studies have shown that the QW layers disrupted by the defect grow along the semi-polar facets at a lower thickness [34–36]. Fig.1.12 shows a TEM image of a V-pit in an InGaN/GaN multiple QW structure with a schematic describing this defect and the manner it affects the growth of the QWs.

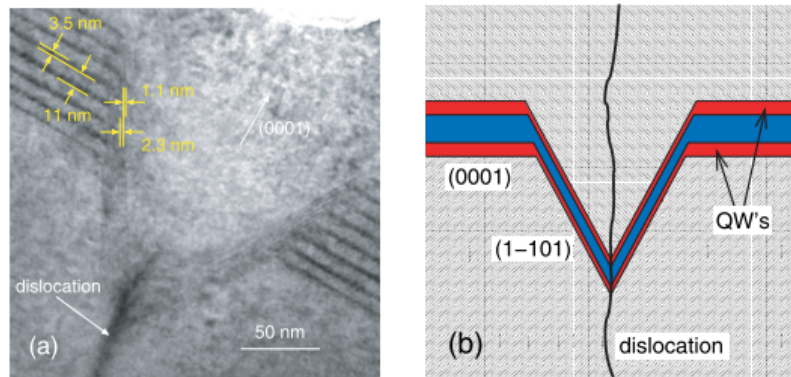


Fig. 1.12 a) TEM image of a hexagonal inverted pyramid defect b) Schematic of a V-pit with its associated TD [34].

The existence of TDs as non-radiative recombination centres has been well documented [6], however it is believed that V-pits suppress this non-radiative recombination and provide an increase in light emission efficiency in III-nitride devices by providing an energy barrier surround TDs [34]. Hangleiter *et al.* suggested the thinner wells grown along the semi-polar facets of the V-pit provided an energy barrier of several hundred meV relative to the normal c-plane QWs [34], thus providing a potential landscape shielding carriers from TDs, as shown in Fig.1.13.

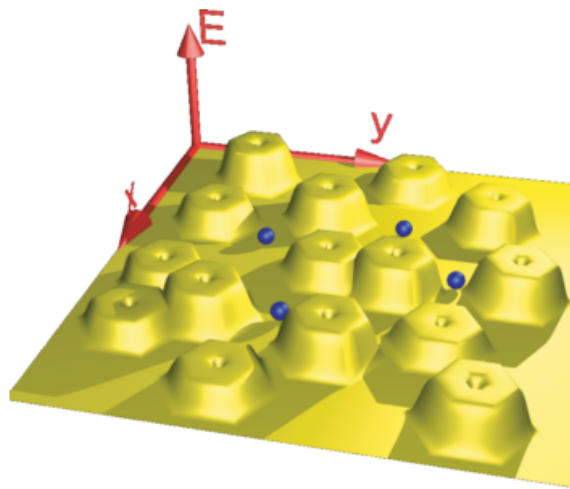


Fig. 1.13 Potential landscape due to V-pits decorating the apex of TDs: carriers (blue) need to overcome the energy barriers to recombine non-radiatively at the TDs [34].

1.2 III-nitride Devices

1.2.1 Light Emitting Diodes

Light emitting diodes (LEDs) are the most widespread commercial application of III-nitride materials. These devices typically consist of a p-n junction. This consists of material containing excess acceptor (*p*-doped) and another containing excess donor impurities (*n*-doped) which are brought into contact. This allows holes from the *p*-type material and electrons from the *n*-type material to diffuse across the junction until an equilibrium state is reached. A region where the electric field from the charged dopants on either side prevents diffusion is formed known as the depletion region. The application of forward bias reduces the built-in potential across the depletion region and allows for the flow of electrons and holes across the junction, as shown schematically in Fig.1.14.

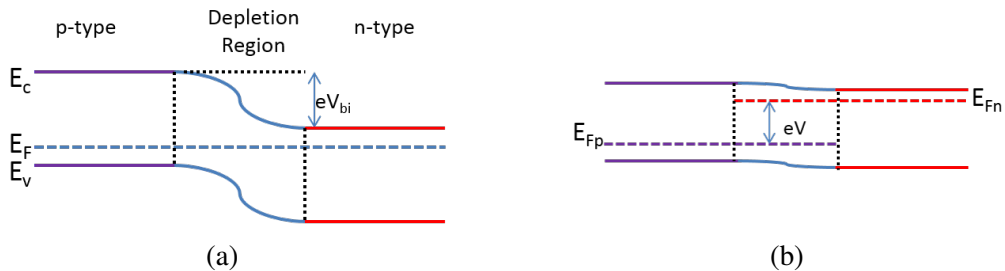


Fig. 1.14 a) *p-n* junction at equilibrium, with the conduction band, Fermi level and valence band denoted E_c , E_F and E_v respectively, the built in potential across the junction is denoted as V_{bi} b) under forward bias of V .

A schematic of a general LED structure is shown in Fig.1.15. Visible light III-nitride LED structures typically contain a magnesium doped *p*-region and a silicon doped *n*-region. An electron blocking layer (EBL) consisting of a material with a higher bandgap than GaN (in this case AlGaN) is often used to prevent the leakage of electrons into the *p*-doped region and confine them in the InGaN QW active region.

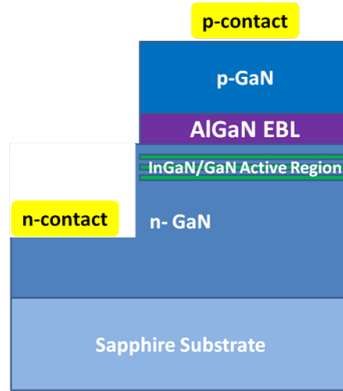


Fig. 1.15 Typical visible light LED structure grown on a sapphire substrate [15].

1.2.2 Microcavities

Microcavity emitters possess rather singular optical properties due to their dimensions. By matching one or more dimensions of the cavity to the order of the wavelength of confined light a plethora of effects can be produced such as low-threshold lasing, directional luminescence and enhanced nonlinear conversion [37]. Confining a dipole within a microcavity can modify its emissive properties by altering the photon density of states. The interaction rate between the confined dipole and a cavity photon relative to the average rate of dissipation of a cavity determines whether the microcavity operates in the weak-coupling or strong-coupling regime.

Weak coupling occurs when dissipation overwhelms the dipole-cavity photon interaction: the effect of the microcavity in this case is to alter the vacuum description of the dipole lifetime, resulting in an increase in spontaneous emission for on-resonance cavity modes, known as the Purcell effect [38]. Weakly-coupled microcavity systems have applications across a wide range of optoelectronic devices due to this effect: from enhancing the recombination rate and extraction efficiency of embedded single photon emitters [39] to the development of high efficiency, low threshold lasers [40].

An interaction occurring on shorter timescales than the average dissipation rate of the cavity photon is defined as being in the strong coupling regime and results in the formation of admixed eigenstates populated by quasiparticles known as polaritons, which are hybrid particles combining a photon and an electric dipole. The bosonic nature of these quasiparticles has led to the observation of spontaneously emitted coherent light from condensates of exciton-polaritons, a phenomenon also known as polariton lasing [41]. The expected threshold energy for coherent emission from a polariton laser is expected to be much smaller than that of a conventional laser due to the lack of the requirement of population inversion , thus rendering polariton lasers extremely attractive as low-threshold lasing applications [37].

Beyond polariton lasing, strong coupling in microcavities is also required for key quantum information processing tasks such as the entanglement of distinguishable quantum systems and controlled coherent coupling [42, 43].

Cavity Parameters and Design

The ability of a microcavity to confine light is a crucial parameter in producing the required effects and is known as the cavity 'quality factor' which is described by Eq. 1.8.

$$Q = \frac{v_0}{\delta v_0} \quad (1.8)$$

Where v_0 is the resonant frequency of the cavity mode and δv_0 is the mode bandwidth. Cavity quality factor can be understood as a parameter describing the rate of energy decay the resonant mode undergoes within the cavity and thus may be alternatively described using an exponential characteristic decay constant τ_{cav} as shown in Eq.1.9, where Q^{-1} is the proportion of energy lost during a single cavity round-trip.

$$Q = \pi \tau_{cav} v_0 \quad (1.9)$$

The manner in which the resonant mode fields interact with the cavity geometry is determined by the effective modal volume of the cavity, which is described by Eq.1.10.

$$V_{eff} = \int_V \frac{\epsilon_0(\mathbf{r}) |\mathbf{E}(\mathbf{r})|^2}{max[\epsilon_0(\mathbf{r}) |\mathbf{E}(\mathbf{r})|^2]} dV \quad (1.10)$$

where $|\mathbf{E}(\mathbf{r})|^2$ is the normalised electric field amplitude, ϵ_0 is the dielectric constant and V is the quantization volume. V_{eff} describes the manner in which cavity supports the distribution of the resonant mode, thus in some cases a large evanescent field component must be included in the calculation of the modal volume.

Cavities often support more than one optical mode, which gives rise to another parameter, known as the free spectral range (FSR), which is defined as the frequency spacing between successive resonant modes. This parameter is crucial to lasing cavities as the probability of photon into a lasing mode is affected by the number of modes supported by the cavity. The FSR as well as parameters needed to define cavity quality factor are shown schematically in Fig.1.16.

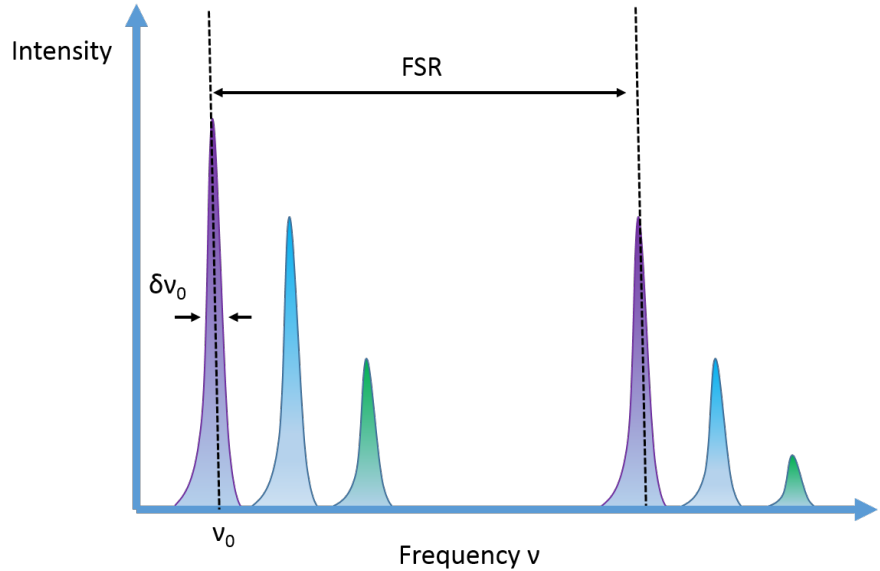


Fig. 1.16 Illustration of the some key parameters such as FSR and resonant cavity mode FWHM.

Cavities modify the optical density of states of an emitter through the generation of standing electromagnetic waves. There are several manners through which to achieve this: at the most basic level an optical cavity is a set of single reflective interfaces, spaced at a specific distance designed to enhance a particular optical mode. However, many cavity designs which employ the use of refractive index mismatches for total internal reflection or an array of boundaries leading to interference enhanced optical modes also exist, as shown in Fig.1.17.

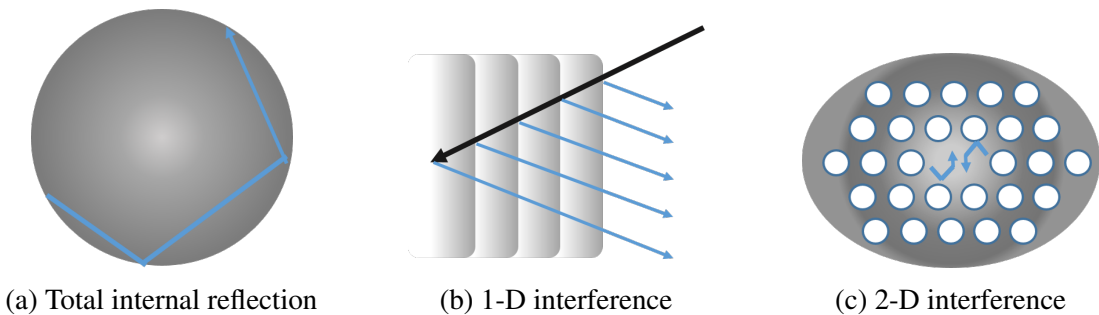


Fig. 1.17 Optical resonators.

Microdisk Cavities

Total internal reflection can be exploited in circular geometries such as microdisk/ring/sphere devices, in which whispering gallery modes (WGMs) propagate around the periphery of the disk.

Microdisks can be described as a cylinder of with a low height:radius ratio supported by a pillar of a small radius (less than half of the cylinder). The position of the WGMs is described by Snell's law: only light satisfying the condition described by Eq.1.11 is contained within the microdisk due to internal reflection.

$$\theta_c = \sin^{-1}\left(\frac{n_2}{n_1}\right) \quad (1.11)$$

Assuming the microdisk thickness is small enough to act as a waveguide in the vertical direction, we can consider the propagation of a ray of light in 2-D as in Fig.1.18. The forbidden position of the WGMs as defined by Eq.1.11 is given by R_{min} .

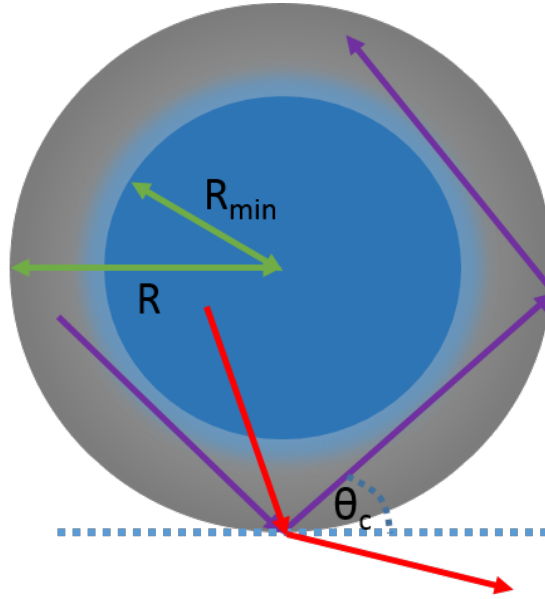


Fig. 1.18 Illustration of the minimum radius R_{min} for WGM propagation. Rays traversing the region $r < R_{min}$ (denoted in red) exceed the critical angle θ_c and thus escape the cavity. Rays travelling outside this region $r > R_{min}$ (denoted in violet) are confined.

Thus the fabrication of microdisks relies heavily on the ability to 'undercut' the microdisk material whilst still leaving a pedestal, as shown in Fig.1.19. This is a particularly challenging problem issue in terms of III-nitride materials due to the excellent thermal and chemical stability of GaN. Early efforts in microdisk nitride fabrication involved dry-etching processes, utilising the refractive index mismatch between the light emitting GaN layers and the

sapphire substrate to confine light [44]. Although stimulated emission and lasing was observed by Chang *et al.* in dry-etched GaN microdisk cavities [45], Haberer *et al.* [46] reduced the required excitation power densities for lasing by an order of magnitude by employing photoelectrochemical (PEC) etching to undercut GaN microdisks, thus providing superior optical confinement due to the index contrast of the GaN/air interface relative to the GaN/sapphire interface used by Chang *et al.* [45]. Further improvements in fabrication were achieved by Tamboli *et al.* with room temperature lasing achieved in GaN/InGaN microdisks through enhancements in microdisk circularity and sidewall smoothness [44].

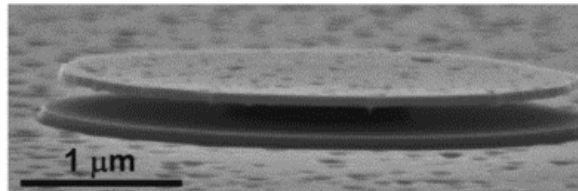


Fig. 1.19 Scanning electron microscope image of a GaN microdisk produced by selective etching of sacrificial AlInN layers [47].

Nanobeam Cavities

Photonic crystals are periodic structures which affect photons in a manner analogous to the way atomic lattices affect electrons in solids. They can be considered as artificial materials exhibiting a dielectric function which varies periodically in either one, two or three dimensions. The principal mechanism of light confinement in this case is known as distributed bragg reflection as is shown in Fig.1.17b).

Whilst micro-toroid and microdisk cavities have the potential to achieve extremely high Q-factors many applications which involve strong coupling, non-linear optical processes and spontaneous emission and other similar processes require a high ratio between the Q-factor and the effective modal volume (V_{eff}). This figure of merit can be achieved in travelling-wave cavity geometries due to the potential for extremely small modal volumes. Yablonovitch [48] and John [49] first proposed the design of 3-D photonic crystal cavities which in theory would possess ultra-high Q-factors, minute modal volumes and perfect reflectivity in all directions. Despite the extremely promising theoretical properties of 3-D photonic crystal cavities, their fabrication has proven to be particularly challenging with few demonstrations of high-Q 3-D PCCs reported in literature [50], [51]. PCCs of lower dimensionality are thus prime candidates for practical applications due to fewer (though not vanishing!) fabrication issues. In particular 1-D PCCs such as suspended structures known as nanobeams are extremely promising due their ability to realise of high-Q, low V_{eff} cavities even in low index materials

such as SiO_2 [52]. For these reasons we will specifically be considering 1-D photonic crystal cavities in the nanobeam geometry in this work.

Electromagnetic field confinement is achieved in nanobeam structures by Bragg scattering from the photonic crystal in one direction, and index guiding in the other two directions. A nanobeam can essentially be considered as a wavelength-scale Fabry-Perot cavity with photonic crystal mirrors [53]: as the nanobeam waveguide mode is trapped and reflected by these mirrors, it also penetrates some distance into them. If the fields terminate at the mirror boundaries, this would lead to large scattering losses due to the large impedance mismatch [54]. In order to avoid this impedance mismatch between the waveguide mode and the Bloch mode of the mirror, the photonic crystal mirrors are tapered in order to match the evanescent mirror Bloch mode [55] as shown in Fig.1.20.

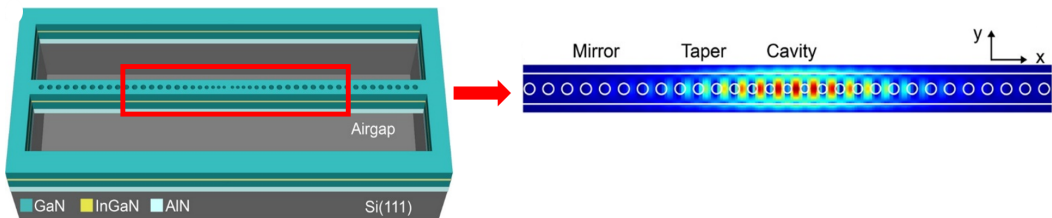


Fig. 1.20 Nanobeam schematic and 3-D FDTD simulation of the electric field intensity profile of the cavity mode adapted from [56].

Despite the promise of large $\frac{Q}{V_{eff}}$ ratios and potential applications ranging from bio-photonics to optical communications, processing issues have hindered the development of III-nitride based photonic crystal cavities, similarly to the development of microdisk cavities discussed earlier. Indeed, the first high-Q (2400) III-nitride photonic crystal cavity was demonstrated in 2007 by Arita *et al.* [57]. In terms of 1-D nanobeam cavities, Pernice *et al.* reported AlN nanobeam cavities with measured Q-factors of approximately 146000 close to standard telecommunication wavelengths of $1.55 \mu m$ [58]. Sergent *et al.* demonstrated a high Q (6.3×10^3) optically active nanobeam cavity with embedded GaN/AlN quantum dots using a layer transfer method rather than the traditional PEC undercut. More recently, continuous wave blue lasing was demonstrated at 460 nm in GaN nanobeams with an InGaN QW active region grown on silicon, where the reported Q-factor was 10^4 . Ultra-low threshold ($9.1 \mu J/cm^2$) lasing was also reported by Niu *et al.* in GaN nanobeam cavity structures with a fragmented InGaN QW active layer which provided additional confinement for photo-generated carriers relative to continuous QW active layers [59].

1.2.3 Nanowires for Nanophotonic Devices

The lack of readily available, low-cost substrates for the epitaxial growth of GaN and its associated alloys has motivated research into the growth of III-nitrides in nanowire geometries. Studies have shown that epitaxial GaN nanowires can be grown with far lower dislocation densities relative to bulk GaN due to a large surface-to-volume ratio. Furthermore, QWs grown radially along the non-polar facets of nanowires allow for the reduction of the polarization fields which can deleteriously affect the optical properties of polar III-nitride emitters without the need for expensive non-polar substrates.

Beyond the material benefits of the nanowire growth geometries in the III-nitrides, the reduced dimensionality of nanowires will potentially allow for the realisation of highly efficient, low-threshold compact light sources for applications such as information processing and optical communications [60]. As such, nanowires may provide a solution to one of the most challenging areas of modern optoelectronics: the miniaturisation of active optoelectronic components. In terms of their employment as active optoelectronic components, nanowires have the additional benefit of having to intrinsic mirrors in the form of their crystalline end-facets thus naturally forming cavities. Due to the increasingly demanding nature of modern optoelectronic device development, research into nanowire devices is currently an extremely active area of research.

The first demonstration of GaN nanowire based lasing was reported by Johnson *et al.*, who demonstrated lasing at wavelengths of 370-380 nm at a threshold of approximately 700 nJ/cm^2 [61]. Progress in the epitaxial growth of heterostructure nanowires lead to the demonstration of InGaN/GaN MQW nanowire lasing in 2008 by Qian *et al.*, by varying the indium composition of the MQW structures lasing at wavelengths ranging from 380 to 478 nm was achieved [62]. Whilst both these demonstrations of nanowire lasing were achieved by using the simplest cavity geometry (Fabry-Perot), polariton lasing in GaN nanowires was demonstrated by Das *et al.* by strongly coupling a single GaN nanowire to a large-area dielectric microcavity [63]. Alternative cavity coupling designs have since been expanded to include plasmonic coupling, first demonstrated in InGaN/GaN nanowires by Wu *et al.* by coupling a bundle of GaN/InGaN nanowires to a gold plate through a dielectric nanogap layer [64]. These nanowire laser applications are shown schematically in Fig.1.21

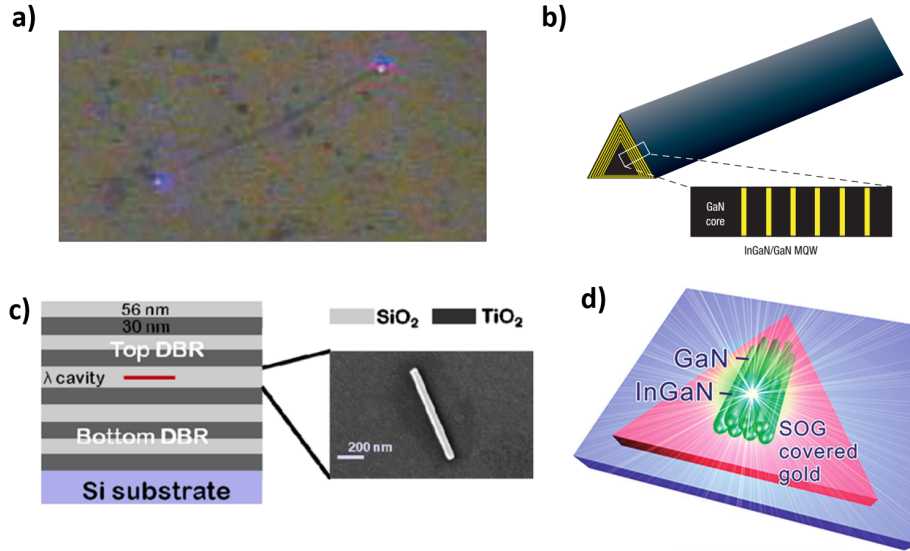


Fig. 1.21 a) Lasing from the end-facets of a GaN nanowire b) schematic of the triangular InGaN/GaN MQW nanowire grown by Qian *et al.* c) GaN nanowire coupling to a dielectric cavity d) GaN/InGaN nanowire bundle coupling to a gold plate through a nanogap layer. Adapted from [61–64] respectively.

Nanowire single photon sources have also been achieved, due to the benefit of site-controlled quantum dots. Electrically injected blue single photon sources based on III-nitride nanowires have been reported by Deshpande *et al.* operating at 10 K. In this particular case, an InGaN QD was incorporated into a *p-n* GaN nanowire as shown in Fig. 1.22.

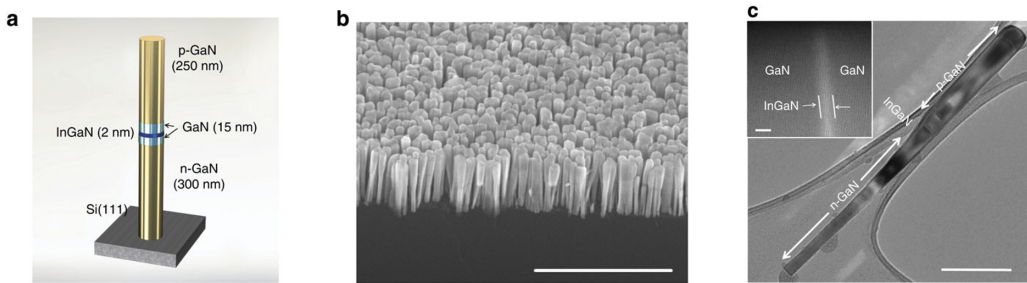


Fig. 1.22 a) Schematic of the InGaN QD in GaN nanowire structure b) SEM micrograph of the nanowire sample grown by MBE c)TEM micrograph of a single nanowire. Adapted from [65].

Holmes *et al.* have also demonstrated room temperature triggered single photon emission from a GaN QD grown in a GaN/AlGaN core-shell nanowire as shown in Fig.1.23.

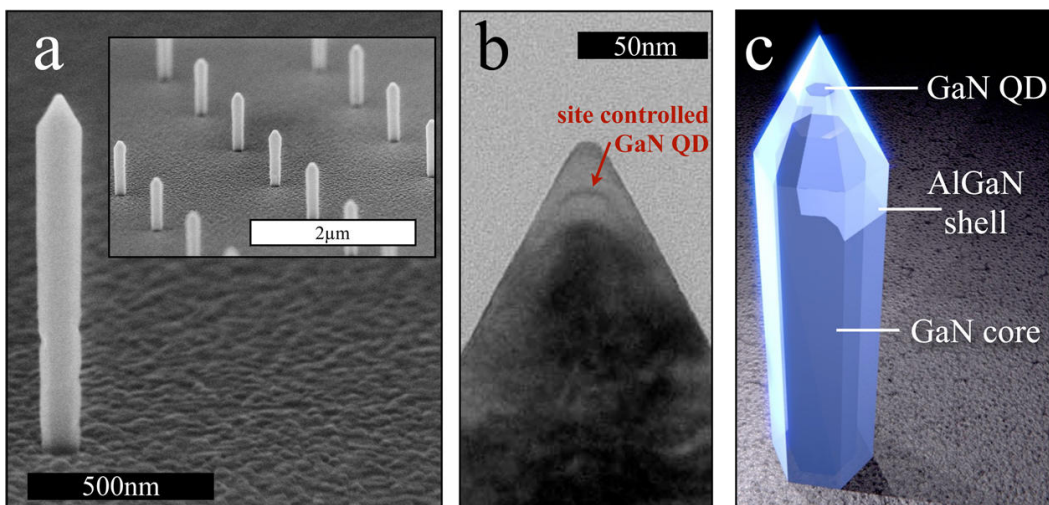


Fig. 1.23 a) SEM micrograph showing the a single nanowire on a patterned SiO_2 substrate grown by MOCVD. The inset shows the array of nanowires grown on the substrate b) showing the site-controlled GaN QD at the tip of the nanowire c)schematic of the nanowire structure [66].

Chapter 2

Experimental Methods

2.1 Transmission Electron Microscopy

A typical transmission electron microscope (TEM) consists of a high voltage (typically 100-400kV) electron gun under extremely high vacuum conditions within a column. The beam of electrons generated by this gun passes through a set of lenses which focus or deflect the beam before it is incident on the sample under examination. If this sample is thin enough to be electron transparent, the electrons passing through it and scattering elastically or inelastically can be collected using a subsequent set of lenses, apertures and a detector. A simplified schematic of a TEM illumination system is shown in Fig.2.1:

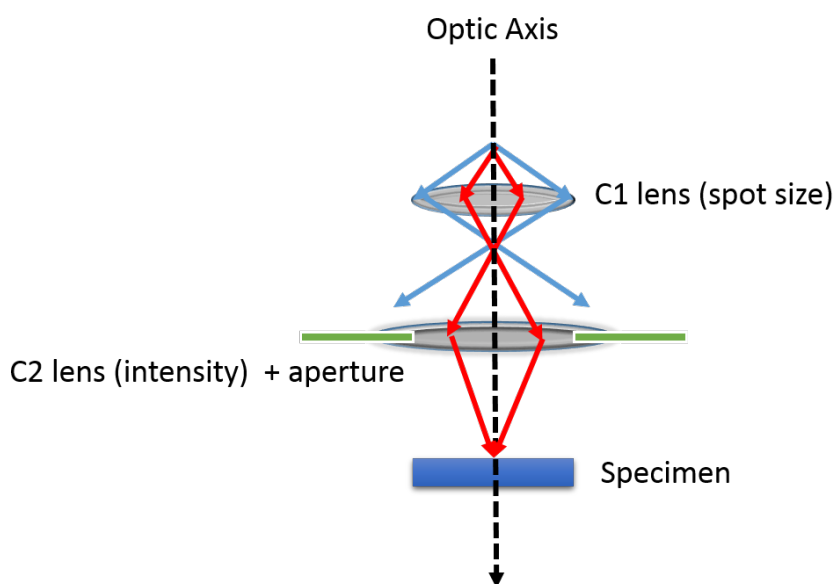


Fig. 2.1 Simplified TEM illumination system.

It is important to consider the range of electron-specimen interactions which occur as the high energy electron beam impact the sample. These interactions can be divided into two main categories according to whether the electron kinetic energy is either conserved or not during the interaction, known as elastic or inelastic respectively. Different elastic and inelastic signals produced by the electron-specimen interaction are illustrated in Fig.2.2.

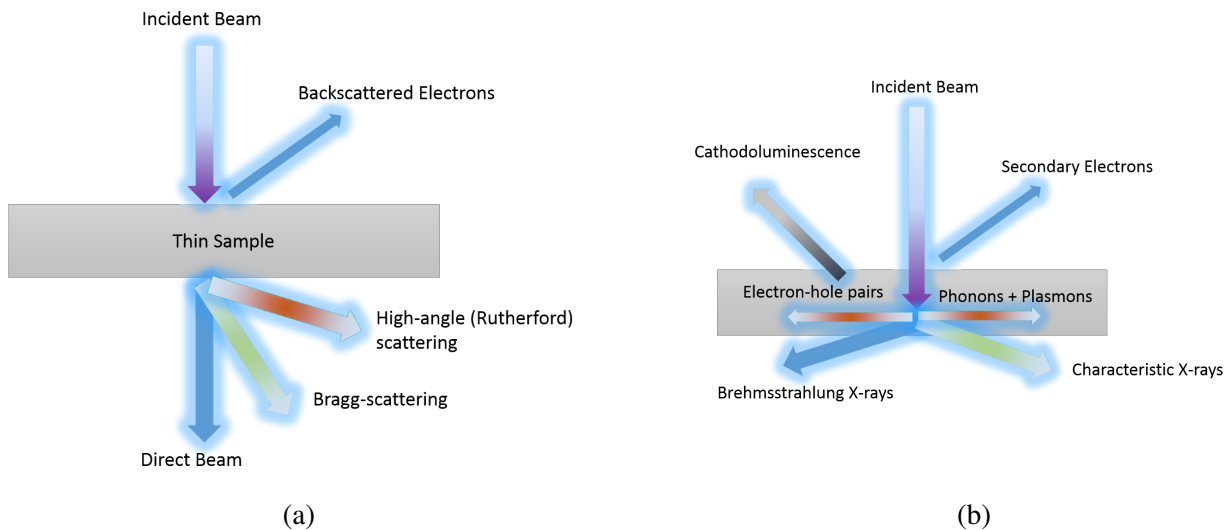


Fig. 2.2 a) Elastic and b) inelastic interactions for a high energy electron beam incident on a thin sample.

Fig.2.2 a) illustrates the importance of sample thickness in TEM. Without a thin specimen, the forward scattered signals such as high-angle and bragg-scattered electrons as well as the direct beam are unavailable. Given the diversity of scattering interactions which can occur throughout the sample and contribute to the final signal, different apertures and detectors must be used to extract useful information. The following sections will introduce the different TEM techniques used in this report and their underlying principles.

2.1.1 Conventional Transmission Electron Microscopy

Electron Diffraction

Electron diffraction is the basis for many TEM techniques as it provides local crystallographic specimen information. The process of diffraction occurs for electrons due to their dual nature as both particles and waves. A beam of electrons can thus be interpreted as a plane wave: the incidence of this plane wave on the specimen results in the scattering of the electrons by atoms through the Coulomb interaction, diffracting the wave in a manner described by Bragg's law. This is given by Eq. 2.1.

$$n\lambda = 2d_{hkl}\sin\theta_B \quad (2.1)$$

where n is an integer, λ is the wavelength of the plane wave, d_{hkl} is the crystal plane spacing described by the Miller indices h, k and l and θ_B is the angle between the plane normal and the scattered wave, also known as the Bragg angle.

Understanding of the diffraction patterns observed in TEM requires consideration of the reciprocal lattice of the crystal. The reciprocal lattice is defined as the Fourier transform of the crystal lattice, as such the relation of the real-space unit-cell lattice points \mathbf{a} , \mathbf{b} and \mathbf{c} to their reciprocal lattice counterparts \mathbf{a}^* , \mathbf{b}^* and \mathbf{c}^* can be described as:

$$\mathbf{a}^* = \frac{\mathbf{b} \times \mathbf{c}}{V_c}, \mathbf{b}^* = \frac{\mathbf{c} \times \mathbf{a}}{V_c}, \mathbf{c}^* = \frac{\mathbf{a} \times \mathbf{b}}{V_c} \quad (2.2)$$

where V_c is the volume of the unit cell and is given by the relation"

$$V_c = \mathbf{a} \cdot \mathbf{b} \times \mathbf{c} \quad (2.3)$$

As such one can define lattice points in reciprocal space which are normal to the plane (hkl) in the real lattice as:

$$r^* = h\mathbf{a}_1^* + k\mathbf{a}_2^* + l\mathbf{a}_3^* \quad (2.4)$$

where \mathbf{a}_1 , \mathbf{a}_2 , \mathbf{a}_3 and \mathbf{c} are the four hexagonal unit-cell vectors as shown in Fig.2.3.

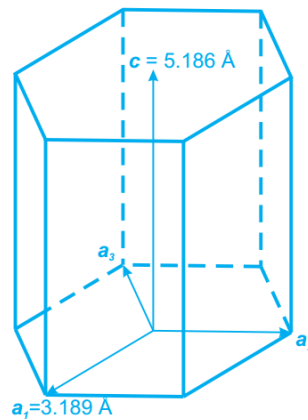


Fig. 2.3 Hexagonal GaN lattice in real space with unit-cell vectors defined. Adapted from [67].

Considering a beam of electrons of wavelength λ incident on a crystal lattice, one can define a sphere in reciprocal space with radius $\frac{1}{\lambda}$ which describes the scattering of the

electron beam known as the Ewald sphere. The intersection of the Ewald sphere with lattice points in reciprocal space represent the diffraction spots which can be observed. Typically, the geometry of the TEM specimen results in elongated reciprocal lattice points known as rel-rods. This elongation allows the Ewald sphere to intersect a greater number of 'points', even with slight deviations to the Bragg condition. The scattering vector \mathbf{K} can thus be described as:

$$\mathbf{K} = \mathbf{k_D} - \mathbf{k_I} = \mathbf{g} + \mathbf{s} \quad (2.5)$$

where $\mathbf{k_D}$ and $\mathbf{k_I}$ are the diffracted and incident beam wavevectors respectively, \mathbf{g} is a reciprocal lattice point intersecting the Ewald sphere and \mathbf{s} is the excitation error, which describes how far the scattering deviates from the exact Bragg diffraction condition. These concepts are shown schematically in Fig.2.4.

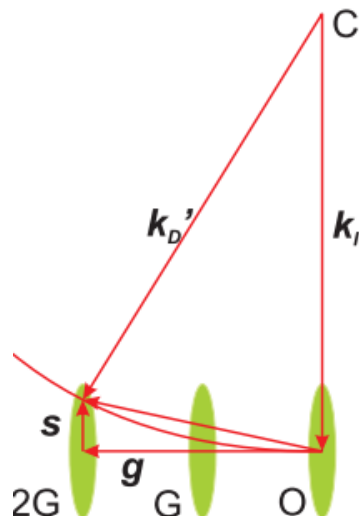


Fig. 2.4 Intersection of the Ewald sphere centered at C with reciprocal lattice rel-rods. Adapted from [67].

Due to the small value of λ (typically picometres), the radius of the Ewald sphere tends to be large relative to the reciprocal lattice spacing, meaning the surface of the sphere is approximately planar relative to the reciprocal lattice rods thus resulting in several spots being observed even in cases where the incident beam is parallel to the zone axis.

Diffraction Contrast Imaging

Diffraction contrast imaging is a conventional TEM technique which exploits differing Bragg diffraction conditions in different regions of the sample to create contrast in an image. Image

contrast can be obtained either through bright field (BF) or dark field (DF) imaging, these are shown schematically in Fig 2.5 below:

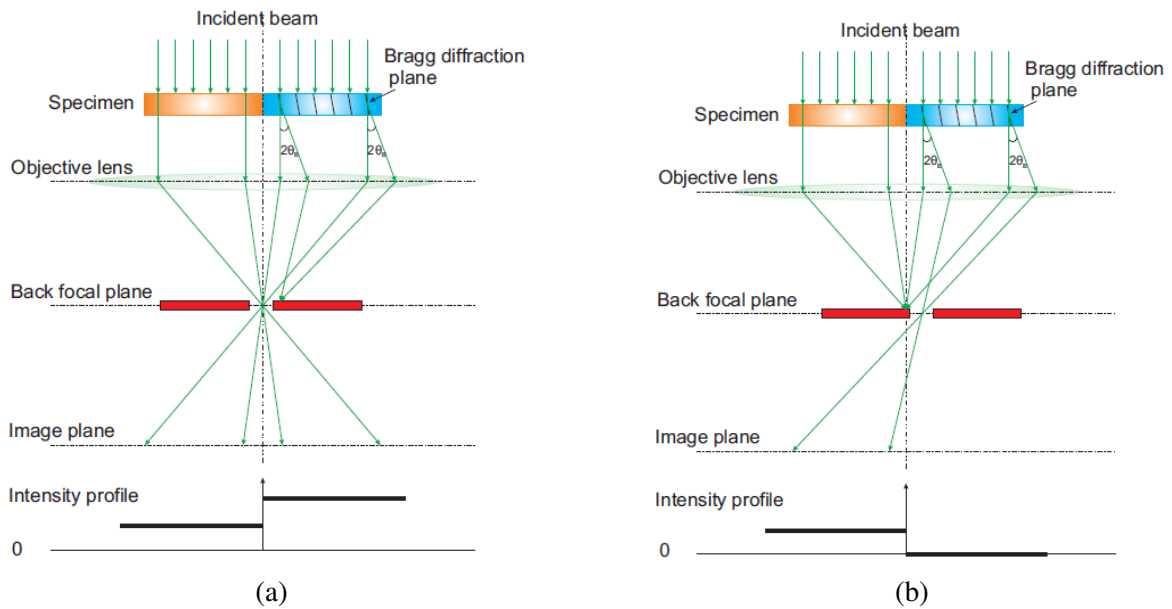


Fig. 2.5 a) Bright-field and b) dark-field imaging [67].

The blue region is shown to satisfy the Bragg diffraction condition for the incident beam whereas the orange region does not. In the case of BF imaging the direct beam is used to generate the image, and as a result the intensity from the orange region is higher than that of the blue region. On the other hand, in DF imaging the diffracted beam is used and the direct beam blocked, resulting in an inverted intensity profile. Barring other electron-specimen interactions such as absorption, the contrast between the BF and DF images is complementary [68].

Figures 2.5 a) and b) demonstrate that the insertion of an aperture at the back-focal plane (BFP) of the objective lens allows for the selection between BF and DF imaging. Without the objective aperture the image consists of a superposition of BF and DF images with a single DF image for every diffracted beam. In order to ensure the diffracted beam is at the optic axis where spherical aberration of the objective lens is less pronounced the incident beam is often tilted, a practice known as centred dark field (CDF) imaging. As dislocations in a crystal structure can be found near strained crystal planes, these will result in diffraction contrast in BF or DF images. However it is important to consider that many diffraction spots can be observed in the electron diffraction pattern, which is undesirable for BF or DF contrast imaging. As such the optimal conditions for are defined as the two-beam condition, in which only one set of planes satisfies the Bragg condition [68], resulting in two beams: the

direct beam and the sole diffracted beam. Under the two-beam condition, image contrast is optimized and the intensity of the two beams can be analytically calculated using the Howie-Whelan equations [68] to deliver detailed information concerning the specimen through the interpretation of contrast in the image.

Weak-Beam Dark-Field Microscopy

An alternative technique known as weak-beam dark-field (WBDF) imaging is often used to image dislocations. As indicated by its name, the technique uses a weakly excited beam to form a DF contrast image. A particular diffraction vector \mathbf{g} associated with a specific set of planes hkl is chosen as in regular on-axis DF imaging. The specimen is then tilted to introduce a large excitation error s_g and bring the first diffraction order G onto the optic axis, in doing so the $3G$ reflection satisfies the Bragg diffraction and appears brighter, whilst the zero-order beam is very weak as shown schematically below:

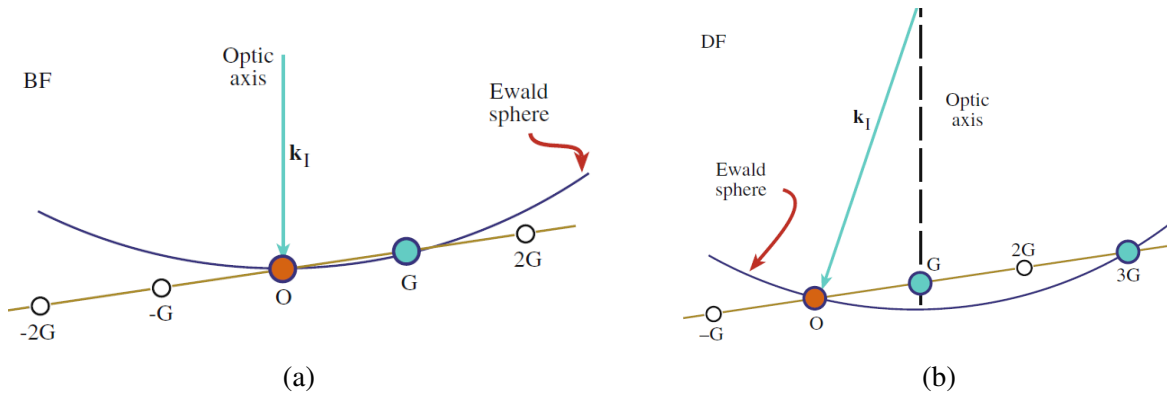


Fig. 2.6 Specimen is tilted from a) to b) for the $g-3g$ condition [68].

As such, most of the lattice planes within the specimen are rotated away from the Bragg condition but near the cores of dislocations these are bent back and appear as high intensity features. The high contrast enables highly detailed imaging of dislocations [68], as shown in Fig.2.7.

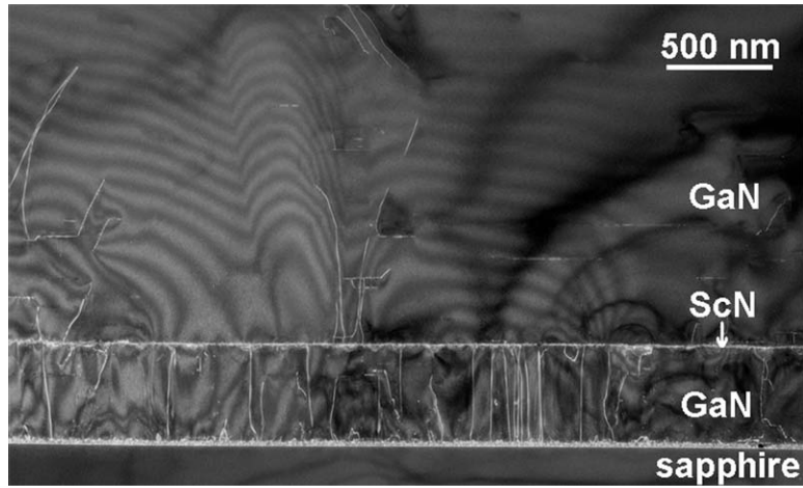


Fig. 2.7 WBDF imaging of dislocations [69].

2.1.2 Scanning Transmission Electron Microscopy

Scanning transmission electron microscopy (STEM) differs from conventional TEM in that a converged electron beam is utilised to generate an image as opposed to a parallel incident beam as described in section 2.1.1. The convergence of the electron beam generates a probe which can be as small as several angstroms which is focused and scanned across the sample. Each pixel in the image generated by this technique is acquired from the probe in a separate position by collecting radiation emitted from the sample generated by irradiation from the beam.

A critical parameter in STEM is the brightness of the source which determines the current in the electron probe. Consequently, field emission guns (FEG) are favoured over thermionic guns such as tungsten or LaB_6 for use in STEM. Another factor which contributes to the preference for FEGs in STEM is the increased spatial localisation of the electron emission compared to thermionic sources, which allows for a smaller probe.

The probe in STEM is a demagnified image of the crossover from the electron gun. The figure below illustrates how a strong gun lens results in a cross over close to the gun such that fewer electrons travel through the collector aperture, leading to a smaller probe with a lower current on the sample.

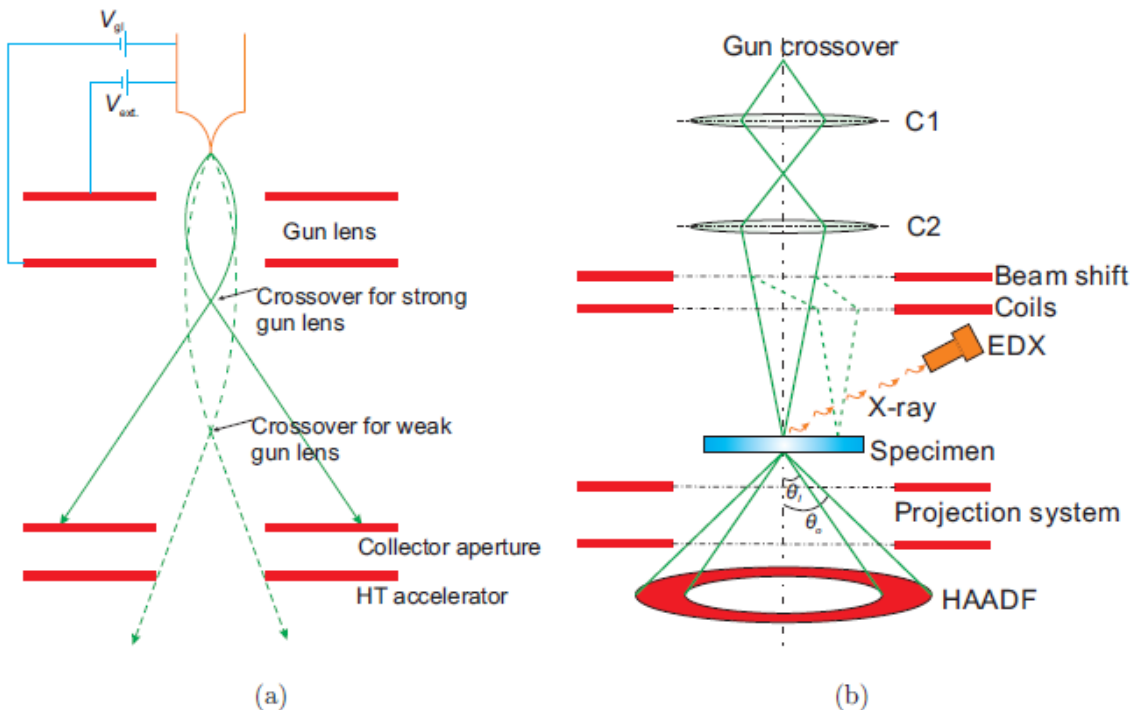


Fig. 2.8 Illustration of a) the FEG source and gun lens b) the column of a STEM with a HAADF for z-contrast imaging and EDX detector [67].

As different STEM techniques such as high-angle annular dark-field (STEM-HAADF) imaging, energy dispersive X-ray spectroscopy (STEM-EDX) or convergent beam electron diffraction (STEM-CBED) imaging will require different probes for optimal results, the strength of the gun lens allows for the adjustment of the required parameters [68].

STEM-HAADF is a STEM technique which allows for what is commonly known as Z-contrast imaging, or imaging by atomic number. The basic principle of operation relies on the fact that electrons scattered by atoms at relatively large angles are mostly incoherent and can be considered as particles rather than waves. At high angles, the intensity of the scattered electrons is proportional to the square of the atomic number Z [70] thus allowing the determination of atomic number of the material at the location of the probe from the brightness of the collected signal. Thus, the use of a high-angle annular dark-field detector allows for the collection of electrons scattered at high angles and the reduction in electrons scattered at low angles, as shown in Fig 2.8 b). The magnification in STEM-HAADF imaging is controlled by varying the size of the area scanned by the probe, rather than through the use of lenses as in conventional TEM. Strong contrast is typically obtained in HAADF images of III-nitride heterostructures due to the large difference in atomic numbers between the group III elements.

2.1.3 Energy-Dispersive X-ray spectroscopy

Electron-induced X-ray emission allows for the characterisation of sample composition. The high-energy electron beam incident on the sample in TEM can lead to the ionisation of electrons of the inner orbitals, generating vacancies. As electrons from higher energy orbitals relax into this vacancy a characteristic X-ray is released, with an energy equal to the difference between the two states involved in the relaxation transition.

Siegbahn notation is used to describe characteristic X-ray lines: the first component is the elemental atom emitting the X-ray, second is the electron shell which was ionized to emit the X-ray (K, L or M) and the final component describes the relative intensity of the line for each shell (in order of decreasing intensity: α, β, γ) [71]. These are shown schematically in Fig. 2.9

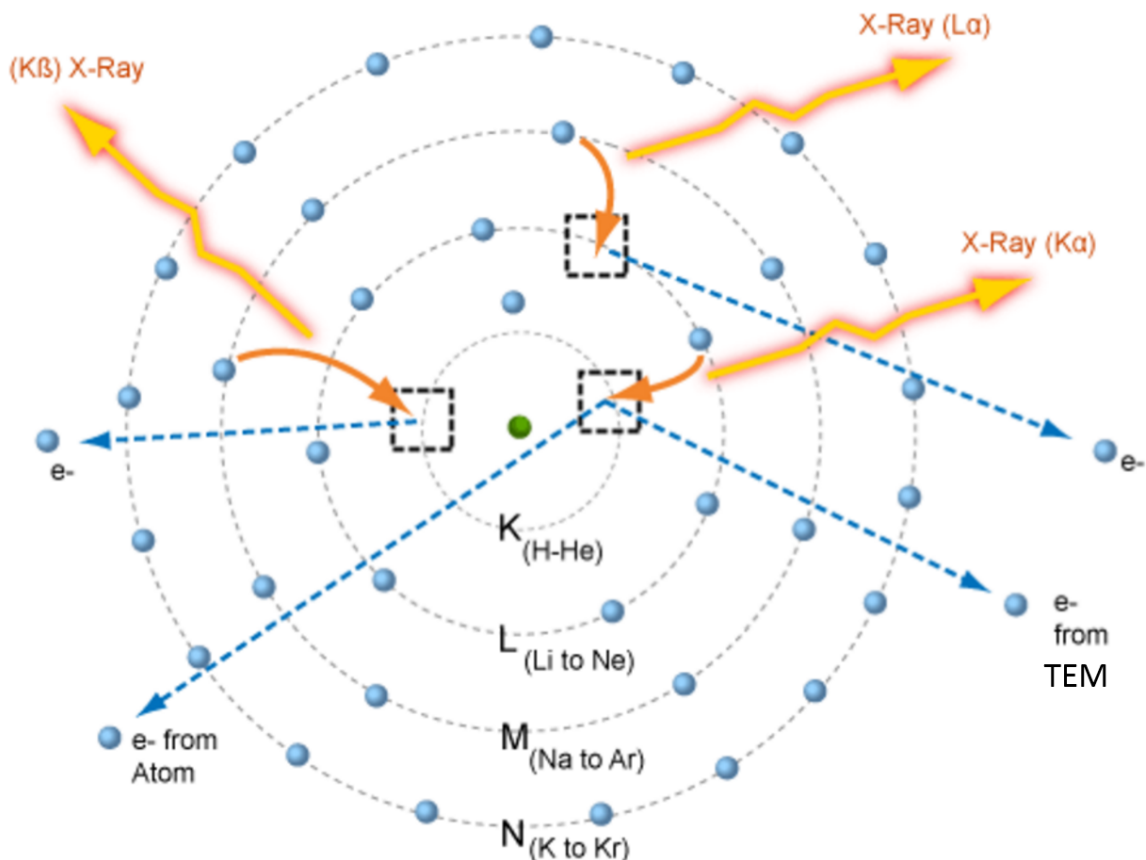


Fig. 2.9 K_α , K_β , and L_α X-rays and their associated electronic transitions. Adapted from [71]

These characteristic X-rays can be collected using an energy dispersive detector, where the X-rays generate electron-hole pairs in a silicon *p-i-n* junction.

Energy-Dispersive X-ray spectroscopy (EDX) is typically used in STEM mode, where the

electron beam is condensed into a small probe, which leads to the majority of the X-rays being emitted from a small volume in the sample. This enables the acquisition of spatially resolved elemental maps.

2.2 Electron Tomography

TEM provides a plethora of techniques with which to characterise nano-scale structures, however it is often insufficient to ascertain the 3D morphology of complex structures as it deals with projections of the specimen. A typical example of this is network of super-imposed particles in which particles overlapping in the projection may not in fact be in contact in real space [72].

Tomographic reconstruction is a technique that has been widely used to infer 3D volumes from series of 2D projections. A prime example of this is computed axial tomography scanning (CAT-scanning), a technique that has become prevalent in healthcare. The first demonstration of tomography applied to electron microscopy was reported at the MRC laboratory in Cambridge by De Rosier and Klug [73]. Since then, electron tomography (ET) has progressed in leaps and bounds due to advances in technology pertaining to both microscopy and tomographic reconstruction.

The fundamental tenet of tomography lies in the projection theorem developed by Radon at the dawn of the 20th century. The implication of the theorem is that the acquisition of a set of projected images of an object at varying angles can allow for the reconstruction of the full 3D Fourier transform of said object, and consequently the morphology of the object in real space [72] as shown in Fig.2.10.a)

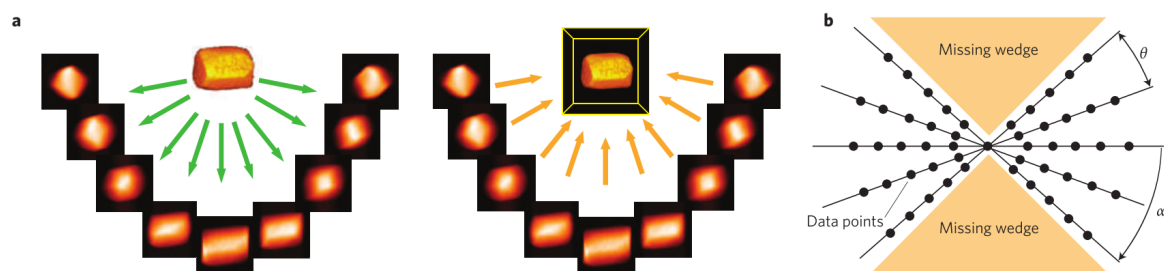


Fig. 2.10 Two-stage tomography process: a tilt series of an object is acquired, then the back projection of these images is used to reconstruct a 3D model of the object [74].

In practical terms, the angular range of the tilt series is an important consideration. A full tilt series acquired between the range $\pm 90^\circ$ allows for minimal anisotropy artifacts. However, typical TEM stage and holder combinations will only allow for a range of $\pm 78^\circ$ due to the

pole-piece gap, leading to a missing wedge of data which results in distortion in the 3D reconstruction [75]. Despite these issues, it has been shown that for tilt ranges larger than $\pm 75^\circ$, the elongation of features due to the missing wedge is below 10% and the volume fraction estimate is within experimental error as other factors such as the interval between images in the series and post-processing can also influence the accuracy of the reconstruction [76].

In order for the reconstruction to be successful, the signal used in the tilt-series must depend monotonically on the thickness of the sample (or some other physical property) [77]. In the case of HAADF-STEM imaging, this is true as the signal intensity depends both on specimen thickness and atomic number.

2.3 Atomic Force Microscopy

Atomic force microscopy is a non-destructive characterisation technique which employs a sharp tip mounted on a cantilever which is rastered across a sample surface. Tip-surface interactions result in changes cantilever position which are measured using the reflection of laser light reflecting off the cantilever and a four-quadrant photodetector as shown in Fig.2.11.

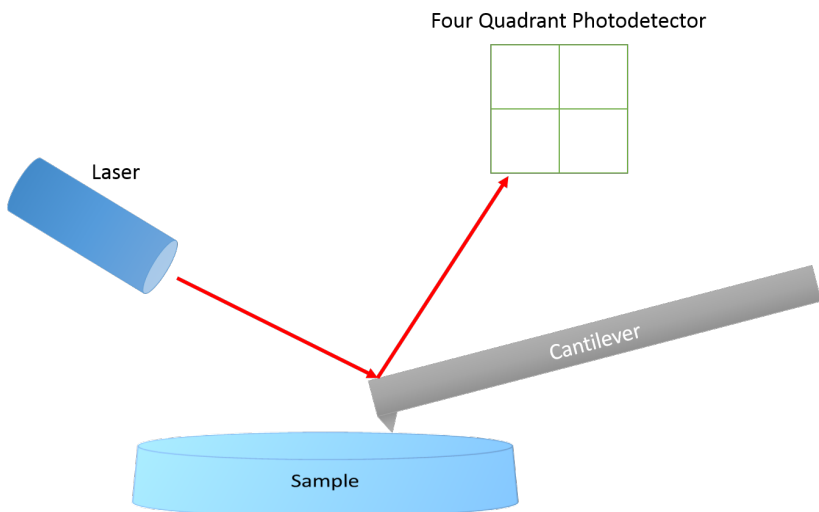


Fig. 2.11 Schematic of an atomic force microscope.

The positioning and movement of the tip is achieved through the use of piezo-electric actuators. In contact mode, a feedback circuit is used to apply a voltage to the piezoelectric crystal in order to maintain a constant tip-sample separation should the tip encounter any features, thus avoiding damage to either the tip or sample. The voltage required to maintain

this distance (also known as the setpoint) is registered at each pixel of the scan and is used in conjunction with calibration data to determine a vertical displacement value, thus generating a topographic image.

An alternative mode of operation known as tapping mode is often referred to contact mode. In this mode of operation the tip is made to oscillate close to its resonant frequency by the piezocrystal. Contact between the tip and the sample is achieved at the lowest point of each oscillation, which damps the oscillation of the tip. The oscillation frequency is maintained by the piezoelectric crystal, thus allowing for the generation of a topographic map. Tapping mode is often preferred to contact mode due to the exclusion of lateral friction which can cause tip wear and sample damage.

The forces experienced by the tip vary depending on the tip-sample separation, as shown in Fig.2.12. Van der Walls forces dominate at large separations attractive the tip to the surface. As the distance is reduced repulsive forces such as hard-sphere repulsion, electron-electron Coulomb interaction and the Pauli-exclusion interaction begin to dominate. The sum of these forces result in cantilever deflection, changing the tip-sample interaction.

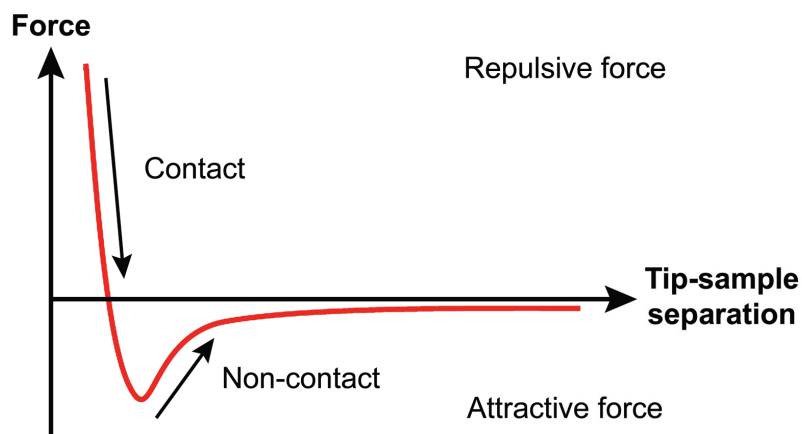


Fig. 2.12 The effect of separation on the tip-sample interaction force [78].

AFM offers excellent vertical resolution limited only by the probes vertical movement and external noise. However, the lateral resolution of this technique is heavily dependent on the shape and size of the tip employed. This is highlighted by Fig.2.13 which depicts a hemispherical tip scanning across a flat-topped island. The apex of the tip is in contact with the surface, but the side of the island also experiences some contact: in this case there is a distinction between the two cases shown in Fig.2.12a) and b) as the error in the measured width of the island varies based on the relative size of the measured object to the tip.

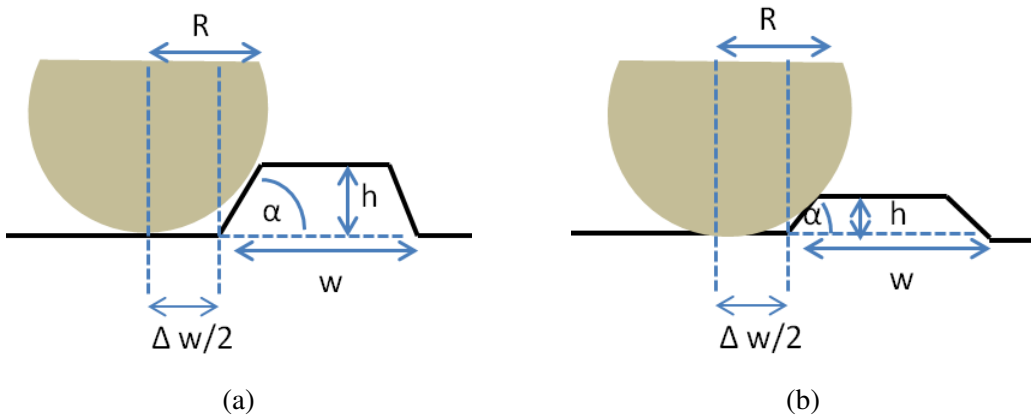


Fig. 2.13 Interaction of a hemisphere with a flat-topped island for the cases a) $h > R(1 - \cos(\alpha))$ and b) $h < R(1 - \cos(\alpha))$ adapted from [79].

Similarly, when measuring depth rather than height the ability of the tip to penetrate into the spaces being measured is also a crucial consideration, as shown in Fig. 2.15. Thus, increasing the gradient of the tip and minimizing the tip apex are desirable to reduce tip-related measurement artefacts when performing atomic force microscopy.

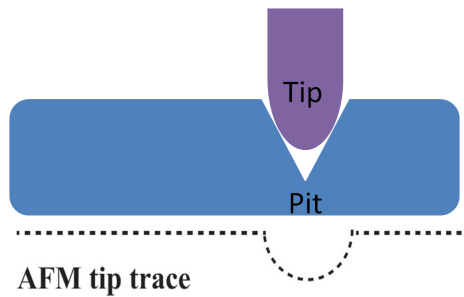


Fig. 2.14 Measurement error in the depth of a pit caused by the finite width of the AFM tip.

Conductive Atomic Force Microscopy

Conductive atomic force microscopy is a technique which combines AFM with local conductivity measurements. In order to perform C-AFM a conductive probe tip is brought close to contact with the sample and a bias is applied between the tip and the sample. The short tip-sample separation causes electron wavefunctions in the tip and sample to overlap, thus allowing a tunneling current to be generated through the application of a bias. C-AFM thus allows for the simultaneous measurement of tip-sample current flow and surface morphology, making it an extremely powerful tool to probe local sample conductivity.

2.4 Scanning Electron Microscopy Techniques

A scanning electron microscope (SEM) employs the use of electrons to characterise material morphology and composition. A schematic of a typical SEM design is shown in Fig.2.15.

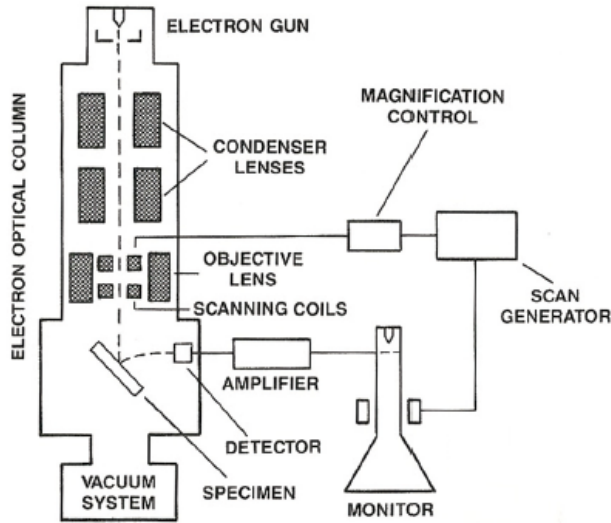


Fig. 2.15 SEM design [80].

The electron gun generates a beam of electrons, typically of energy up to 30 keV. The condenser lenses situated below the gun serve to determine the probe size by adjusting the demagnification of the beam. The objective lens serves to further adjust this demagnification, and is situated directly above the specimen. The scanning coils raster the electron probe across the sample, and the detector thus builds an image of the specimen by collecting various signals which occur due to the electron-specimen interactions.

As the beam of electrons interacts with the specimen, various processes occur which generate characteristic signals, as shown in Fig.2.16 and previously discussed in Section 2.1. The volume within the sample which contains the energy deposited by the electron beam is known as the interaction volume, the shape and size of which is determined by both the beam energy and sample composition. Inelastic scattering of the electrons results in the production of signals such as secondary electrons (SEs), Auger electrons and characteristic X-rays. Typically, it is the SEs which are used for imaging in SEMs. Elastic scattering can generate back scattered electrons (BSEs), which are collected through the surface on which the beam is incident. Due to the nature of elastic scattering, BSEs have a strong dependence on atomic, and are can thus be used to produce composition-dependent image contrast.

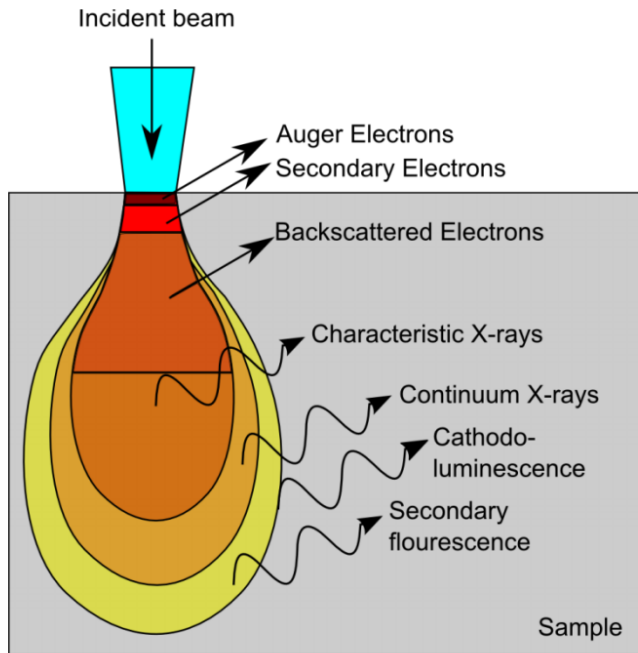


Fig. 2.16 Interaction volumes for different interactions of an electron beam [81].

Cathodoluminescence

The absorption of primary electrons in a semiconductor can generate electronic excitations, or electron-hole pairs, with light emission occurring as a consequence of their recombination. This process is known as cathodoluminescence (CL). The electronic transitions which are associated with CL emission require lower energies than those needed to excite X-rays.

One of the principal advantages of CL in comparison with photo-excitation spectroscopy techniques used on semiconductors is the limitation of the spatial resolution of the technique by the interaction volume of the electron beam in the material rather than diffraction, which can be considered an intrinsic limitation of most optical far-field techniques [82]. As a result, nanometre-scale characterization of materials can be achieved.

Due to the large number of electron-hole pairs generated within the interaction volume of the impinging electron beam on a bulk semiconductor material, all possible transitions within the material tend to be excited, resulting in the crucial limitation of being unable to selectively excite transitions below a certain energy [82]. Nonetheless, the versatility of CL as a technique has been amply demonstrated in its ability to shed light on the composition of compound materials such as InGaN/GaN structures [83], carrier diffusion length and surface recombination rates [84] and even minority carrier lifetimes [80].

A schematic view of a set-up for CL imaging is shown in Fig. 2.17:

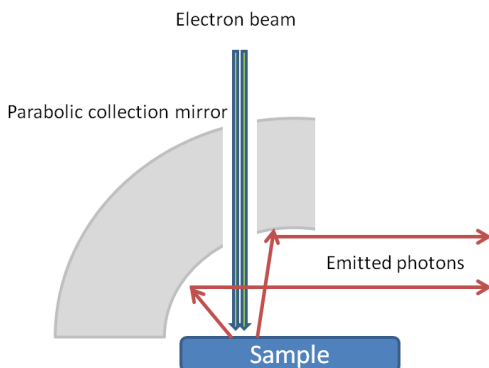


Fig. 2.17 Schematic layout of a CL imaging system.

The electron beam is incident on the sample in the SEM chamber and results in the generation of photons which are collected by a parabolic mirror through a high vacuum feedthrough and coupled into a monochromator. Photomultiplier tubes (PMTs) are the most commonly used detector for this set-up.

The most basic form of CL imaging is known as panchromatic imaging. In this case, the collected light in its entirety is directed to a single detector and the resulting greyscale image intensity is the product of the spectral response of the system and the emission spectrum [82]. An extension of this is the monochromatic imaging mode, in which case only a single band of wavelengths is imaged using a band-pass filter or spectrometer [82].

CL hyperspectral imaging, or CL wavelength imaging is an extension of the aforementioned technique whereby a full luminescence spectrum is recorded at each point during a beam scan, enabling the construction of a spatially and spectrally resolved data set.

In the set-up shown in Fig 2.17, a semi-paraboloidal mirror allows emitted photons to be collected over close to the entire hemisphere. In this case, the beam is scanned across the sample in order to achieve CL hyperspectral imaging, however a number of drawbacks are inherent to this collection geometry:

- The position of the mirror requires a large working distance and can obscure the optical element thus compromising the imaging capabilities of the microscope.
- The small distance between the sample and mirror imposes a restriction on the extent to which the sample can be tilted, which can be an issue in the examination of three-dimensional structures.
- The *étendue* of the system imposes a strict compromise between the field of view of the microscope and the collection efficiency at the spectrometer [82].

In an effort to overcome these limitations, CL hyperspectral imaging systems have been developed, whereby light collection is achieved using an objective placed perpendicular to the electron beam as shown below in Fig 2.18. By allowing the optics to be placed further away from the sample, a far shorter working distance can be used, allowing the electron spot to remain small at low accelerating voltages [82].

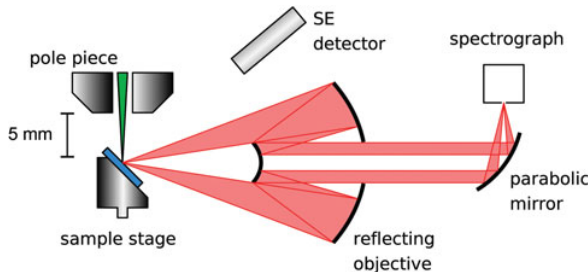


Fig. 2.18 Schematic layout of a CL hyperspectral imaging system [85].

The CL data in this thesis was collected on two separate systems, one employing the collection geometry described in Fig.2.17 and the other shown in Fig.2.18

Electron-Beam Induced Current

Electron beam induced current (EBIC) imaging is a technique complementary to scanning electron microscopy. The premise of the measurement is that minority carriers which arise from the incident electron beam of an SEM on a semiconductor junction can diffuse to the junction where they are separated by the built-in field and collected as current by an external circuit (the EBIC amplifier).

Due to the small interaction volumes achievable, EBIC can provide detailed spatial information on minority carrier dynamics. Regions of high signal indicate high collection efficiency and low recombination, for example: the depletion region of a p-n junction appears bright in EBIC imaging. As such EBIC imaging has proven extremely useful in characterising the recombination properties of individual defects across a wide range of semiconductors [86].

2.5 Hyperspectral Electroluminescence Mapping

Hyperspectral electroluminescence (EL) mapping can be used to characterise local variations in EL in optoelectronic devices. The EL mapping data in this thesis was acquired on a modified electron probe micro-analyser (EPMA). The EPMA consists of a CL system, and can also be used for CL spectroscopy. In order to perform EL mapping, the electron beam

is switched off and a pinhole inserted. A forward bias is then applied to the device being characterised and the stage is moved in order to build up a map of EL emission of the device which is collected by a CCD camera to build up a hyperspectral data set consisting of a full spectrum for each pixel.

2.6 Dual Beam FIB-SEM

In this work a dual beam focused ion beam/scanning electron microscope was used to perform sample preparation as well as 'slice and view' tomography experiments. As we have introduced the basic principles behind SEM we will focus on the FIB in this section.

The FIB is an extremely versatile combination of a scanning ion microscope (similar in principle to the SEM but utilising ions rather than electrons) and a precision machining tool. The ions utilised by the FIB are typically Ga^+ , though helium sources also exist. A liquid-metal ion source is used to produce the gallium ions which are focused into a beam and onto the surface of a sample in a similar manner to the SEM using electrostatic lenses and apertures. Due to the complementary nature of FIB and SEM instruments, dual beam FIB/SEM machines have been produced in which the techniques are used synergistically to overcome limitations on individual systems. Aside from a standard electron beam, the FIB-SEM contains an additional gallium ion beam at an angle of 52° to the axis of the electron beam as shown in Fig.2.19

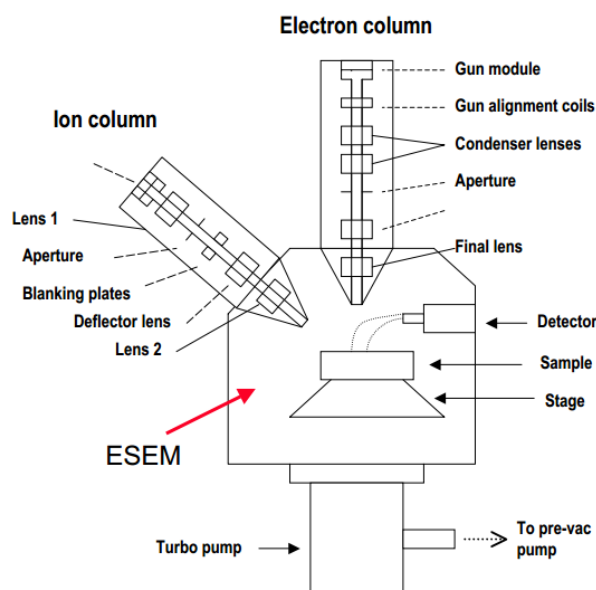


Fig. 2.19 Diagram of a dualbeam FIB-SEM

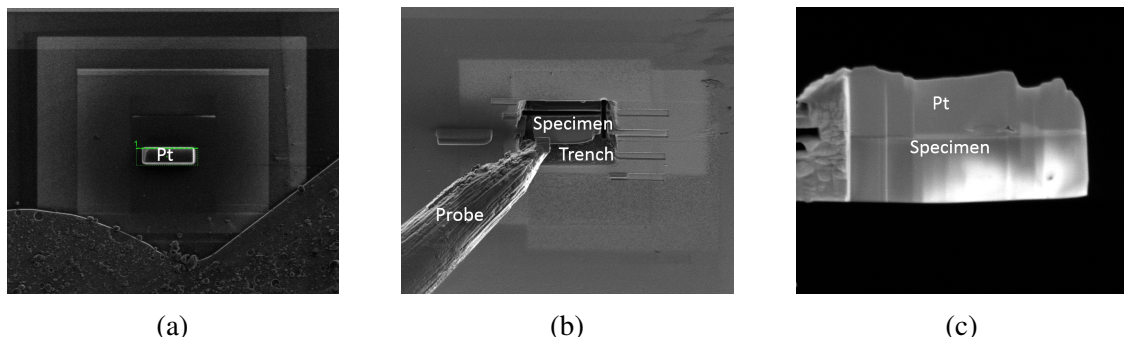


Fig. 2.20 FIB/SEM lamella lift-out and polishing process: a) Protective Pt layer deposition, b) trench milling and Lamella lift out c) final thinning.

Due to the large mass of the Ga^+ ions relative to electrons the interaction of the focused ion beam with a sample can cause sputtering of the material, thus allowing for the precise removal of material. Often the SEM is used to monitor the milling process of the FIB as electrons cause negligible damage to the sample relative to the ion beam. Beyond the removal of material, the ion beam can also often be used to deposit material. A gas injection system is typically used to achieve this: a gas containing a metal-organic compound is injected into the chamber where it interacts with the targeted ion-beam at the surface of the sample leading to the heavier metal atoms remaining at the sample surface whilst the organic material is evacuated by the chamber vacuum system. Typically, platinum or carbon can be deposited using this method, though the platinum often contains carbon and other impurities rendering it effectively semi-insulating.

2.6.1 Sample Preparation

Transmission electron microscopy requires electron transparent samples, typically of a thickness on the order of 100-150nm. As such the dual beam FIB/SEM allows for site-specific TEM specimen preparation. Unless otherwise stated, all the TEM samples prepared in this work were produced using the FIB/SEM.

The specimen preparation method is shown in Fig.2.20 is as follows:

- A region of interest on the sample surface is identified.
- A protective layer of metal is deposited using the GIS system, first with the electron beam then with the ion beam.
- Ion milling is used to form trenches on either side of the deposited protective layer
- A probe is then attached to the lamella by connecting the two with ion-beam deposited metal and used to lift the lamella out.
- The lamella is then transferred to a TEM grid, where it is thinned to a suitable thickness.

2.6.2 Tomography

FIB/SEM tomography, often referred to as 'slice and view', is a technique which has become relatively widespread in materials and life sciences due to the variety of detection modes available in commercial systems as well as the resolution and volume of material which can be analysed. Typical resolutions that can be achieved (voxel sizes) are in the range 5-10 nm. In FIB/SEM tomography, a small volume of the sample is selected for analysis. This volume is then typically coated with a layer of protective metal in order to prevent ion beam damage. Serial sectioning is then used to analyse the sample: alternating turns of milling and imaging allow for the sequential erosion of thin layers of material and subsequent imaging as shown in Fig.2.21. In this work we employ only the use of the SE detector for imaging.

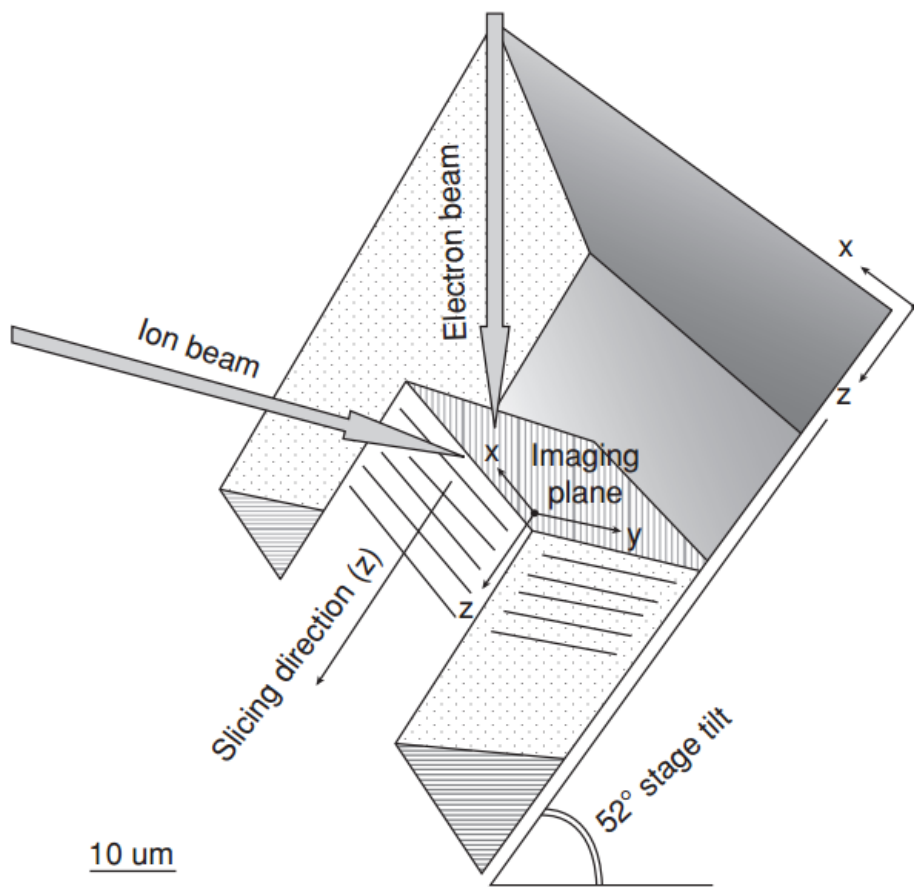


Fig. 2.21 Schematic of sample geometry for serial sectioning in a FIB/SEM instrument [87].

The purpose of serial sectioning is to produce a stack of images which can be transformed into a voxel-based volume data set. As such the thickness of the milled layers should match approximately with the resolution in the imaging plane.

Perhaps the most challenging task in FIB/SEM tomography lies in the extraction of information from the reconstructed 3-D image volume. This procedure, known as 'stack-processing', is very similar to reconstruction protocol used for electron tomography and can be described as follows:

- 3-D volume reconstruction by stack alignment.
- Image defect correction (noise reduction etc...)
- Segmentation and recognition of objects.
- Visualization of voxel-based volume data.
- Quantitative analysis of features.

Chapter 3

Inhomogeneous Electroluminescence in InGaN QW LEDs

3.1 Background

$\text{In}_x\text{Ga}_{1-x}\text{N}/\text{GaN}$ QW structures are key structures in present day light emitting diodes in the visible wavelengths. Despite the growth of III-nitride LEDs into a gigantic market with a projected overall worth of 64 billion EUR by 2020, III-nitride alloys suffer from a plethora of material issues arising from heteroepitaxial growth on foreign substrates with large lattice mismatches [6]. A notorious issue in III-nitride growth is the high density of threading dislocations which are the source of highly undesirable effects in diode structures such as non-radiative recombination [88] and leakage current [6].

Threading dislocations have been shown to result in inverted pyramidal defects at the surface of nitride epilayers, known as 'V defects'. The effect of these defects on LED performance is hotly debated in literature as they are expected by many to hinder LED performance due to their association with TDs. However, it has been shown that narrower QWs along the sidewalls of V-defects serve to screen carriers from the non-radiative centres at TDs [34].

In this study, a 'multi-microscopy' approach whereby several microscopy techniques are utilised on the same features is used to elucidate the origin of inhomogeneous EL in $\text{In}_x\text{Ga}_{1-x}\text{N}/\text{GaN}$ QW structures. The correlation of emissive and structural properties at the surface of the LED structures using several microscopy techniques has allowed for the detection of hexagonal defects at the centre of the inhomogeneities. Following this, structural and compositional information obtained using this combination of techniques is then used to simulate and reproduce the inhomogeneous EL, thus elucidating the mechanism whereby hexagonal defects can cause inhomogeneous EL in LEDs.

3.2 Sample Structure

For this study, two multiple QW InGaN LED structures of different QW nominal thicknesses (3.5 nm and 4.5 nm) were studied. Both samples were grown at the Cambridge Centre for Gallium Nitride, with LED processing carried out at the University of Bath. The structures were grown on low dislocation density ($5 \times 10^8 \text{ cm}^{-2}$) GaN template on sapphire, and consist of a $2 \mu\text{m}$ layer of unintentionally doped GaN followed by a $3 \mu\text{m}$ silicon doped GaN layer. The active layer consists of a 5 period InGaN/GaN MQW region, with unintentionally doped GaN barriers (7.6 nm). An AlGaN electron blocking layer (20 nm) and a magnesium-doped GaN cap (117 nm) were grown following the active region. This is shown schematically in Fig. 3.1:



Fig. 3.1 LED structure schematic.

The wafers were processed into $1 \times 1 \text{ mm}^2$ side contacted LEDs with thin oxidized Ni/Au current spreading *p*-layer Ohmic contact. Ti/Al Ohmic contact stripes were deposited on the *n*-layer and the Ni/Au current spreading layer in an interdigitated geometry.

QW thickness for both samples was determined from X-ray diffraction (XRD) using the method described by Vickers *et al.* [9]. The QWs were grown using the '2T' method, whereby the growth temperature is ramped up immediately following the InGaN growth

under ammonia but without metalorganic fluxes. The barrier growth begins towards the end of the temperature ramp, this typically leads to loss of indium during the temperature ramp which can cause gross well-width fluctuations [89] but a higher barrier growth temperature is preferable[90]. '2T' growth is shown schematically in Fig.3.2.

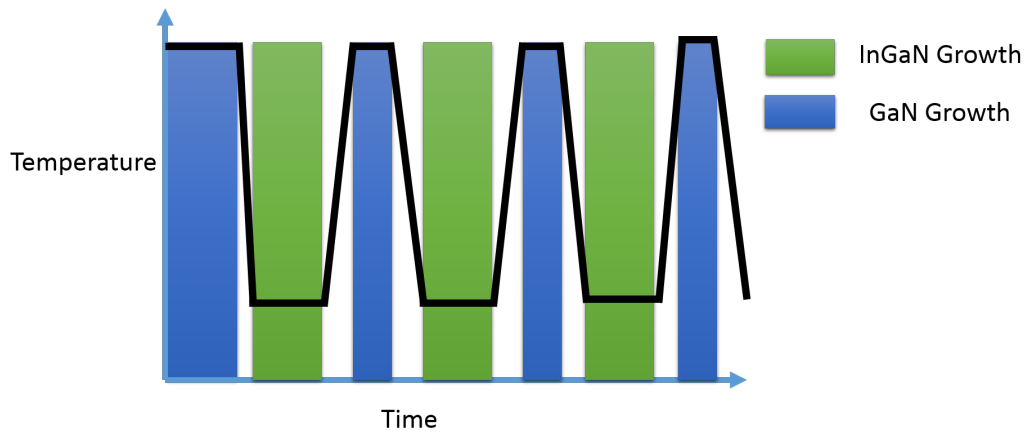


Fig. 3.2 '2T' growth of InGaN/GaN QWs. GaN QB growth is halted during the temperature ramp. The black trace indicates growth temperature over time.

3.3 Experimental

Initial evaluation of the inhomogeneous EL was performed in a Signatone S-1160 probe station under forward bias, as shown in Fig.3.3.

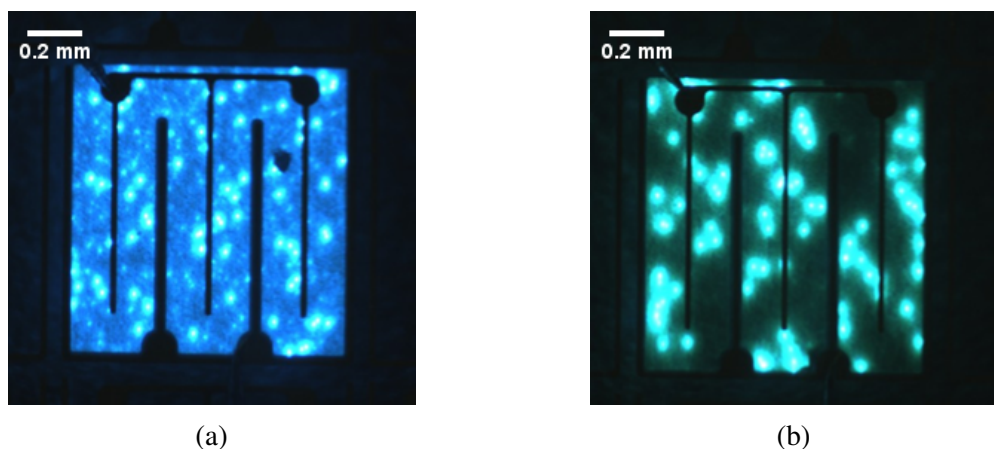


Fig. 3.3 a) C5610A b) C5608A EL under a forward bias of 3V. The bright inhomogeneities are visible in the emission of the LEDs.

Following this, hyperspectral EL mapping with CL and EBIC were performed using a modified Cameca SX100 electron probe micro-analyser with a custom built cathodoluminescence set-up. Hyperspectral EL measurements were performed under forward bias, enabling the acquisition spatially resolved EL maps of the inhomogeneities. Following the detection of hexagonal defects at the centre of inhomogeneities using SEM-CL, the defects were analyzed using AFM and C-AFM. Finally, FIB/SEM lamella preparation techniques were used to perform HAADF-STEM and STEM-EDX on the defects, allowing for access nanoscale compositional and structural information required to reproduce the EL in simulations.

3.3.1 Hyperspectral EL Imaging

Hyperspectral EL imaging was performed at Strathclyde University with the assistance of Dr Michael Wallace. In order to study the device under forward current, the LED wafers were mounted on TO-5 headers and bonded with 5 μm Al wire. A Keithley Instrument 2401 source meter was used to apply varying forward currents to the devices and thus allow for the collection of EL.

Full EL spectra were collected with a spatial resolution of approximately 3 μm and analysed using custom software developed by Dr. Paul Edwards, allowing for 2-D maps of EL peak intensity, position and FWHM. At each pixel in the map, a full EL spectrum was collected by an Andor CCD camera. A full set of data extracted from the hyperspectral EL mapping is shown in Fig.3.4

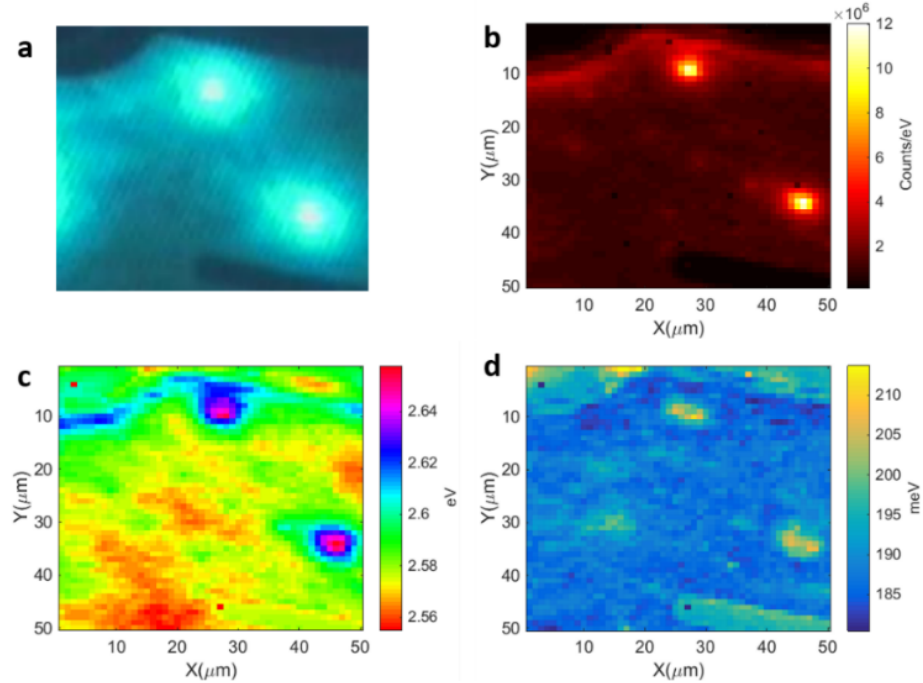


Fig. 3.4 a) Probe station image b) EL peak intensity, c) EL peak energy and d) EL FWHM extracted by fitting the hyperspectral EL data under a forward current of 10 mA

It is interesting to note that from this representative data set, the inhomogeneities observed are brighter by a factor of ~ 6 , blue-shifted in terms of peak energy by ~ 0.08 eV and have a larger FWHM. Although these values were observed to shift based on injection current, the overall trend observed in all data sets for both LED devices is represented by Fig.3.4.

Current Dependent EL Measurements

Current dependent hyperspectral EL maps of the same area were performed, in order to examine the behaviour of the inhomogeneities with increasing current relative to the 'uniform' background. The peak intensities and peak energies for injection currents for device C5610A ranging from 1-500 mA are shown in Figures 3.5 and 3.6 respectively.

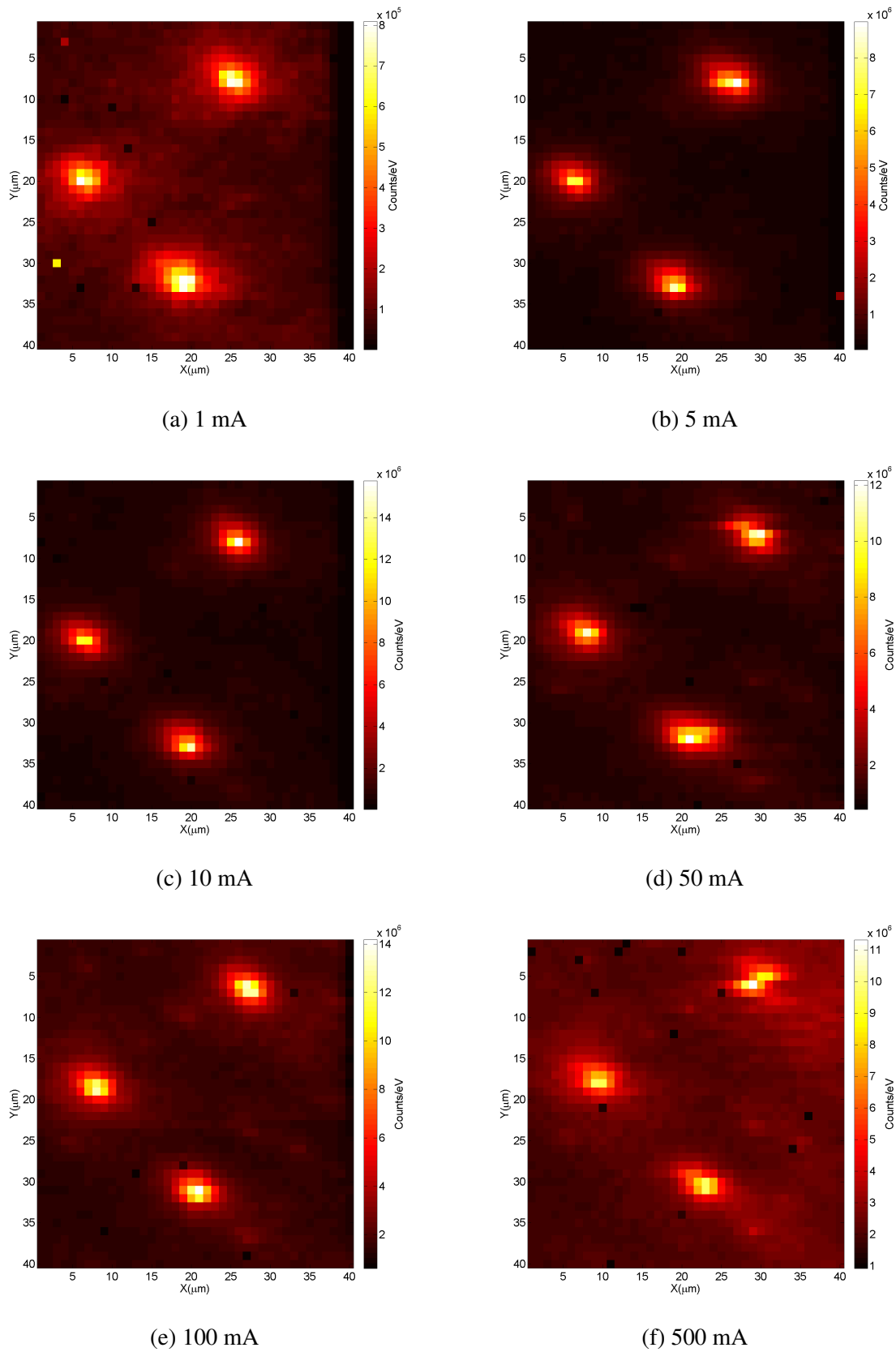


Fig. 3.5 Peak intensity for varying injection current for C5610.

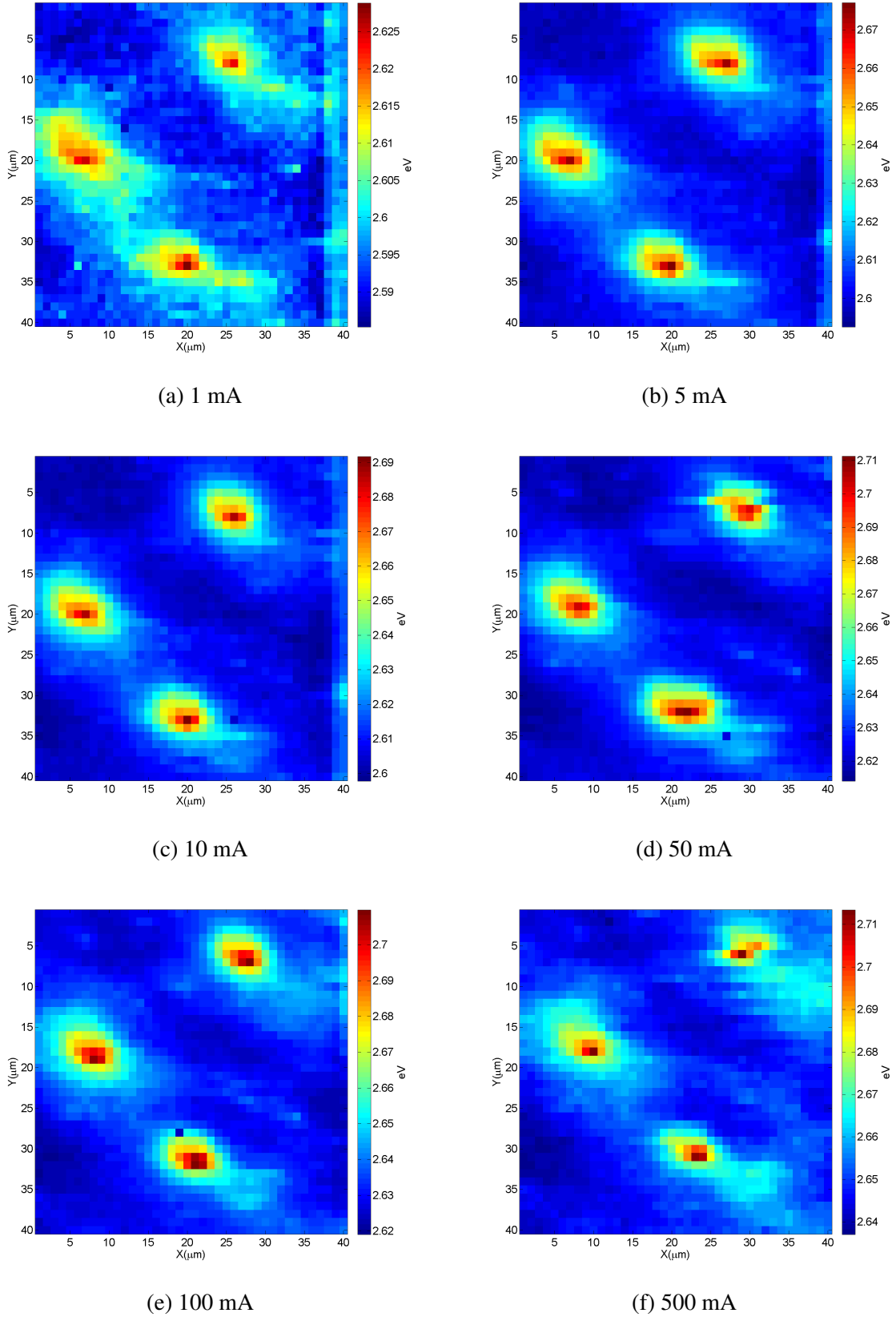


Fig. 3.6 Peak energy for varying injection current for C5610.

The spatially resolved EL data shown in Figures 3.5 and 3.6 allow for the comparison between areas containing the inhomogeneities and the 'background' EL by thresholding the data set. This is demonstrated in Fig. 3.7 which shows the behaviour of both the inhomogeneities (labelled 'spots') and the averaged background peak intensity with increasing injection current.

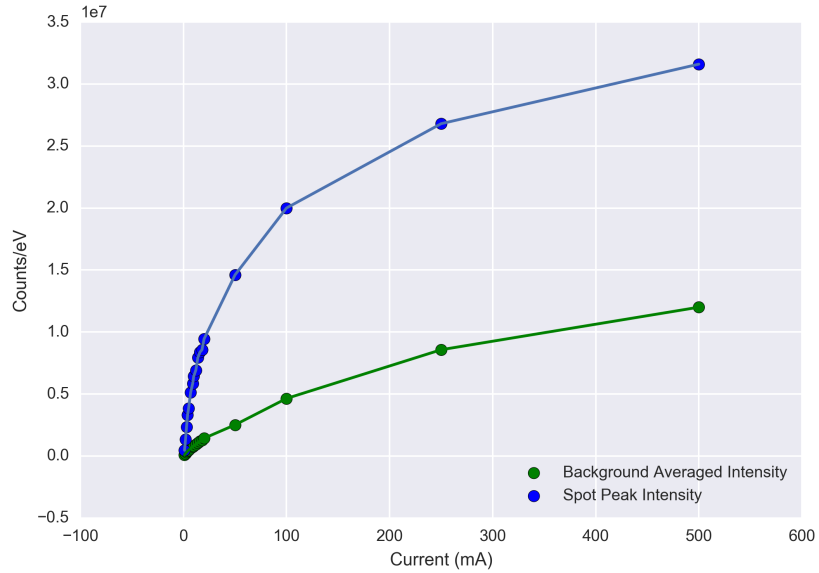


Fig. 3.7 Spot and background average peak intensity against injection current

It is interesting to note that Fig.3.7 shows the inhomogeneities experience a far sharper initial increase in peak intensity relative to the background based on the hyperspectral EL data fitting in the current range 0-50 mA, perhaps indicating enhanced current injection in the areas exhibiting the inhomogeneities.

Fig. 3.8 shows the same current dependent comparison for background and inhomogeneity peak energy. Here we see the same trend, in that the inhomogeneity exhibits a larger current-induced blueshift in the 0-50 mA range relative to the background. The origin of the current-dependent blueshift in InGaN QW structures is attributed to the screening of the QCSE by the additional carriers injected into the wells [22], and as such indicates the inhomogeneities are regions experiencing higher current injection relative to the background.

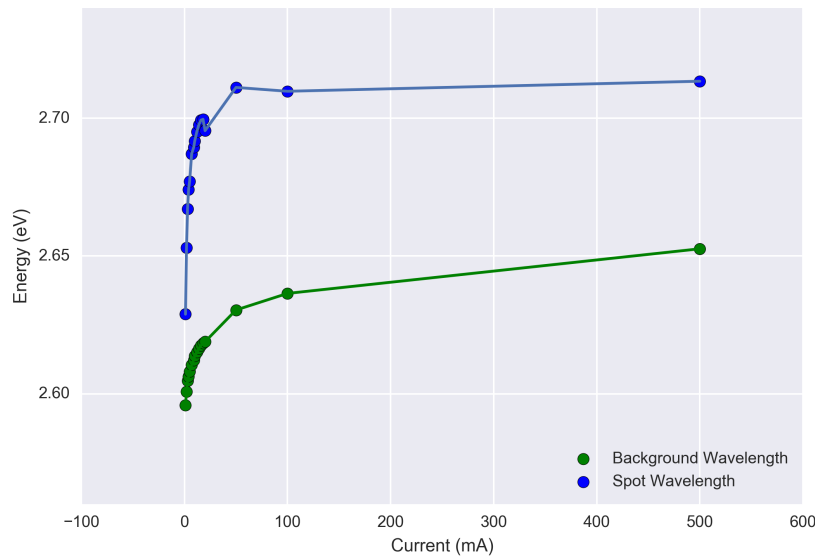


Fig. 3.8 Spot and background average peak energy against injection current

Device C5608A exhibited a similar current dependent relationship between the inhomogeneities and the background, as shown in Fig. 3.9 and 3.10. As evidenced by Fig. 3.3, Fig. 3.9 demonstrates a larger difference in EL intensity between the background and the inhomogeneities for C5608A relative to C5610A.

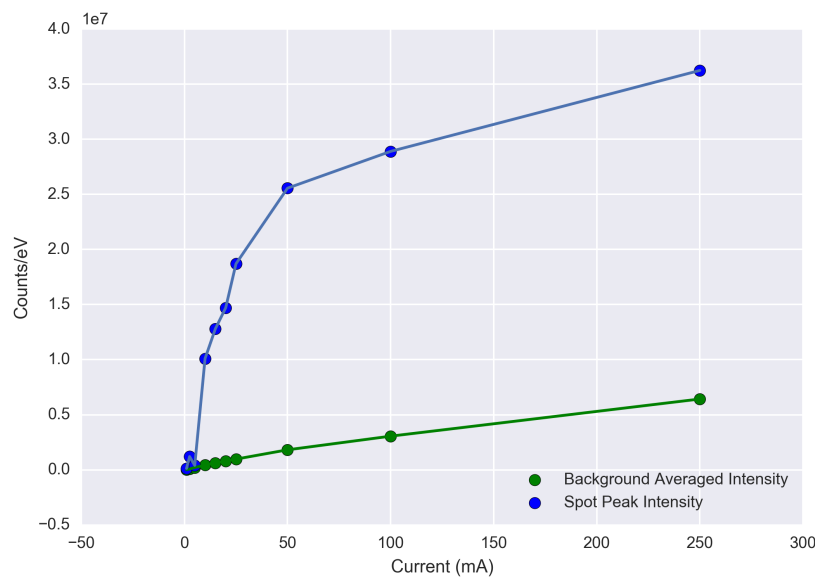


Fig. 3.9 Spot and background average peak intensity against injection current

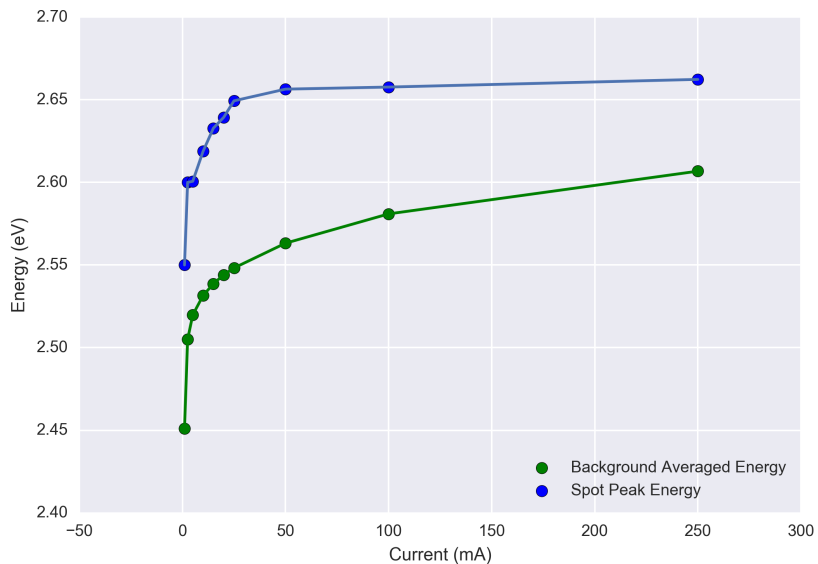


Fig. 3.10 Spot and background average peak intensity against injection current

3.3.2 Cathodoluminescence and Electron Beam Induced Current

Having noted the behaviour of the inhomogeneities inferred from the hyperpectral EL data, CL and EBIC data were taken over areas containing the inhomogeneities in order to examine their properties in more detail as CL and EBIC are electron beam based techniques and as such allow for a far higher resolution than EL mapping.

In order to achieve simultaneous CL and EBIC measurements, a Keithley Instrument 2401 source/measure unit was utilised in order to main the LED devices at a fixed bias of 0V thus allowing for the measurement of the short circuit current. During the CL image scanning, the Andor CCD camera was set-up to trigger the measure unit to record the current at each point in the CL spectral acquisition. The CL acquisition was performed with an electron beam at 10 kV and 1 nA. Unfortunately the secondary electron detector was inoperable during the acquisition of this data, as such there is no accompanying SEM micrograph for the CL and EBIC data. The CL and EBIC data for devices C5610A and C5608A are shown in figures 3.12 and 3.13 respectively.



Fig. 3.11 EL images of the regions examined using CL and EBIC mapping for a) C5610A and b) C5608A.

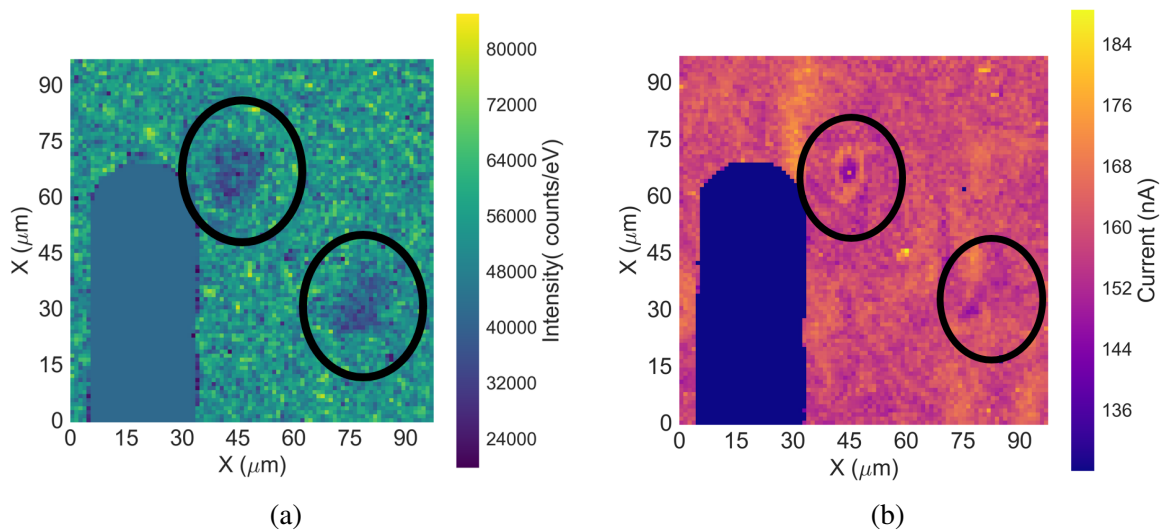


Fig. 3.12 a) CL and b) EBIC maps acquired simultaneously of the area shown in Fig.3.11 a.

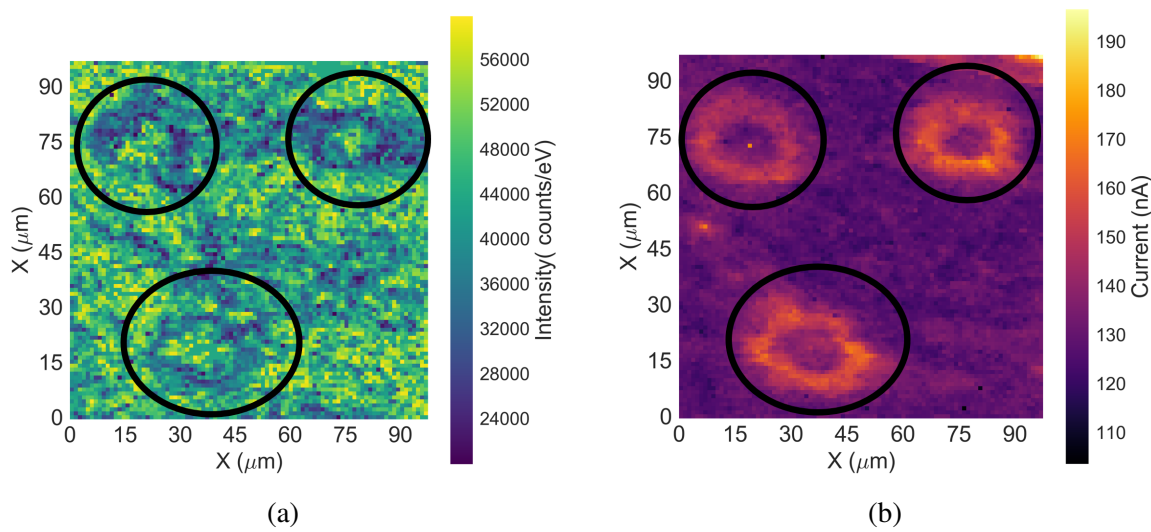


Fig. 3.13 a) CL and b) EBIC maps acquired simultaneously of the area shown in Fig.3.11b.

Fig. 3.12a. shows the inhomogeneities exhibit a lower CL intensity relative to the background, in contrast to the EL. Interestingly, the EBIC signal, shown in Fig.3.12 for both inhomogeneities examined seem rather different. The feature closest to the contact region can be seen as a region of high EBIC surrounding a region of lower extracted current. However the feature furthest from the electrical contact shows far less prominent EBIC signal. The features examined are far more prominent in the case of device C5608A. Fig.3.13.a. shows the detection of 'rings' emitting at a lower at a lower intensity in the CL at the location of the features. These rings correspond to rings of higher EBIC current as observed in Fig.3.13.b.

Scanning Electron Microscopy with Cathodoluminescence

Following the CL and EBIC scans shown in figures 3.12 and 3.13 performed at Strathclyde University, more detailed SEM-CL experiments were performed at the University of Cambridge using a Phillips XL30s field emission SEM at 5 kV equipped with a Gatan MonoCL4 system to record the CL signal. This set-up provides the additional benefit of panchromatic CL imaging, which allows for the detection of the features without the need for extremely detailed EL correlation.

Fig. 3.14 shows the morphology of the features in the panchromatic CL and the associated SEM micrograph. The inhomogeneity appears as a region of lower CL intensity, though it is important to note the signal in panchromatic CL mode is the sum of the complete spectrum of photons collected. Nonetheless, this can be considered in relatively good agreement with the CL intensity recorded in Fig.3.12.a. Fig.3.14 reveals the presence of a hexagonal

defect (outlined in red) which can be spatially correlated with the centre of the feature in the panchromatic CL image in Fig.3.12.b.

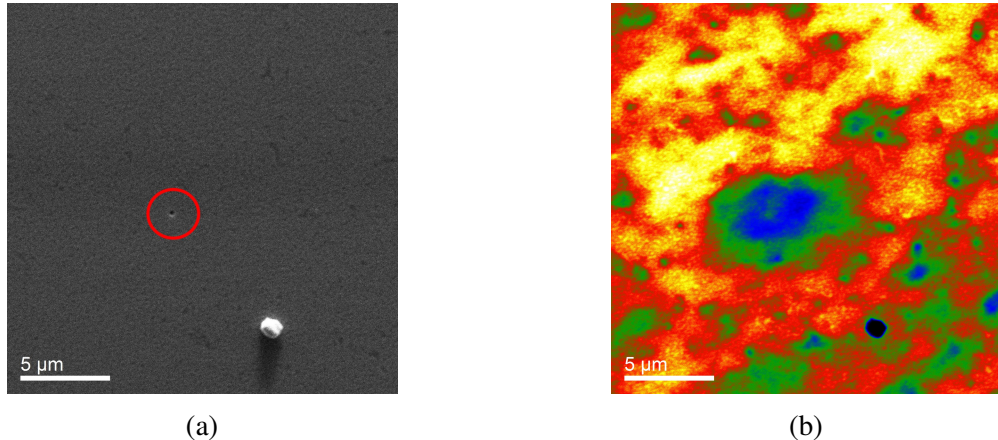


Fig. 3.14 a) SEM micrograph and b) pan-CL image of an inhomogeneity in C5610A. The pan-CL image utilises a temperature scale (blue = low, red = high).

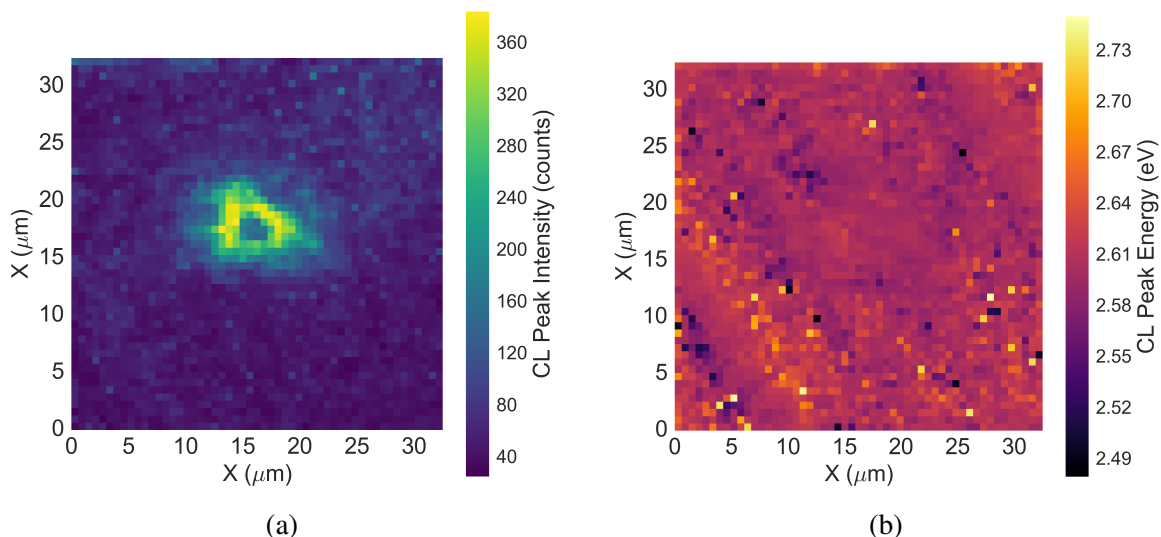


Fig. 3.15 a)CL peak intensity and b) CL peak energy for the feature shown in Fig.3.14

Following the detection of a hexagonal defect at the centre of the feature, a $32 \times 32 \mu\text{m}^2$ hyperspectral CL scan was performed in the region of the defect. Figures 3.15.a. and 3.15.b. show the CL peak intensity and peak energy respectively. The defect appears to show little CL intensity, which is expected to due the association of hexagonal defects with threading dislocations [6]. However, the region surrounding the defect appears as a 'ring' of higher CL intensity. It is difficult to resolve differences in the peak CL energy in Fig.3.15.b. due to the low CL intensity disrupting the accuracy of the fitting process.

The same experiment was performed for a feature in device C5608A, which revealed a similar morphology for the features in panchromatic CL imaging shown in Fig.3.14.b. in that the region surrounding the hexagonal defect exhibited a lower overall CL intensity.

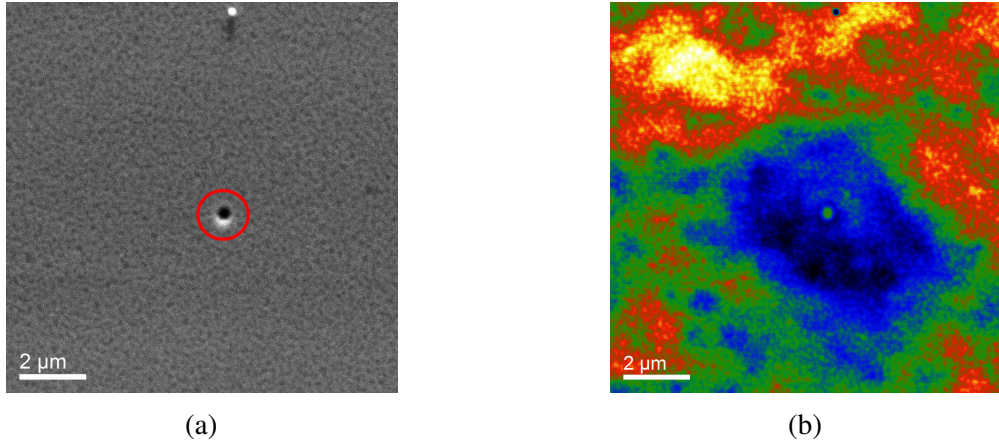


Fig. 3.16 a) SEM micrograph and b) pan-CL image of an inhomogeneity in C5608A. The pan-CL image utilises a temperature scale (blue = low, red = high).

A hyperspectral CL map of $2 \times 2 \mu\text{m}^2$ was taken to examine the emissive properties of the defect in more detail. Fig.3.17.a. shows that as expected, the region close to the hexagonal defect exhibits low CL intensity. Interestingly, the defect also shows extremely low-energy emission relative to the background, most likely due to defect-related yellow band emission [91].

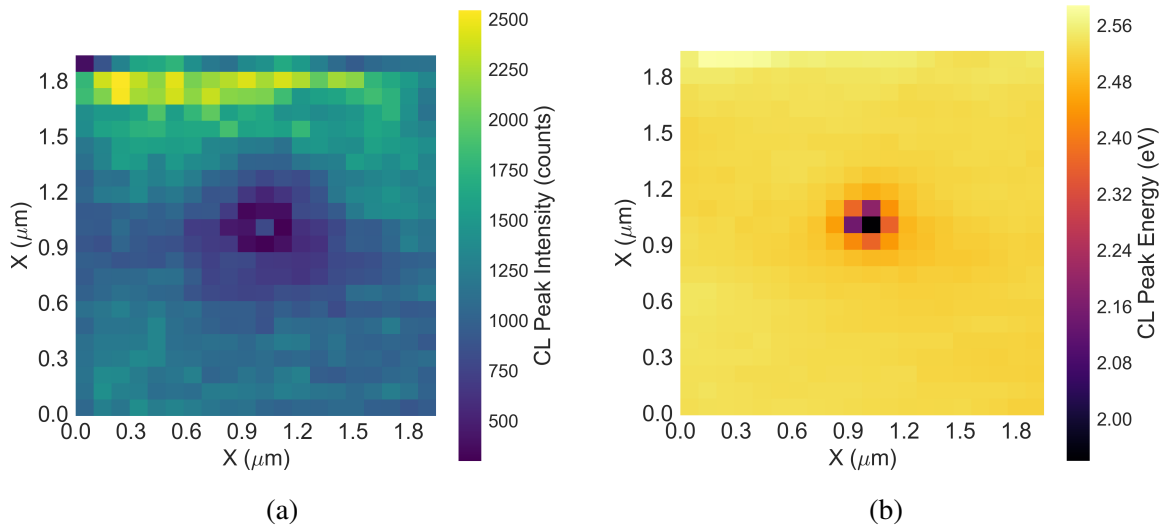


Fig. 3.17 a)CL peak intensity and b) CL peak energy for the feature shown in Fig.3.16

3.3.3 Hexagonal Defect Structure

The structure of the hexagonal defects found at the centre of the inhomogeneities was examined following their detection using SEM-CL.

Scanning Electron Microscopy

In order to achieve a higher resolution in examining the defects via SEM, an FEI Helios Nanolab 650 SEM/FIB with a schottky FEG at 5 kV and through lens detector (TLD) was used to perform high resolution SEM imaging. This is shown in Fig. 3.18.

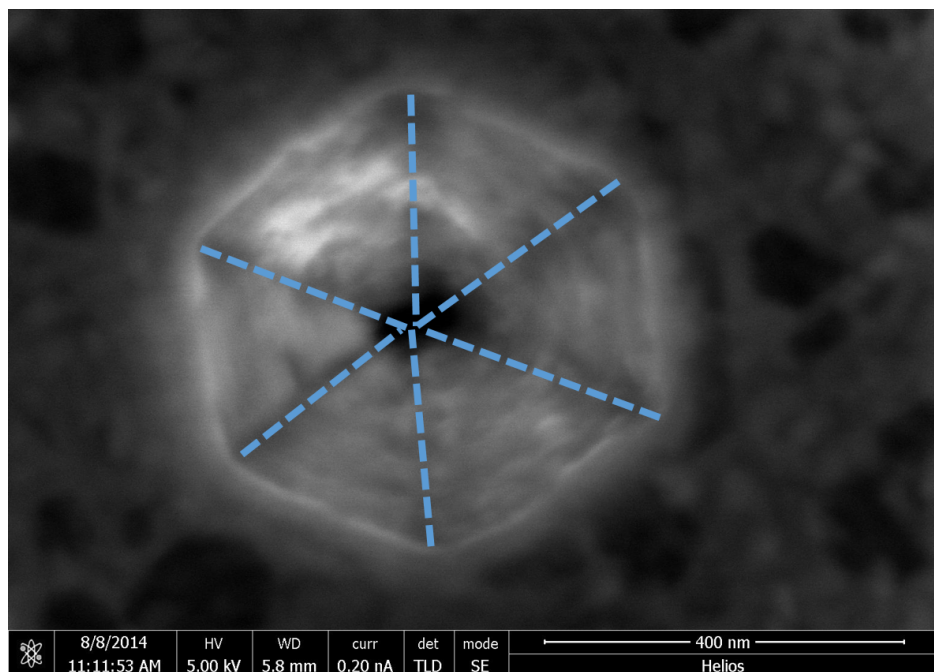


Fig. 3.18 High-resolution SEM image of a hexagonal defect located at the centre of an inhomogeneity in the EL. The vertices of the facets are delineated by dashed lines.

Most hexagonal defects located at the centre of the inhomogeneities fell within the 200-600 nm range, with some exceedingly large defects reaching up to 1 μm in size. This is rather uncommon for hexagonal defects in III-nitrides, as the lateral size of hexagonal defects is typically sub-100 nm [92, 36].

Atomic Force Microscopy

The topography of the hexagonal defect was studied by AFM performed on a Veeco Dimension 3100 with RTESP tips with a nominal radius of 8 nm in intermittent contact mode. The defect shown in the SEM micrograph in Fig.3.18 is shown below in the AFM image.

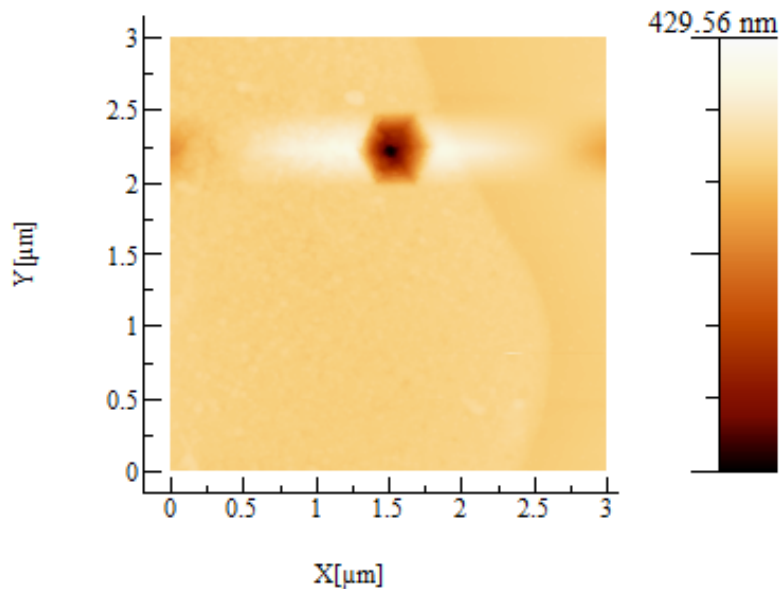


Fig. 3.19 AFM image of the hexagonal defect.

By taking a topography profile across the hexagonal defect, we can resolve the depth of the defect as well as the slope of the facets.

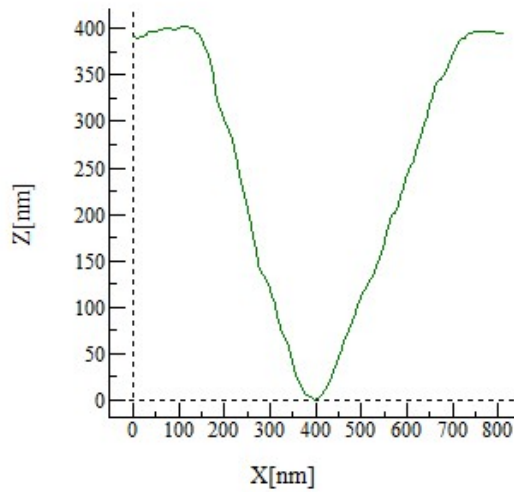


Fig. 3.20 Profile taken across the defect shown in Fig.3.19

Conductive-AFM

TEM Lamella preparation

Preparation of TEM lamellae for the analysis of the defects requires some additional steps due to site-specific nature of the experiment. Standard FIB/SEM sample preparation methods simply require a 2 μm thick wedge of the sample to be extracted and thinned down to a thickness of 100-200 nm for TEM experiments. However, analysis of the defect and any associated dislocations which may be present at the apex of the inverted pyramidal shape [93, 94] requires thinning to be performed in an extremely controlled manner. As such a method devised by Thomas O'Hanlon at the Cambridge Centre for Gallium Nitride was utilised to perform high-precision site specific TEM sample preparation shown in Fig.3.21. A 'marker layer' consisting of a cross intersecting the apex of the defect is deposited using the electron beam, thus allowing for little damage to the unprotected sample and a higher deposition resolution than the ion beam. Following this a protective layer is then deposited using the ion beam, and a standard dual-beam lift-out method is used to extract the wedge of sample containing the defect.

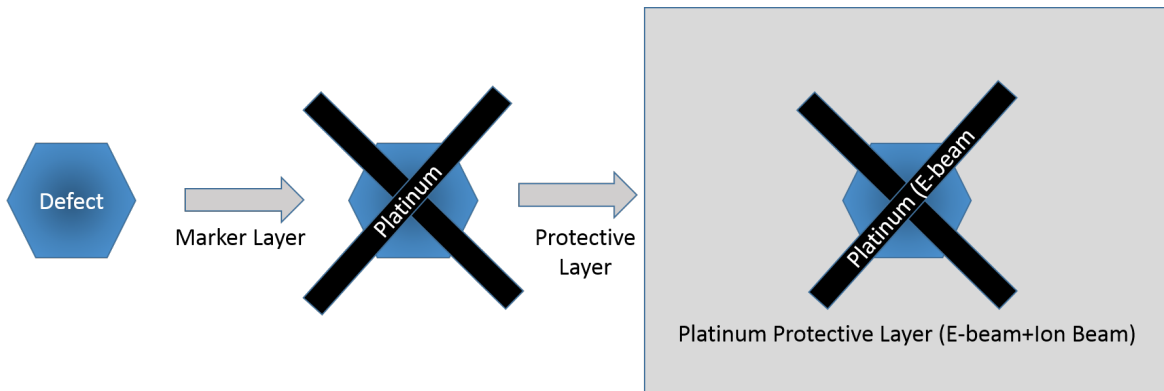


Fig. 3.21 Marker layer deposition for high precision TEM sample preparation.

The purpose of the marker layer is to serve as a guide during sample thinning. The electron beam deposited platinum provides contrast against both the sample and the ion-beam platinum in the SEM image. As the sample is imaged in cross-section during the thinning process, the distance between the marker layer 'ends' is an indicator of the proximity to the defect apex. As the defect apex is reached during the thinning process, the two marker stripes should merge into one at the intersection of the cross, as shown in Fig.3.22.

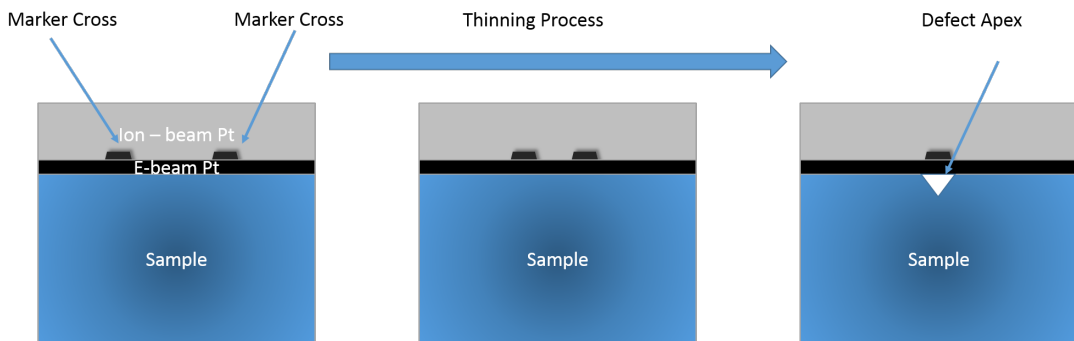


Fig. 3.22 Marker layer deposition for high precision TEM sample preparation.

A successfully thinned sample is shown in Fig.3.23.

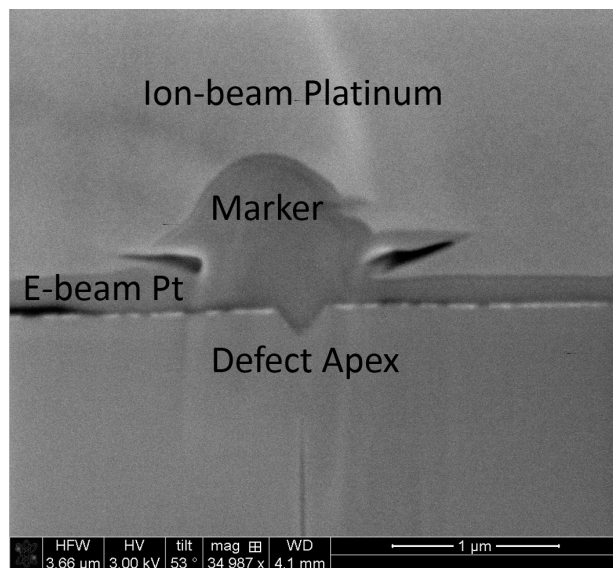


Fig. 3.23 SEM image of a prepared TEM lamella showing the marker position and defect apex.

Transmission Electron Microscopy

The site-specific TEM lamella prepared using the dual-beam methods, shown in Fig.3.23 was studied by HAADF-STEM performed on an FEI Osiris microscope with an extreme-FEG (X-FEG) at 200 kV. HAADF-STEM imaging of the defect reveals it originates below/at the MQW stack, a possible explanation for the large size of the hexagonal defects relative to those reported in literature [34, 36, 92].

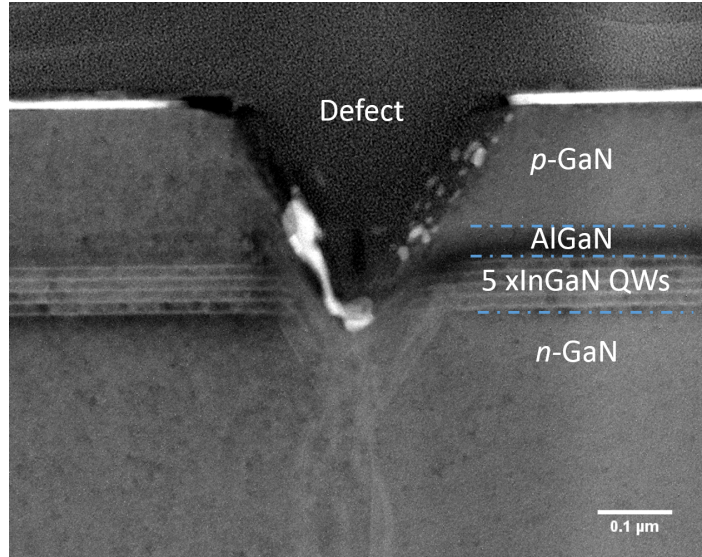


Fig. 3.24 HAADF-STEM image of a prepared TEM lamella showing defect interrupting the QW stack.

The composition of the MQW stack adjacent to the region occupied by the defect was studied using EDX-STEM, where the characteristic X-rays emitted by the sample were recorded by four silicon drift detectors which form a solid angle greater than 0.9 sr. Cliff-Lorimer analysis of the aluminium, gallium and indium was performed using HyperSpy in order to quantify the ternary alloy compositions as shown in Fig.3.25

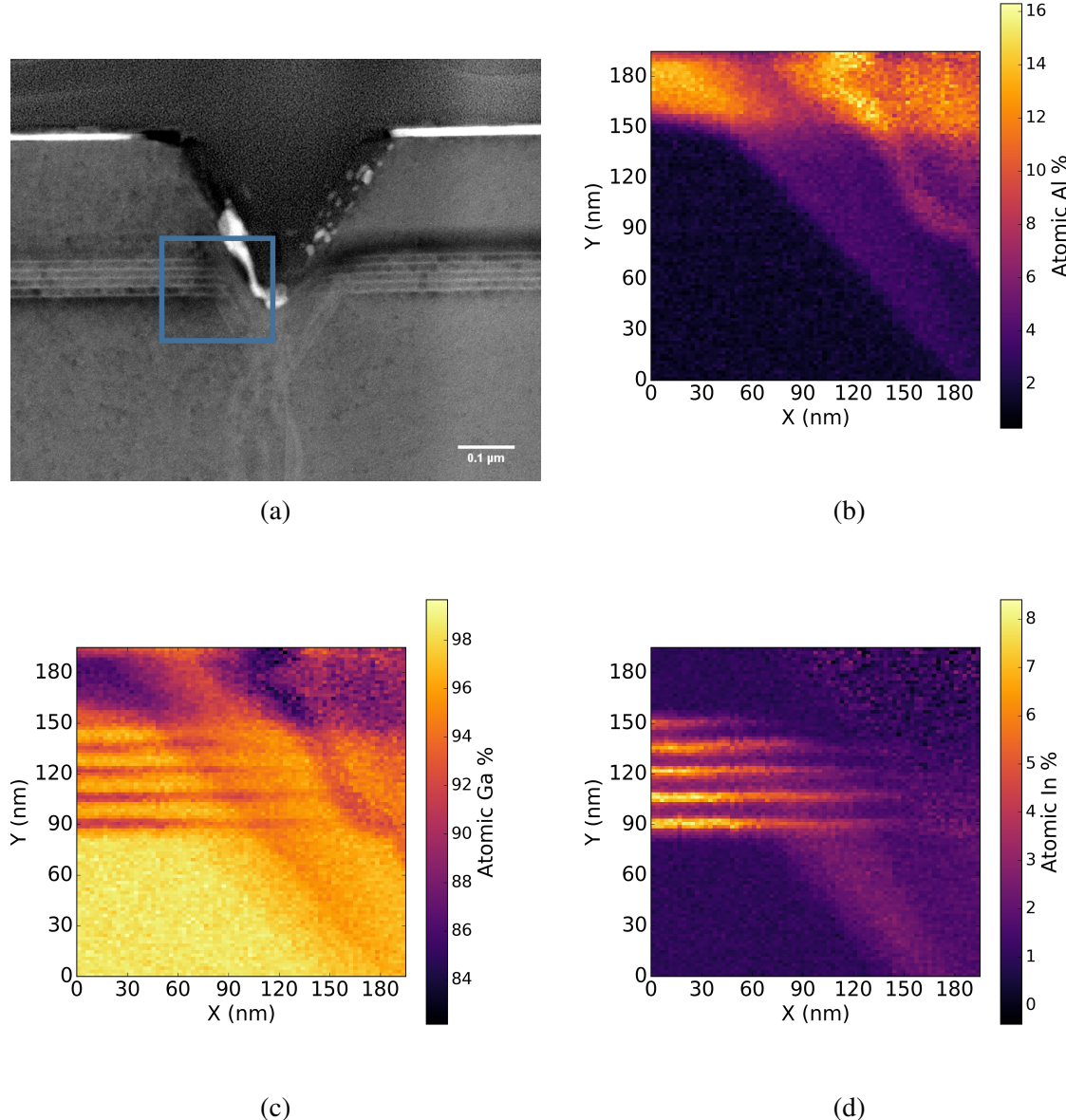


Fig. 3.25 Quantification of the ternary alloy compositions: a) HAADF-STEM image showing the region examined by EDX (blue box) b) aluminium atomic percentage, c) gallium atomic percentage and d) indium atomic percentage.

The EDS analysis shows the disruption of the QW stack by the defect, as evidenced by the apparent termination of the QW In signal in Fig.3.25.d. Additionally, the Al signal can be seen to overlap with the QW In signal, suggesting the presence of aluminium in the region disrupted by the defect. Furthermore, there is an observable indium signal originating from below the QWs. Although both the aluminium and indium atomic percentages observed in the region disrupted by the defect appear lower than expected (approximately 6-7 % and 4 % respectively) it is also important to consider the effect of the sample geometry in the collection of the EDX signal: due to the inverted pyramidal morphology of the defect the collected signal is expected to be reduced, and thus the atomic percentages obtained via quantification are expected to be under-estimates.

3.3.4 LED Simulations

In order to investigate the manner in which changes induced by the defect could affect the EL of the LED simulations were performed by Bertrand Rouet-Leduc using the APSYS simulation package, with parameters taken from J.Piprek [95]. The carrier transport equations are self-consistently solved and coupled with the Schrodinger equation to compute the confined states in the QWs.

Deep Inclusion

Fig.3.26 shows the simulated LED structure with a hexagonal defect incorporated. In this case we assume the QW stack simply continues along the edge of the hexagonal defect as described in [34], as the EDX quantification reveals a detected atomic percentage of indium of approximately 4 % below the QW stack. We assume a similar geometry for the AlGaN EBL, which is expected to follow the angled facet of the defect. Thus, this set of simulations deals with what we term a 'deep' AlGaN inclusion, which is expected to penetrate below the QW stack.

In this set of simulations, we have set the *p*-GaN doping concentration to $3 \times 10^{19} \text{ cm}^{-3}$, the *p*-AlGaN EBL doping to $4 \times 10^{19} \text{ cm}^{-3}$ except on the semi-polar facets of the defect where it is set to $1 \times 10^{19} \text{ cm}^{-3}$.

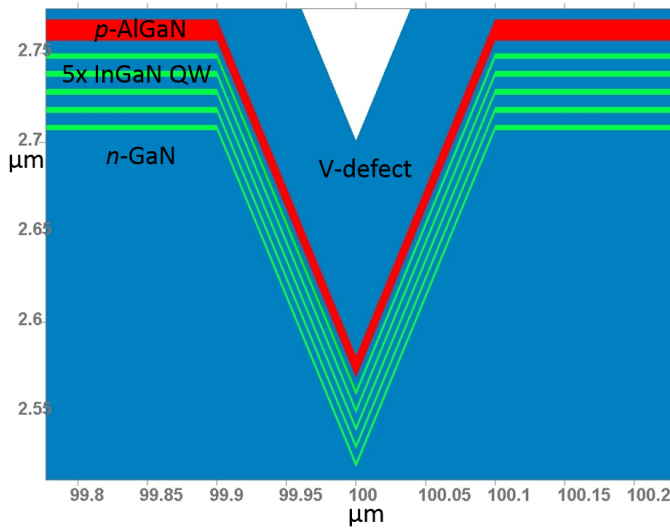


Fig. 3.26 Simulated LED structure.

The simulation results are shown in Fig.3.27. Fig.3.27.a. shows overall radiative recombination events in units of $10^{28} \text{ cm}^{-3} \text{ s}^{-1}$. The region closest to the defect at the lowest QW shows an increased radiative recombination rate, indicating the presence of the defect can indeed cause enhanced radiative recombination under electrical injection in regions surrounding the defect. Fig.3.27.b. shows two profiles taken from Fig.3.27.a. intersecting the five QWs and indicates that the rate of radiative recombination is almost doubled in the lowest QW close to the defect when compared with a profile taken further away.

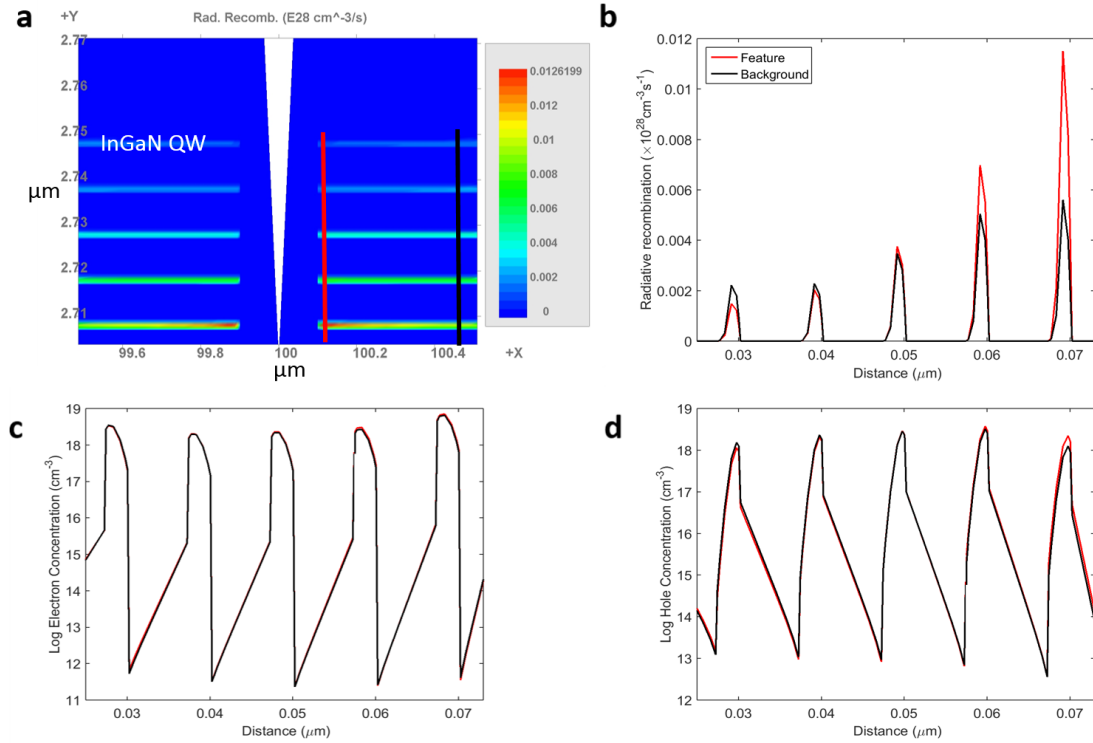


Fig. 3.27 APSYS simulation results: a) Radiative recombination events b) radiative recombination profiles, c) electron concentration profiles and d) hole concentration profiles. Red and black traces in b), c) and d) correspond to the red and black profiles in a).

Shallow Inclusion

In this simulation we have simulated a structure similar to the EDX maps shown in Fig.3.25. We have assumed that the AlGaN EBL may penetrate only slightly in into the QW stack due to the defect, but otherwise the rest of the disrupted region is filled with undoped GaN. The AlGaN EBL doping is set to $5 \times 10^{18} \text{ cm}^{-3}$ with an Al content of 10%.

3.4 Conclusion

3.5 Future Work

References

- [1] C. J. Humphreys, “USE Solid-State Lighting,” *MRS Bulletin*, vol. 33, no. April, pp. 459–471, 2008.
- [2] S. Nakamura, T. Mukai, and M. Senoh, “High-Power GaN P-N Junction Blue-Light-Emitting Diodes,” *Japanese Journal of Applied Physics*, vol. 30, no. 12A, pp. 1998–2001, 1991.
- [3] S. Najda, P. Perlin, L. Marona, M. Leszczy, R. Czernecki, S. Watson, A. E. Kelly, A. Malcolm, P. Blanchard, and H. White, “Novel laser diode technology for free-space communications,” *SPIE*, pp. 10–12, 2015.
- [4] H. Berlien, H. Breuer, G. Müller, N. Krasner, T. Okunata, and D. Sliney, *Applied Laser Medicine*. Springer Berlin Heidelberg, 2012.
- [5] S. Kako, C. Santori, K. Hoshino, S. Götzinger, Y. Yamamoto, and Y. Arakawa, “A gallium nitride single-photon source operating at 200 K.,” *Nature materials*, vol. 5, pp. 887–92, nov 2006.
- [6] S. E. Bennett, “Dislocations and their reduction in GaN,” *Materials Science and Technology*, vol. 26, no. 9, pp. 1017–1028, 2010.
- [7] E. T. Yu, X. Z. Dang, P. M. Asbeck, S. S. Lau, and G. J. Sullivan, “Spontaneous and piezoelectric polarization effects in III–V nitride heterostructures,” *Journal of Vacuum Science & Technology B: Microelectronics and Nanometer Structures*, vol. 17, p. 1742, 1999.
- [8] I. Vurgaftman and J. R. Meyer, “Band parameters for nitrogen-containing semiconductors,” *Journal of Applied Physics*, vol. 94, no. 6, pp. 3675–3696, 2003.
- [9] M. E. Vickers, M. J. Kappers, T. M. Smeeton, E. J. Thrush, J. S. Barnard, and C. J. Humphreys, “Determination of the indium content and layer thicknesses in InGaN/GaN quantum wells by x-ray scattering,” *Journal of Applied Physics*, vol. 94, no. 3, pp. 1565–1574, 2003.
- [10] F. Scholz, “Semipolar GaN grown on foreign substrates: a review,” *Semiconductor Science and Technology*, vol. 27, p. 024002, feb 2012.
- [11] J. Wu, W. Walukiewicz, K. M. Yu, J. W. Ager, E. E. Haller, H. Lu, and W. J. Schaff, “Small band gap bowing in In_{1-x}Ga_xN alloys,” *Applied Physics Letters*, vol. 80, no. 25, pp. 4741–4743, 2002.

- [12] M. D. McCluskey, C. G. Van de Walle, L. T. Romano, B. S. Krusor, and N. M. Johnson, “Effect of composition on the band gap of strained $In_xGa_{1-x}N$ alloys,” *Journal of Applied Physics*, vol. 93, no. 7, pp. 4340–4342, 2003.
- [13] P. G. Moses and C. G. Van De Walle, “Band bowing and band alignment in InGaN alloys,” *Applied Physics Letters*, vol. 96, no. 2, pp. 2–5, 2010.
- [14] T. J. Puchtler, A. Woolf, T. Zhu, D. Gachet, E. L. Hu, and R. a. Oliver, “Effect of Threading Dislocations on the Quality Factor of InGaN/GaN Microdisk Cavities,” *ACS Photonics*, vol. 2, pp. 137–143, 2015.
- [15] C. X. Ren, “Polarisation fields in III-nitrides: effects and control,” *Materials Science and Technology*, vol. 00, no. 0, p. 1743284715Y.000, 2015.
- [16] O. Ambacher and J. Majewski, “Pyroelectric properties of Al (In) GaN/GaN hetero-and quantum well structures,” *Journal of physics: ..., vol. 3399*, 2002.
- [17] M. Sumiya and S. Fuke, “Review of polarity determination and control of GaN,” *MRS Internet Journal of Nitride Semiconductor Research*, vol. 9, no. 1, pp. 1–32, 2004.
- [18] C. Wood and D. Jena, *Polarization Effects in Semiconductors: From Ab Initio Theory to Device Applications*. Springer, 2007.
- [19] J. E. R. Miguel, C. J. Gladys, and O. L. César, “Computational calculation of the electronic and magnetic properties of 1×1 -MN / GaN (M = V , Cr and Mn) multilayers,” *International Journal of Physical Sciences*, vol. 9, no. 24, pp. 538–544, 2014.
- [20] V. Fiorentini, F. Bernardini, F. D. Sala, A. D. Carlo, P. Lugli, and T. Vergata, “Effects of macroscopic polarization in III-V nitride multiple quantum wells,” *Physical Review B*, vol. 60, no. 12, pp. 8849–8858, 1999.
- [21] S. F. Chichibu, A. Uedono, T. Onuma, B. a. Haskell, A. Chakraborty, T. Koyama, P. T. Fini, S. Keller, S. P. Denbaars, J. S. Speck, U. K. Mishra, S. Nakamura, S. Yamaguchi, S. Kamiyama, H. Amano, I. Akasaki, J. Han, and T. Sota, “Origin of defect-insensitive emission probability in In-containing $(Al,In,Ga)N$ alloy semiconductors.,” *Nature materials*, vol. 5, pp. 810–6, oct 2006.
- [22] J. H. Ryou, P. D. Yoder, J. Liu, Z. Lochner, H. S. Kim, S. Choi, H. J. Kim, and R. D. Dupuis, “Control of quantum-confined stark effect in InGaN-based quantum wells,” *IEEE Journal on Selected Topics in Quantum Electronics*, vol. 15, no. 4, pp. 1080–1091, 2009.
- [23] H. Strite, S., Morkoç, “GaN, AlN, and InN: A review,” *Journal of Vacuum Science & Technology B*, vol. 10, no. 4, pp. 1237–1266, 1992.
- [24] M. A. Reschchikov and H. Morkoç, “Luminescence properties of defects in GaN,” *Journal of Applied Physics*, vol. 97, no. 6, 2005.
- [25] X. Ning and F. Chien, “Growth defects in GaN films on sapphire: The probable origin of threading dislocations,” *Journal of materials ...*, no. 0001, 1996.

- [26] M. a. Moram, C. S. Ghedia, D. V. S. Rao, J. S. Barnard, Y. Zhang, M. J. Kappers, and C. J. Humphreys, “On the origin of threading dislocations in GaN films,” *Journal of Applied Physics*, vol. 106, no. 7, p. 073513, 2009.
- [27] R. A. Oliver, M. J. Kappers, C. McAleese, R. Datta, J. Sumner, and C. J. Humphreys, “The origin and reduction of dislocations in Gallium Nitride,” *Journal of Materials Science: Materials in Electronics*, vol. 19, pp. 208–214, mar 2008.
- [28] L. Z.-Y. Liu, *Advanced Transmission Electron Microscopy of GaN-based Materials and Devices*. PhD thesis, University of Cambridge, 2011.
- [29] J. Lahnemann, U. Jahn, O. Brandt, T. Flissikowski, P. Dogan, and H. T. Grahn, “Luminescence associated with stacking faults in GaN,” *Journal of Physics D: Applied Physics*, vol. 47, no. 42, p. 423001, 2014.
- [30] W. Rieger, R. Dimitrov, D. Brunner, E. Rohrer, O. Ambacher, and M. Stutzmann, “Defect-related optical transitions in GaN,” *Physical Review B*, vol. 54, no. 24, p. 17596, 1996.
- [31] Y. Rebane, Y. Shreter, and M. Albrecht, “Stacking Faults as Quantum Wells for Excitons in Wurtzite GaN,” *Physica Status Solidi (a)*, vol. 164, no. 141, 1997.
- [32] J. Lahnemann, O. Brandt, U. Jahn, C. Pfüller, C. Roder, P. Dogan, F. Grosse, A. Belabbes, F. Bechstedt, A. Trampert, and L. Geelhaar, “Direct experimental determination of the spontaneous polarization of GaN,” *Physical Review B*, vol. 86, pp. 1–5, 2012.
- [33] G. Nogues, T. Auzelle, M. Den Hertog, B. Gayral, and B. Daudin, “Cathodoluminescence of stacking fault bound excitons for local probing of the exciton diffusion length in single GaN nanowires,” *Applied Physics Letters*, vol. 104, p. 102102, mar 2014.
- [34] A. Hangleiter, F. Hitzel, C. Netzel, D. Fuhrmann, U. Rossow, G. Ade, and P. Hinze, “Suppression of nonradiative recombination by V-shaped pits in GaInN/GaN quantum wells produces a large increase in the light emission efficiency,” *Physical Review Letters*, vol. 95, no. 12, pp. 1–4, 2005.
- [35] S. H. Han, D. Y. Lee, H. W. Shim, J. Wook Lee, D. J. Kim, S. Yoon, Y. Sun Kim, and S. T. Kim, “Improvement of efficiency and electrical properties using intentionally formed V-shaped pits in InGaN/GaN multiple quantum well light-emitting diodes,” *Applied Physics Letters*, vol. 102, no. 25, 2013.
- [36] H.-L. Tsai, T.-Y. Wang, J.-R. Yang, C.-C. Chuo, J.-T. Hsu, Z.-C. Feng, and M. Shiojiri, “Observation of V Defects in Multiple InGaN/GaN Quantum Well Layers,” *Materials Transactions*, vol. 48, no. 5, pp. 894–898, 2007.
- [37] S. Christopoulos, G. B. H. von Högersthal, a. J. D. Grundy, P. G. Lagoudakis, a. V. Kavokin, J. J. Baumberg, G. Christmann, R. Butté, E. Feltin, J.-F. Carlin, and N. Grandjean, “Room-Temperature Polariton Lasing in Semiconductor Microcavities,” *Physical Review Letters*, vol. 98, no. 12, p. 126405, 2007.
- [38] K. J. Vahala, “Optical microcavities.,” *Nature*, vol. 424, no. 6950, pp. 839–846, 2003.

- [39] A. F. Jarjour, R. A. Taylor, Robert A.. and Taylor, M. J. Kappers, C. J. Humphreys, and A. Tahraoui, "Cavity-enhanced blue single-photon emission from a single InGaN/GaN quantum dot," *Applied Physics Letters*, vol. 91, no. 5, p. 052101, 2007.
- [40] I. Aharonovich, A. Woolf, K. J. Russell, T. Zhu, N. Niu, M. J. Kappers, R. a. Oliver, and E. L. Hu, "Low threshold, room-temperature microdisk lasers in the blue spectral range," *Applied Physics Letters*, vol. 103, no. 2, p. 021112, 2013.
- [41] G. Malpuech, A. Di Carlo, A. Kavokin, J. J. Baumberg, M. Zamfirescu, and P. Lugli, "Room-temperature polariton lasers based on GaN microcavities," *Applied Physics Letters*, vol. 81, no. 3, pp. 412–414, 2002.
- [42] a. Imamoglu, D. Awschalom, G. Burkard, D. P. DiVincenzo, D. Loss, M. Sherwin, and a. Small, "Quantum information processing using quantum dot spins and cavity QED," *Physical Review Letters*, vol. 83, no. 20, pp. 4204–4207, 1999.
- [43] K. Hennessy, a. Badolato, M. Winger, D. Gerace, M. Atatüre, S. Gulde, S. Fält, E. L. Hu, and a. Imamoğlu, "Quantum nature of a strongly coupled single quantum dot–cavity system," *Nature*, vol. 445, no. 7130, pp. 896–899, 2007.
- [44] A. C. Tamboli, E. D. Haberer, R. Sharma, K. H. Lee, S. Nakamura, and E. L. Hu, "Room-temperature continuous-wave lasing in GaN/InGaN microdisks," *Nature Photonics*, vol. 1, pp. 61–64, jan 2007.
- [45] S. Chang, N. B. Rex, R. K. Chang, G. Chong, and L. J. Guido, "Stimulated emission and lasing in whispering-gallery modes of GaN microdisk cavities," *Applied Physics Letters*, vol. 75, no. 2, p. 166, 1999.
- [46] E. D. Haberer, R. Sharma, C. Meier, A. R. Stonas, S. Nakamura, S. P. DenBaars, and E. L. Hu, "Free-standing, optically pumped, GaN/InGaN microdisk lasers fabricated by photoelectrochemical etching," *Applied Physics Letters*, vol. 85, no. 22, p. 5179, 2004.
- [47] D. Simeonov, A. Feltin, E. and Castiglia, A. Castiglia, J. F. Carlin, R. Butte, and N. Grandjean, "High quality nitride based microdisks obtained via selective wet etching of AlInN sacrificial layers," *Applied Physics Letters*, vol. 92, no. 17, pp. 2008–2010, 2008.
- [48] E. Yablonovitch, "Inhibited Spontaneous Emission in Solid-State Physics and Electronics Eli," *Physical Review Letters*, vol. 58, no. 20, pp. 2059–2062, 1987.
- [49] S. John, "Strong localization of photons in certain disordered dielectric superlattices," *Physical Review Letters*, vol. 58, no. 23, pp. 2486–2489, 1987.
- [50] K. Ishizaki, M. Koumura, K. Suzuki, K. Gondaira, and S. Noda, "Realization of three-dimensional guiding of photons in photonic crystals," *Nature Photonics*, vol. 7, no. 2, pp. 133–137, 2013.
- [51] A. Tandaechanurat, S. Ishida, D. Guimard, M. Nomura, S. Iwamoto, and Y. Arakawa, "Lasing oscillation in a three-dimensional photonic crystal nanocavity with a complete bandgap," *Nature Photonics*, vol. 5, no. 2, pp. 91–94, 2011.

- [52] Y. Gong and J. Vukovic, "Photonic crystal cavities in silicon dioxide," *Applied Physics Letters*, vol. 96, no. 3, pp. 2009–2011, 2010.
- [53] P. B. Deotare, M. W. McCutcheon, I. W. Frank, M. Khan, and M. Lončar, "High quality factor photonic crystal nanobeam cavities," *Applied Physics Letters*, vol. 94, no. 12, pp. 8–11, 2009.
- [54] M. Notomi, E. Kuramochi, and H. Taniyama, "Ultrahigh-Q nanocavity with 1D periodicity," *Conference Proceedings - Lasers and Electro-Optics Society Annual Meeting-LEOS*, vol. 16, no. 15, pp. 689–690, 2008.
- [55] P. Lalanne and J. P. Hugonin, "Bloch-Wave Engineering for High-Q, Small-V Microcavities," *IEEE Journal of Quantum Electronics*, vol. 39, no. 11, pp. 1430–1438, 2003.
- [56] N. V. Triviño, R. Butté, J.-F. Carlin, and N. Grandjean, "Continuous Wave Blue Lasing in III-Nitride Nanobeam Cavity on Silicon," *Nano Letters*, vol. 15, no. 2, pp. 1259–1263, 2015.
- [57] M. Arita, S. Ishida, S. Kako, S. Iwamoto, and Y. Arakawa, "AlN air-bridge photonic crystal nanocavities demonstrating high quality factor," *Applied Physics Letters*, vol. 91, no. 5, pp. 89–92, 2007.
- [58] W. H. P. Pernice, C. Xiong, C. Schuck, and H. X. Tang, "High-Q aluminum nitride photonic crystal nanobeam cavities," *Applied Physics Letters*, vol. 100, no. 9, 2012.
- [59] N. Niu, A. Woolf, D. Wang, T. Zhu, Q. Quan, R. a. Oliver, and E. L. Hu, "Ultra-low threshold gallium nitride photonic crystal nanobeam laser," *Applied Physics Letters*, vol. 106, no. 23, p. 231104, 2015.
- [60] S. Arafat, X. Liu, and Z. Mi, "Review of recent progress of III-nitride nanowire lasers," *Journal of Nanophotonics*, vol. 7, no. 1, pp. 074599–074599, 2013.
- [61] J. C. Johnson, H.-J. Choi, K. P. Knutsen, R. D. Schaller, P. Yang, and R. J. Saykally, "Single gallium nitride nanowire lasers.,," *Nature materials*, vol. 1, no. 2, pp. 106–110, 2002.
- [62] F. Qian, Y. Li, S. Gradecak, H.-G. Park, Y. Dong, Y. Ding, Z. L. Wang, and C. M. Lieber, "Multi-quantum-well nanowire heterostructures for wavelength-controlled lasers.,," *Nature materials*, vol. 7, no. 9, pp. 701–706, 2008.
- [63] A. Das, J. Heo, M. Jankowski, W. Guo, L. Zhang, H. Deng, and P. Bhattacharya, "Room temperature ultralow threshold GaN nanowire polariton laser," *Physical Review Letters*, vol. 107, no. 6, pp. 1–5, 2011.
- [64] C.-y. Wu, C.-t. Kuo, C.-y. Wang, and C.-l. He, "Plasmonic Green Nanolaser Based on a Metal-Oxide-Semiconductor Structure," *Nano letters*, pp. 4256–4260, 2011.
- [65] S. Deshpande, J. Heo, A. Das, and P. Bhattacharya, "Electrically driven polarized single-photon emission from an InGaN quantum dot in a GaN nanowire.,," *Nature communications*, vol. 4, p. 1675, jan 2013.

- [66] M. J. Holmes, K. Choi, S. Kako, M. Arita, and Y. Arakawa, "Room-Temperature Triggered Single Photon Emission from a III-Nitride Site-Controlled Nanowire Quantum Dot," *Nano letters*, jan 2014.
- [67] Y. Zhang, *Characterisation of GaN using Transmission Electron Microscopy*. PhD thesis, University of Cambridge, 2008.
- [68] C. B. C. David B. Williams, *Transmission Electron Microscopy*. Springer US, 2009.
- [69] M. a. Moram, Y. Zhang, M. J. Kappers, Z. H. Barber, and C. J. Humphreys, "Dislocation reduction in gallium nitride films using scandium nitride interlayers," *Applied Physics Letters*, vol. 91, no. 15, p. 152101, 2007.
- [70] A. Howie, "Image contrast and localized signal selection techniques," *Journal of Microscopy*, 1979.
- [71] A. M. . M. R. Facility, "Characteristic x-rays." <http://www.ammrf.org.au/myscope/analysis/eds/xraygeneration/characteristic/>.
- [72] G. Divitni, *Electron microscopy studies of photo-active TiO₂ nanostructures*. PhD thesis, University of Cambridge, 2012.
- [73] D. J. De Rosier and A. Klug, "Reconstruction of Three Dimensional Structures from Electron Micrographs," *Nature*, vol. 217, pp. 130–134, 1968.
- [74] P. a. Midgley and R. E. Dunin-Borkowski, "Electron tomography and holography in materials science.," *Nature materials*, vol. 8, no. 4, pp. 271–280, 2009.
- [75] G. Möbus and B. J. Inkson, "Nanoscale tomography in materials science," *Materials Today*, vol. 10, no. 12, pp. 18–25, 2007.
- [76] N. Kawase, M. Kato, H. Nishioka, and H. Jinnai, "Transmission electron microtomography without the "missing wedge" for quantitative structural analysis," *Ultramicroscopy*, vol. 107, no. 1, pp. 8–15, 2007.
- [77] J. Frank, *Electron Tomography*. Springer New York, 2006.
- [78] T. Zhu, *Nanoscale Electrical Characterisation of Gallium Nitride*. PhD thesis, University of Cambridge, 2010.
- [79] R. a. Oliver, "Advances in AFM for the electrical characterization of semiconductors," *Reports on Progress in Physics*, vol. 71, p. 076501, jul 2008.
- [80] B. Yacobi and D. Holt, *Cathodoluminescence Microscopy of Inorganic Solids*. Springer US, 1990.
- [81] T. Puchtler, *DEVELOPMENT OF STRUCTURES AND MATERIALS FOR INGAN/GAN CAVITY-QUANTUMELECTRODYNAMICS*. PhD thesis, University of Cambridge, 2014.
- [82] P. R. Edwards and R. W. Martin, "Cathodoluminescence nano-characterization of semiconductors," *Semiconductor Science and Technology*, vol. 26, p. 064005, jun 2011.

- [83] R. W. Martin, P. R. Edwards, K. P. O'Donnell, M. D. Dawson, C.-W. Jeon, C. Liu, G. R. Rice, and I. M. Watson, "Cathodoluminescence spectral mapping of III-nitride structures," *Physica Status Solidi (a)*, vol. 201, pp. 665–672, mar 2004.
- [84] P. Sercel, H. Zarem, J. Lebans, and L. Eng, "A novel technique for the direct determination of carrier diffusion lengths in GaAs/AlGaAs heterostructures using cathodoluminescence," *International Electron Devices Meeting*, pp. 285–288, 1989.
- [85] C. L. Paul R. Edwards, Lethy Krishnan Jagadamma, Jochen Bruckbauer and R. W. M. Philip Shields, Duncan Allsopp, Tao Wang, "High-resolution cathodoluminescence hyperspectral imaging of nitride nanostructures," *Microscopy and Microanalysis*, pp. 1212–1219, 2012.
- [86] E. Yakimov, "Electron-beam-induced-current study of defects in GaN; experiments and simulation," *Journal of Physics: Condensed Matter*, vol. 13069, 2002.
- [87] L. Holzer, F. Indutnyi, P. Gasser, B. Münch, and M. Wegmann, "Three-dimensional analysis of porous BaTiO₃ ceramics using FIB nanotomography," *Journal of Microscopy*, vol. 216, no. 1, pp. 84–95, 2004.
- [88] M. Albrecht, J. L. Weyher, B. Lucznik, I. Grzegory, and S. Porowski, "Nonradiative recombination at threading dislocations in n-type GaN: Studied by cathodoluminescence and defect selective etching," *Applied Physics Letters*, vol. 92, no. 23, pp. 0–3, 2008.
- [89] N. K. V. D. Laak, R. A. Oliver, M. J. Kappers, C. J. Humphreys, N. K. V. D. Laak, R. A. Oliver, M. J. Kappers, and C. J. Humphreys, "Role of gross well-width fluctuations in bright , green-emitting single InGaN/GaN quantum well structures Role of gross well-width fluctuations in bright , green-emitting single InGaN / GaN quantum well structures," vol. 121911, no. 2007, pp. 1–4, 2013.
- [90] R. a. Oliver, F. C.-P. Massabuau, M. J. Kappers, W. a. Phillips, E. J. Thrush, C. C. Tartan, W. E. Blenkhorn, T. J. Badcock, P. Dawson, M. a. Hopkins, D. W. E. Allsopp, and C. J. Humphreys, "The impact of gross well width fluctuations on the efficiency of GaN-based light emitting diodes," *Applied Physics Letters*, vol. 103, no. 14, p. 141114, 2013.
- [91] J. L. Lyons, A. Janotti, and C. G. Van De Walle, "Carbon impurities and the yellow luminescence in GaN," *Applied Physics Letters*, vol. 97, no. 15, pp. 10–13, 2010.
- [92] R. Oliver, M. Kappers, J. Sumner, R. Datta, and C. Humphreys, "Highlighting threading dislocations in MOVPE-grown GaN using an in situ treatment with SiH₄ and NH₃," *Journal of Crystal Growth*, vol. 289, pp. 506–514, apr 2006.
- [93] K. Watanabe, J. R. Yang, S. Y. Huang, K. Inoke, J. T. Hsu, R. C. Tu, T. Yamazaki, N. Nakanishi, and M. Shiojiri, "Formation and structure of inverted hexagonal pyramid defects in multiple quantum wells InGaN/GaN," *Applied Physics Letters*, vol. 82, no. 5, pp. 718–720, 2003.
- [94] M. Shiojiri, C. C. Chuo, J. T. Hsu, J. R. Yang, and H. Saijo, "Structure and formation mechanism of V defects in multiple InGaN/GaN quantum well layers," *Journal of Applied Physics*, vol. 99, no. 7, 2006.

- [95] J. Piprek, *Nitride Semiconductor Devices: Principles and Simulation*. Wiley-VCH, january 20 ed., 2007.

Appendix A

How to install L^AT_EX

Windows OS

TeXLive package - full version

1. Download the TeXLive ISO (2.2GB) from
<https://www.tug.org/texlive/>
2. Download WinCDEmu (if you don't have a virtual drive) from
<http://wincdemu.sysprogs.org/download/>
3. To install Windows CD Emulator follow the instructions at
<http://wincdemu.sysprogs.org/tutorials/install/>
4. Right click the iso and mount it using the WinCDEmu as shown in
<http://wincdemu.sysprogs.org/tutorials/mount/>
5. Open your virtual drive and run setup.pl

or

Basic MikTeX - T_EX distribution

1. Download Basic-MiK_TE_X(32bit or 64bit) from
<http://miktex.org/download>
2. Run the installer
3. To add a new package go to Start » All Programs » MikTex » Maintenance (Admin) and choose Package Manager

4. Select or search for packages to install

TexStudio - T_EX editor

1. Download TexStudio from
<http://texstudio.sourceforge.net/#downloads>
2. Run the installer

Mac OS X

MacTeX - T_EX distribution

1. Download the file from
<https://www.tug.org/mactex/>
2. Extract and double click to run the installer. It does the entire configuration, sit back and relax.

TexStudio - T_EX editor

1. Download TexStudio from
<http://texstudio.sourceforge.net/#downloads>
2. Extract and Start

Unix/Linux

TeXLive - T_EX distribution

Getting the distribution:

1. TeXLive can be downloaded from
<http://www.tug.org/texlive/acquire-netinstall.html>.
2. TeXLive is provided by most operating system you can use (rpm, apt-get or yum) to get TeXLive distributions

Installation

1. Mount the ISO file in the mnt directory

```
mount -t iso9660 -o ro,loop,noauto /your/texlive####.iso /mnt
```

2. Install wget on your OS (use rpm, apt-get or yum install)

3. Run the installer script install-tl.

```
cd /your/download/directory  
.install-tl
```

4. Enter command ‘i’ for installation

5. Post-Installation configuration:

<http://www.tug.org/texlive/doc/texlive-en/texlive-en.html#x1-320003.4.1>

6. Set the path for the directory of TexLive binaries in your .bashrc file

For 32bit OS

For Bourne-compatible shells such as bash, and using Intel x86 GNU/Linux and a default directory setup as an example, the file to edit might be

```
edit $~/.bashrc file and add following lines  
PATH=/usr/local/texlive/2011/bin/i386-linux:$PATH;  
export PATH  
MANPATH=/usr/local/texlive/2011/texmf/doc/man:$MANPATH;  
export MANPATH  
INFOPATH=/usr/local/texlive/2011/texmf/doc/info:$INFOPATH;  
export INFOPATH
```

For 64bit OS

```
edit $~/.bashrc file and add following lines  
PATH=/usr/local/texlive/2011/bin/x86_64-linux:$PATH;  
export PATH  
MANPATH=/usr/local/texlive/2011/texmf/doc/man:$MANPATH;  
export MANPATH
```

```
INFOPATH=/usr/local/texlive/2011/texmf/doc/info:$INFOPATH;
export INFOPATH
```

Fedora/RedHat/CentOS:

```
sudo yum install texlive
sudo yum install psutils
```

SUSE:

```
sudo zypper install texlive
```

Debian/Ubuntu:

```
sudo apt-get install texlive texlive-latex-extra
sudo apt-get install psutils
```

Appendix B

Installing the CUED class file

\LaTeX .cls files can be accessed system-wide when they are placed in the <texmf>/tex/latex directory, where <texmf> is the root directory of the user's \TeX installation. On systems that have a local texmf tree (<texmflocal>), which may be named "texmf-local" or "localtexmf", it may be advisable to install packages in <texmflocal>, rather than <texmf> as the contents of the former, unlike that of the latter, are preserved after the \TeX system is reinstalled and/or upgraded.

It is recommended that the user create a subdirectory <texmf>/tex/latex/CUED for all CUED related \LaTeX class and package files. On some \TeX systems, the directory look-up tables will need to be refreshed after making additions or deletions to the system files. For \TeX Live systems this is accomplished via executing "texhash" as root. MIK \TeX users can run "initexmf -u" to accomplish the same thing.

Users not willing or able to install the files system-wide can install them in their personal directories, but will then have to provide the path (full or relative) in addition to the filename when referring to them in \TeX .

